

DEVELOPING A PLATFORM FOR CQED STUDIES OF SILICON VACANCY  
CENTERS IN DIAMOND WITHIN THE GOOD-CAVITY LIMIT

by

ABIGAIL PAULS

A DISSERTATION

Presented to the Department of Physics  
and the Division of Graduate Studies of the University of Oregon  
in partial fulfillment of the requirements  
for the degree of  
Doctor of Philosophy

December 2022

## DISSERTATION APPROVAL PAGE

Student: Abigail Pauls

Title: Developing a Platform for cQED Studies of Silicon Vacancy Centers in Diamond within the Good-Cavity Limit

This dissertation has been accepted and approved in partial fulfillment of the requirements for the Doctor of Philosophy degree in the Department of Physics by:

Brian Smith	Chairperson
Hailin Wang	Advisor
Stephanie Majewski	Core Member
Cathy Wong	Institutional Representative

and

Krista Chronister	Vice Provost for Graduate Studies
-------------------	-----------------------------------

Original approval signatures are on file with the University of Oregon Division of Graduate Studies.

Degree awarded December 2022



© 2022 Abigail Pauls

This work is licensed under a Creative Commons  
**Attribution-NonCommercial-NoDerivs (United States) License.**



## DISSERTATION ABSTRACT

Abigail Pauls

Doctor of Philosophy

Department of Physics

December 2022

Title: Developing a Platform for cQED Studies of Silicon Vacancy Centers in Diamond within the Good-Cavity Limit

Silicon vacancy centers (SiVs) in diamond are local defects in the diamond lattice that behave as atomic-like systems with electronic energy levels and optical transitions. The SiV's optical properties and long spin decoherence times ( $> 10$  ms @ 100 mK), along with its ability to be integrated into nano-engineered devices while maintaining its optical coherence, make it an attractive option as a solid state spin qubit for applications in quantum information.[1, 2, 3] Here I present my work to develop a composite platform for cavity quantum electrodynamics (cQED) studies of SiVs in diamond in the good-cavity limit,  $\kappa < g < \gamma$ , where  $\kappa$ ,  $g$ , and  $\gamma$  are the cavity decay rate, single-photon coupling rate, and excited state decay respectively. The system utilizes a strain-tunable silica microsphere optical resonator in contact with a 100 nm thin SiV diamond membrane which couples to the cavity modes via the external evanescent field. This system takes advantage of the exceptionally narrow cavity linewidths ( $< 50$  MHz) of microspheres to enable

cQED studies in the good cavity limit and eventually allow cavity mediated control of the SiV spin state through the use of three-level  $\Lambda$  systems. Cavity transmission measurements confirm that cavity mode broadening can be as small as 3 MHz when the membrane is in contact with the sphere. Photoluminescence (PL) and Photoluminescence Excitation (PLE) spectroscopy of the composite system show efficient coupling of SiV fluorescence into the cavity modes with single SiV optical transitions that are spectrally resolvable ( $\gamma/2\pi \approx 200\text{-}400$  MHz.) Strain tuning of the cavity has been demonstrated over a range of 500 GHz, and the system has been made robust to the vibration and acoustic noise created by the operation of the cryostat that keeps the system at 4 K. A theoretical estimate of the single photon coupling rate ( $g/2\pi = 150$  MHz) suggests this system can reach cooperativities of  $C \approx 10$ , which should be sufficient to observe cQED coupling effects in the SiV-cavity system.

This dissertation contains previously published and unpublished material.

## CURRICULUM VITAE

NAME OF AUTHOR: Abigail Pauls

GRADUATE AND UNDERGRADUATE SCHOOLS ATTENDED:

University of Oregon, Eugene, Oregon  
Goshen College, Goshen, Indiana

DEGREES AWARDED:

Doctor of Physics, 2022, University of Oregon  
Master of Physics, 2022, University of Oregon  
Bachelors of Arts, 2013, Goshen College

AREAS OF SPECIAL INTEREST:

Quantum Optics, cQED, Color Centers in Diamond, Cryogenics, Instrument Design

PROFESSIONAL EXPERIENCE:

Research Assistant, University of Oregon, 2015-2022  
Teaching Assistant, University of Oregon, 2014-2019

GRANTS, AWARDS AND HONORS:

Emanuel Thesis Scholarship, University of Oregon Center for Optical, Molecular, and Quantum Science, 2022

PUBLICATIONS:

Abigail Pauls, Ignas Lekavicius, and Hailin Wang. Coupling silicon vacancy centers in a thin diamond membrane to a silica optical microresonator. *Opt Express*. 2020 Sep 14; 28(19):27300-27307.

Abigail Pauls, Yiteng Zhang, Gennady P. Berman, and Sabre Kais. Quantum coherence and entanglement in the avian compass. *Phys. Rev. E*. 2013 June 11; 87(6):062704.

## ACKNOWLEDGEMENTS

Thank you to all my current and former lab mates for your collaboration and assistance through the years. I'm especially grateful to Ethan Turner, Xinzhu Li, Shuhao Wu, and Ran-Ran Xie for your friendship and camaraderie. Your company and support has been a constant source of encouragement to get through those tough days in the lab when everything seems to go wrong. I've never had more fun being miserable with anyone else more than you guys.

Thank you to Ignas Lekavicious for your tireless fabrication work to create the diamond membranes that were the basis for this project. Another thank you to Xinzhu Li as well for honing the fabrication process for diamond membranes. Your excellent low SiV-density sample was crucial for allowing me to eventually resolve single SiV optical transitions, one of the key goals of this experiment. Thank you to my advisor, Hailin Wang, for your persistent support, availability, and constantly challenging me to “think on my feet” and grow as a physicist.

A huge thank you goes out to all the folks at the TSA shop: John Boosinger, Geordi Helmick, Jeffrey German, and Julian McAdams. Fabricating new components for my experiment was one of the most enjoyable and time intensive aspects of this project. Y'all were always available and ready to help anytime I had a question or needed to learn how to use a new tool. Every time I finished a project in the shop I always left hoping I'd have an excuse to return soon to work on something new.

Thank you to those who offered your time, assistance, and willingness to just listen and commiserate when the world outside of the lab was wearing me

down. Stephanie Majewski, Tzula Propp, Kara Zappitelli, and Ethan Turner- it's impossible to imagine having persisted this long without your help.

Thank you to my parents for nurturing my curiosity and love of science from a young age, as well as to all the teachers and educators that helped me on my journey to this point. Thank you to my brother, David, for just being around, hanging on the porch, and drinking cheap beer with us. You helped me get through some of the toughest moments of grad school just by being there.

Lastly, the biggest thank you to my adventure buddy and spouse, Ana.

Dedicated to Trout and Hank.

This dissertation is the product of unionized labor as part of the Graduate Teaching Fellows Federation, AFT Local 3544.

# TABLE OF CONTENTS

Chapter	Page
I. INTRODUCTION . . . . .	1
1.1. An Introduction to an Introduction . . . . .	1
1.2. Experimental Confirmation of Murphy's Law . . . . .	10
1.3. Outline . . . . .	13
II. CAVITY QUANTUM ELECTRODYNAMICS, AN OVERVIEW . . .	16
2.1. Introduction . . . . .	16
2.2. Jaynes-Cummings Model for a Two Level Atomic System . . . .	17
2.3. cQED in the Linear Regime . . . . .	19
2.4. Theoretical Estimation of cQED Performance of the Sphere-Membrane System . . . . .	24
III. SILICA MICROSPHERE OPTICAL CAVITIES . . . . .	27
3.1. An Introduction to Optical Cavities . . . . .	27
3.2. Whispering Gallery Mode Solutions . . . . .	29
3.3. Coupling to a Microsphere via Tapered Optical Fiber Waveguide	33
3.4. WGM Strain Tuning . . . . .	37
3.5. Fabricating Double Stemmed Microsphere Cavities . . . . .	39
3.6. Fabricating Tapered Fiber Waveguides . . . . .	47



Chapter	Page
IV. SILICON VACANCY COLOR CENTERS IN DIAMOND: THEIR PROPERTIES, AND FABRICATION OF SiV IMPLANTED MEMBRANES . . .	53
4.1. An Introduction to Color Centers . . . . .	53
4.2. SiV Electronic Structure and Optical Properties . . . . .	54
4.3. Fabricating SiV Implanted Nano-Membranes in Diamond . . . .	58
V. SIVS AND CQED: APPLICATIONS IN THE GOOD CAVITY LIMIT USING THREE-LEVEL $\Lambda$ SYSTEMS . . . . .	62
5.1. Introduction . . . . .	62
5.2. A $\Lambda$ System for the SiV Spin State . . . . .	62
VI. "THINKING ON YOUR FEET:" EXPERIMENTAL DESIGN, METHODS, AND CHALLENGES . . . . .	68
6.1. Constraints and Objectives of the System Design . . . . .	68
6.2. Cryostat System Design . . . . .	69
6.3. Optics Setup and Data Acquisition . . . . .	75
6.4. Configuring the Cryostat System . . . . .	80
6.5. Cavity Transmission Spectrum Measurement . . . . .	82
6.6. Optical Alignment and Spectroscopy Experiments . . . . .	83
6.7. Challenges of Working in the Cryostat Environment . . . . .	86
6.8. Vacuum Performance . . . . .	86
6.9. Noise and Vibrational Performance . . . . .	90
6.10. Redesigning the Cryostat System to Limit the Impact of Vibration	94

Chapter	Page
VII. CHARACTERIZATION OF THE TUNABLE CAVITY QED SYSTEM	97
7.1. Introduction . . . . .	97
7.2. WGM Q-Spoiling . . . . .	97
7.3. Tension mediated cavity tuning . . . . .	98
7.4. Vibration Performance . . . . .	100
VIII. COUPLING BETWEEN SILICON VACANCY CENTERS AND WHISPERING GALLERY MODES . . . . .	113
8.1. Introduction . . . . .	113
8.2. PL and PLE Spectroscopy . . . . .	113
8.3. Revisiting the Estimate for $C$ in the Composite cQED System . .	121
IX. GUIDANCE FOR FUTURE WORK AND CONCLUSIONS . . . . .	123
9.1. Introduction . . . . .	123
9.2. Further Modifications for Vibration and Acoustic Susceptibility .	124
9.3. Addressing Sample Contamination . . . . .	128
9.4. Managing Nitrogen Deposition . . . . .	130
9.5. Potential improvements of $C$ and $g$ . . . . .	132
9.6. Modeling Membrane-Coupled Equatorial WGMs . . . . .	133
9.7. PLE Count Rate and Signal-to-Noise Optimization . . . . .	134
9.8. Experimentation: Next steps . . . . .	138
9.9. Conclusion . . . . .	140

Chapter	Page
REFERENCES CITED . . . . .	142

## LIST OF FIGURES

Figure		Page
1.1.	The evolution of optics applied to sending information over large distances: the Lighthouse of Alexandria to modern day fiber optic networks. . . . .	2
1.2.	The photonic crystal SiV cQED system developed by Sipahigil et. al and our complementary cQED system utilizing a silica microsphere and ultra thin SiV diamond membrane. . . . .	7
1.3.	Example of how the SiV spin state can be optically controlled using a classical laser field $\Omega_L$ and an optical cavity $g$ to drive a three-level $\Lambda$ system when a magnetic field is applied to lift the SiV spin degeneracy. [43] . . . . .	9
1.4.	“Serenity Now!” - a poster haphazardly scotch-taped to the cryostat helium compressor unit. . . . .	10
2.1.	Cartoon of a simple atom and Fabry-Pérot cQED system. . . . .	16
2.2.	Energy-level structure for the independent and coupled system Hamiltonians. The energy structure given for the total interaction Hamiltonian is shown for the case when there is zero detuning between the cavity and atomic transition frequencies . . . . .	19
2.3.	Plots of the cavity field and atomic polarization for steady state driving of the cavity field in the bad cavity, good cavity, and strong coupling limits. The cavity mode is zero-detuned from the atomic transition . . .	23
2.4.	Plots of the steady state cavity field and atomic polarization for cQED parameters matching the estimates for the SiV-microsphere system. Both are plotted for various values of the cavity-atom detuning. . . . .	25
3.1.	Micrographs visualizing the cavity mode distribution of several modes with different $l$ and $m$ values. [40] The silica sphere is doped with erbium atoms which fluoresces due to the cavity field. . . . .	32
3.2.	Illustration of the optical coupling between sphere and taper via overlapping evanescent fields. . . . .	35

Figure	Page
3.3. Plots of the cavity transmission spectrum for a single WGM in under coupled, critically coupled, and over coupled regimes. . . . .	36
3.4. Cavity mode transmission for the case of a tapered fiber aligned with the equator (red) and the case a of taper positioned away from the equator (blue). The presence of a specific WGM in the red spectrum while being absent in the blue spectrum indicates it is an equatorial mode. . . . .	36
3.5. Illustration depicting the process of WGM resonance tuning via tension provided by an attocube nanopositioner. Displacement of the nanopositioner causes a change in the stem tension which causes a small deformation of the cavity geometry, and in turn results in a frequency shift of the cavity resonance. . . . .	39
3.6. Like beads of water, molten silica will naturally relax into a spherical geometry from the presence of surface tension. . . . .	39
3.7. System for making double stemmed microspheres. Top and bottom fiber chucks are visible, with the CO <sub>2</sub> laser focusing lens visible behind the top fiber chuck, and the imaging objective visible to the left. . . . .	40
3.8. A) The hydrogen torch heating optical fiber while stretching it. B) An illustration of the stretching process. . . . .	42
3.9. Trimming the excess fiber from the hanging stem of a double stemmed sphere. A) An arrow points to the specific point where the fiber needs to rest during cutting. B) An illustration showing roughly the necessary angles for holding the fiber strippers and fiber chuck to successfully cut the excess fiber without breaking the sphere. Note that in addition to the bend as the fiber transitions from the chuck alignment to the alignment of the hanging stem, there is a slight second segment of curvature on the fiber chuck end of the sphere which indicates there is slack on the the fiber. . . . .	45
3.10. A double stemmed sphere in the process of being mounted and epoxied on to the sphere assembly. The both stems rest in their respective v-grooves and the sphere (not visible) rests at the center of the gap between the two grooves. . . . .	48
3.11. Color bands due to thin-film interference indicate the taper waist location during gluing of the fiber to the carrier fork. The center (wide yellow band) is surrounded by many other colored bands. The apparent	

Figure	Page
thickness of the taper is an artifact from camera motion during the exposure. . . . .	51
3.12. A series of photographs taken at successive steps of DSS fabrication. 1) A tapered fiber is cut with the laser and the tip is melted into a small droplet. The sphere can be seen glowing from the heat of the CO <sub>2</sub> laser. 2) The process is repeated for a second larger sphere and the first sphere is mounted on the translations stage below. 3) Both spheres are brought into contact and fused with low laser power. 4) Continued annealing of the fused spheres results in a single elongated almond shape. Also note that at this stage, the stems are not parallel to one another. 5) The hanging stem is trimmed and the sphere annealed repeatedly from multiple angles until it produces a nearly perfect sphere with co-aligned stems. . . . .	52
4.1. A) A 2D representation of the SiV geometry. B) SiV <sup>-</sup> energy-level diagram for zero B field, and the case when an applied magnetic field lifts the spin state degeneracy. Green arrows indicate dipole-allowed transitions and red arrows indicate dipole-forbidden transitions. Dipole-forbidden transition may be allowed due to state mixing from the presence of an off-axis magnetic field. [43] . . . . .	54
4.2. Confocal PLE of SiVs in the diamond membrane with no sphere present. A) PLE spectra of the SiV C and D transitions constructed from five individual narrow frequency laser scans. B) PLE of the D transition only. C) Scatter plot showing measured SiV transition linewidths as a function of membrane thickness demonstrating good optical coherence even when integrated in a nanophotonic device. D and E) Scans of individual SiV transitions corresponding to the two data points in C identified with blue arrows. . . . .	58
4.3. Scatter plot showing measured SV transition linewidths as a function of membrane thickness. In contrast to the SiV membrane samples, the NV linewidths are dramatically broadened. Membrane thicknesses of less than 600 nm result in linewidths greater than 1 GHz. . . . .	59
4.4. A) Optical microscope image of the low SiV density membrane mounted on the copper sample mount. B) An enlarged view of the blue box. Color bands indicating a tapered membrane thickness are visible. . . . .	61
5.1. Three level $\Lambda$ system of the SiV spin state using the cavity mode and classical driving field.[66, 67] . . . . .	63

Figure	Page
5.2. Calculated transmission spectrum (solid curve) of a cavity QED system containing a $\Lambda$ -type 3-level system driven by a classical control field, with $\Delta = 0$ , $\gamma/2\pi = 200$ MHz, $\kappa/2\pi = g/2\pi = \Omega_L = 100$ MHz, and $\gamma_s/2\pi = 4.5$ MHz. The dashed line shows the transmission spectrum of the empty cavity.[68] . . . . .	65
5.3. Cavity mediated spin state transfer between two SiVs within the same optical cavity. . . . .	66
6.1. Top view of the last evolution of the cryostat system design, installed in the cryostat sample chamber with the radiation shield in place. . . . .	68
6.2. A cross section sketch of the cryostat setup. . . . .	70
6.3. Cryostat sample chamber with central pedestal, attocube nanopositioners with flex link, and sample mount installed on the 4K cold platform. The 4K PCB boards (gold) are visible surrounding the pedestal. . . . .	71
6.4. Outer pedestal mounted on the 4K PCB boards. . . . .	72
6.5. Taper assembly (missing the Invar fork) mounted on the outside pedestal . . . . .	74
6.6. Cryostat setup with the top sphere mounting assembly installed and fiber fork mounted to the fiber positioning attocubes. Note that the fork pictured is from the first design iteration and the improved design used for experimental runs with the low SiV density sample is pictured in the first figure of this chapter. . . . .	76
6.7. Closeup of the cryostat system (without tapered fiber). The DSS is visible suspended across the two v-grooves. The diamond membrane is seen mounted to the copper pedestal with silver paste. . . . .	77
6.8. Schematic of optical and data aquisition setup. . . . .	78
6.9. Illustration of the method used to measure the cavity transmission spectrum. . . . .	80
6.10. 532 nm scan raster image of the sphere-membrane system. The silhouette of the sphere can be seen, and the point of high intensity at the left edge of the sphere is due to free space coupling of the 532 nm light into the sphere. The blue dotted circle denotes the approximate contact point. . . . .	84

Figure	Page
6.11. An extreme case of nitrogen ice deposition during an initial test run without the top radiation shield lid installed. Sub-micron sized spots of nitrogen ice deposition cause scattering of nearly 100 percent of the light propagating in the fiber into free space, causing it to glow red from the scattered laser light. . . . .	87
6.12. Micrograph of the sphere after the oil leak into the sample chamber. Significant oil accumulation is visible where the sphere was in contact with the membrane. . . . .	89
6.13. Illustration depicting cases of vibrational modes of the sphere-taper system inducing coupling noise. In the top example, the sphere is stationary while the taper experiences guitar string vibrational modes. The bottom case depicts vibration of the sphere either due to guitar string modes of the DSS stems, or vibration through contact with a vibrating sample mount. . . . .	91
6.14. A simplified illustration of the process responsible for vibration and acoustically induced cavity frequency noise. Sound and/or vibration from the cryostat excites resonant vibration of one of the anchor points of the double stemmed sphere. The resulting vibration at the anchor point results in high frequency variation of the stem tension leading to rapid modulation of the cavity mode resonance frequency. . . . .	93
6.15. The original cryostat system design. Note the relatively tall and thin sample mount and taper anchor point which posed major issues for vibration and acoustic sensitivity. . . . .	95
7.1. Cavity transmission spectra of an equatorial WGM with the sphere alone, and the case when the diamond membrane is in contact with the sphere. . . . .	98
7.2. Data showing WGM frequency shift data from strain tuning experiments. A) Long range tuning data utilizing the attocube step function. B) Tuning data using the continuous DC offset mode over 60 volts of its 150 volt range. C) DC offset tuning data over a narrower 5V range to demonstrate the tuning resolution. Note that this data was taken using the first cryostat system design which was more sensitive to ambient system noise. Also note that the need to readjust the taper coupling over the course of the experiment introduces some variation due to frequency shifts from the taper coupling. . . . .	100
7.3. Illustration of the data acquisition scheme used to measure the effective cavity broadening at different points in the cryostat cold head cycle. . .	101



Figure	Page
7.4. WGM frequency noise data consisting of 9 successive frequency scans gated by a set delay time relative to the 1 Hz trigger output from the cryostat. A single scan of the mode with the cryostat off is used to establish the natural linewidth of the mode. The linewidth of the averaged trace is given for each delay. The specific WGM is a near equatorial ( $l - m + 1 = 3$ ) mode which has been tightened to 200 attocube steps past being slack using a 30V step size. . . . .	109
7.5. Vibration data for an $l - m + 1 = 3$ WGM with the DSS tightened to 50 attocube steps past slack. 9 successive WGM traces are taken for each trigger delay, and the best fit linewidth is given for the cumulative average curve for each delay set. . . . .	110
7.6. Vibration data for an $l - m + 1 = 3$ WGM with the DSS tightened to 150 attocube steps past slack. 9 successive WGM traces are taken for each trigger delay, and the best fit linewidth is given for the cumulative average curve for each delay set. Contamination of the sphere led to a larger intrinsic WGM linewidth. . . . .	111
7.7. Reduction of averaged WGM linewidth via a naive drift correction model. A) Successive cavity resonance scans taken at a 400ms delay relative to the cold head trigger signal. Colored in chromatic order from red (first) to violet (last). B) averaged trace (blue) and lorentzian best fit model (red) which gives a linewidth of 117 MHz. C) Corrected WGM traces shifted in frequency assuming constant rate of drift. D) Averaged trace with the correction applied (blue) and lorentzian best fit (red) which gives a linewidth of 56 MHz. . . . .	112
8.1. PL spectra of the sphere-membrane system showing two peaks separated by the SiV excited state splitting. The blue line is from data collected with no 532 nm excitation, using the same integration duration as a control to distinguish SiV fluorescence from background. . . . .	114
8.2. PLE spectra of the sphere-membrane system using the original high SiV density membrane sample. All four SiV transitions are visible. The data has been background subtracted using an identical PLE scan that was taken without off resonant 532 nm excitation. . . . .	116
8.3. Blue line: PLE spectra of the sphere-membrane system using the low SiV density membrane sample. Orange line: control scan taken with zero 523 nm initialization pulse. Much sharper features are visible suggesting single SiV transitions. . . . .	120

Figure	Page
8.4. A) PLE scan of the SiV B transitions. B) A narrower plot of the data with arrows identifying potential single SiV transitions. . . . .	121
8.5. A) Wide frequency PLE scan of the SiV C transitions. B) A narrower scan of the two peaks shown within the outlined box in A. C) A repeated scan of both peaks but with reduced 737 nm power, revealing narrower fluorescence peaks of presumably single SiV transitions. . . . .	122
9.1. A micrograph of the membrane contact point of a contaminated sphere taken with a scanning electron microscope. Many spots of contamination are visible and the different shades of the contaminants suggest multiple substances are present. The blurry rectangular ghost images present in the micrograph are an artifact from hydrocarbons that deposit onto the surface while in the SEM and are subsequently burned off by the electron beam. They do not indicate actual surface features or contamination present while the sphere is in the cryostat. . . . .	129
9.2. A micrograph of the same sphere taken at a 45° angle away from the view axis of the previous figure. The surface is clean, indicating the contamination buildup originated from an contact with the membrane and not the cryostat environment itself. . . . .	130
9.3. A micrograph of a section of a single diamond membrane taken with an optical microscope. The image has been slightly enhanced to show the numerous spots of surface contamination. . . . .	131

## CHAPTER I

### INTRODUCTION

#### 1.1. An Introduction to an Introduction

Through the centuries as our understanding of light and matter has progressed, we have always found new ways to apply that understanding to facilitate the exchange of information over large distances through the use of light. In the third century B.C.E., optics was in its infancy and matter was only understood in terms of the elements described by Empedocles: water, earth, fire, and air. The Lighthouse of Alexandria, an engineering marvel for its time, served as a beacon to warn ships at sea from running aground. Its light was created by a simple wood-fueled bonfire at its peak, with only a flat metal mirror to reflect the otherwise omni-directional light towards the sea. Many centuries later, early advancements in chemistry enabled brighter, more efficient flames through oil burning lanterns whose combustion had been optimized to burn hotter and brighter, and advances in optics enabled the manipulation of light through the use of lenses. This enabled lighthouses that could produce light from a more efficient source that was enhanced further through collimation. Not only did this increase the visibility of the beacon, but it also enabled the encoding of information into the light through the amplitude modulation resulting from rotating lenses.

Further advances in chemistry and the study of black body radiation facilitated the invention of incandescent bulbs, which enabled the generation of light through electricity. The advent of a quantum mechanical description of atoms resulted in the invention of lasers, which generate coherent light that can be more

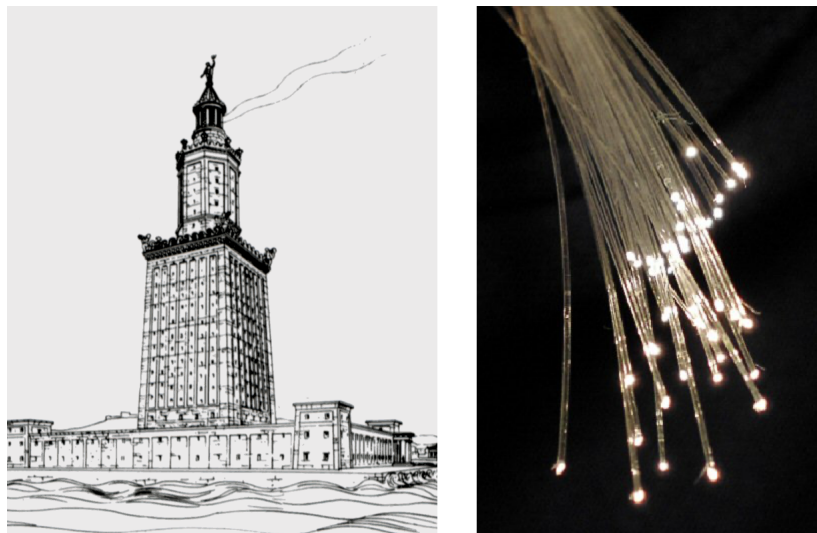


FIGURE 1.1. The evolution of optics applied to sending information over large distances: the Lighthouse of Alexandria to modern day fiber optic networks.

effectively collimated and modulated in intensity and polarization to transmit large volumes of data rapidly over distances on the scales of continents and even the solar system.

Today, lasers are beginning to be used as high speed data links between spacecraft exploring the solar system, and the backbone of our information infrastructure is built upon networks that transmit digital information across the globe as modulated laser light confined within fiber optic cables. The current frontier of optics at its intersection with information is the development of quantum networks and computers, which will utilize the quantum nature of both light and matter simultaneously to create systems for exchanging and processing information in radically new ways.

A primary motivator for the work described in this thesis is the development of platforms for quantum computing and quantum networking. There is large interest in the development of quantum computers due to their potential to offer

dramatic increases in processing speed for certain tasks and their potential ability to accurately simulate quantum systems that are intractable with any realistic classical computer. The distinction between classical computing and quantum computing comes from the basic logical unit used to construct them. Classical computers rely on transistors for storing and manipulating information, which have only “on” and “off” states - in binary terms: “1” and “0” - known as bits. If engineered properly, however, the individual bits of a computer can be made to be susceptible to the weirdness of quantum mechanics. A classical bit, whether observed or not, will always have a definite state of either 1 or 0. In a quantum system, however, the phenomenon of superposition of states allows for the bit to exist in a well-defined state that is a weighted superposition of both 1 and 0, until it is “collapsed” via measurement or decoherence from environmental noise. These quantum-affected bits are referred to as qubits. Their superposition of states, as well as the phenomenon of quantum entanglement within a computational system, should in theory enable the execution of certain algorithms that can be completed exponentially faster than what is possible with a classical computer, as well as enable more effective encryption schemes for communication.

Along with the interest in the development of quantum computers comes the need to create quantum networks that can transmit information via qubits instead of bits.[4] If we wish to connect two separate quantum computers or nodes while still utilizing quantum behavior, we need both a channel capable of carrying that quantum information and a means to exchange information between whatever quantum system constitutes each node/computer and the networking channel. There are several general types of qubits currently being explored for use in quantum computing networking, including trapped ions/cold atoms, quantum

dots, superconducting qubits, and solid state qubits. [4, 5, 6, 7, 8] Each of these different qubit types has advantages and disadvantages, which likely means the future of computing and networking will not be dominated by one single qubit type but a mix of several used in different applications according to their strengths and weaknesses. Ultimately, quantum networks of the future will almost certainly be built upon the backbone of fiber optics.[4, 9] The already widespread use of fiber optics in telecommunications, as well as their ability to effectively transmit light long distances with minimal loss or distortion, make fiber optics an ideal method for transmitting quantum information. This ultimately leads us to the question that motivates this project: how can we create a system that allows effective exchange of quantum information between an optical channel/qubit and a stationary qubit that is part of a local quantum node?

The work presented here will focus specifically on the use of a particular kind of solid state qubit known as a color center in diamond, in particular a silicon vacancy color center. Color centers in diamond are local defects in the diamond lattice that behave as an atomic-like system with its own electronic energy level structure and are the phenomena responsible for the different colors diamonds can exhibit (think The Pink Panther) The more well known nitrogen vacancy center, for example, has an optical transition at 637 nm, which results in the diamonds containing them to appear pink or red depending on the density of NVs.[10, 11, 12, 13] The work presented here focuses specifically on the silicon vacancy (SiV) color center for application in quantum networking.[9, 14, 15, 16, 17] In the case of SiVs, the electronic structure is that of a spin-1/2 system, and under the proper conditions, it can exhibit spin decoherence times greater than 10 ms. This long lived spin can be used to store quantum information over the course

of quantum operations functioning as logic gates.[1, 2, 3, 18, 19] Experiments with the neutral SiV charge state have shown longer coherence times achievable at room temperatures.[20] SiVs are also ideal for integration in nano-fabricated systems because they can retain their narrow ( 200 MHz) transition linewidths, whereas NVs experience dramatic broadening due to a greater susceptibility to the electric field noise that comes with being positioned near the diamond surface.[21, 22, 23, 24, 25, 26, 27, 28] If we wish to use the SiV spin state as a qubit, the question then becomes how we go about coupling to it optically to facilitate a quantum network. The quantum state of an SiV can be controlled by classical laser fields[22, 23, 24, 25], but for SiVs to be used in a quantum optical network, we need a quantum system that can also be effected by single light quanta. A way to achieve this is through the integration of SiVs into optical cavities.

Optical cavities function by trapping light within a confined volume for some finite amount of time. By confining light, a cavity can enhance any optical field coupled into it that matches one of its resonance frequencies. The smaller a cavity is, and the longer light can propagate within the cavity before being lost, the greater the enhancement. The application of cavities into quantum systems can then be used to enhance quantum control for applications in computing and networking.[9, 17, 29] The coupling of an atomic system with a cavity field is described by the single-photon coupling rate,  $g$ , which characterizes the strength of coupling between the cavity field and dipole moment associated with the particular atomic transition. For an atomic transition with an excited-state decoherence rate  $\gamma$ , and an optical cavity with decay rate  $\kappa$ , a useful figure of merit for describing

the coupling between the cavity and atom is its cooperativity which is given by,

$$C = \frac{4g^2}{\kappa\gamma}. \quad (1.1)$$

For the case  $C > 1$ , the behavior of the system becomes susceptible to the presence of individual atoms and/or photons. The task now becomes creating a SiV-cavity system that optimizes the relevant cQED parameters.

Some work has already explored integration of SiVs into both whispering gallery mode (WGM) and photonic crystal cavities[21, 30, 31], as well as the integration of SiVs and other color centers into mechanical cavities that use similar principles.[32, 33] One such system has already been developed by Sipahigil et. al at Harvard University. Their system utilizes monolithic 1D photonic crystal cavities constructed from the same diamond that contains the SiVs to which they couple. A long narrow beam of diamond is suspended on either end to a carrier chip. Holes are then milled into the beam at a periodic interval using focused ion-beam milling that then behave as two opposing Bragg mirrors. SiVs are then formed by implanting the center of the cavity mode volume with silicon atoms and annealing it to form the SiVs.[21, 30, 34, 35] This system has been utilized to demonstrate cavity mediated optical control of SiVs and cavity-mediated coupling between multiple SiVs contained within the same cavity. This system has also been used to demonstrate its implementation in a quantum register.[36] A key advantage to this cavity system is its small mode volume, which helps to enhance the coupling strength ( $g = 8$  GHz) and achieve cooperativities as high as  $C \approx 100$ .

In this thesis, I present a SiV cQED coupling scheme complementary to the photonic crystal scheme that utilizes a silica microsphere optical resonator as an alternative optical cavity that then couples to an ultra-thin (100 nm) diamond



membrane containing the SiVs.[28, 37, 38, 39] Silica microspheres are, as the name would suggest, near perfectly spherical cavities composed purely of silica.[40] Microspheres support a particular family of cavity modes known as whispering gallery modes (WGMs) that are confined to circulate within the boundary of the sphere due to the effects of total internal reflection. Microspheres can achieve exceptional cavity linewidths that make them well suited for cQED experiments within the good-cavity limit ( $\gamma \gg g\kappa$ ) where the cavity linewidth is much less than the single-photon coupling rate and SiV optical transition linewidth. Whereas the photonic crystal scheme is limited to cavity linewidths of 20 GHz, silica microspheres can achieve linewidths of 30 MHz.

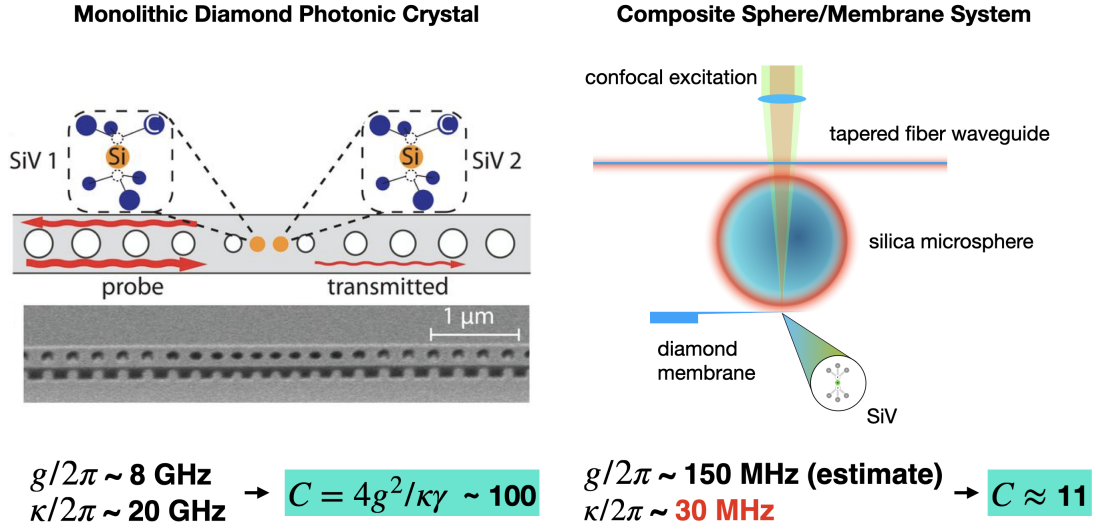


FIGURE 1.2. The photonic crystal SiV cQED system developed by Sipahigil et. al and our complementary cQED system utilizing a silica microsphere and ultra thin SiV diamond membrane.

Due to the confinement from total internal reflection, a portion of the WGM also circulates just outside the boundary of the cavity as an evanescent field decaying exponentially away from the sphere. The presence of this external field allows objects, near or in contact with the sphere, to couple to the cavity

mode.[41, 42] If a thin SiV implanted diamond membrane is brought into contact with the sphere, the overlap of the evanescent field with the membrane will allow the nearest SiVs to couple to the cavity. By ensuring that the SiV-containing membrane is fabricated as thin as possible, contact of the membrane with the sphere will result in coupling of the SiVs to the cavity while also minimizing the mode broadening (also known as Q-spoiling) caused through absorption and scattering by the membrane.

A particular drawback of the photonic crystal cavity system stems from its cavity linewidth. The photonic crystal design is inherently limited to a cavity linewidth in the tens of gigahertz.[21, 34] This poses a roadblock to utilizing the system for cavity mediated interactions and control of the SiV spin state. Each of the four SiV energy levels are actually a pair of degenerate spin  $1/2$  and spin  $-1/2$  states. An external magnetic field can be used to lift the degeneracy via Zeeman splitting, which then allows for optical control of the SiV spin state through Raman transitions using a pair of ground states (whose degeneracy has been lifted by a magnetic field) as the bottom two states of a  $\Lambda$ -type optical system. Realization of optical control using a classical driving in tandem with the optical cavity resonance is useful in that it opens up the potential for swapping quantum information between the SiV spin and cavity field states, enabling optical SiV state preparation and control through adiabatic following, optically-mediated entanglement of SiVs, and realizing cavity mediated interactions between multiple SiV spin states within the same cavity. A necessary condition to using the cavity field in this three level cQED system is that the cavity linewidth be small relative to the Zeeman splitting. For a cavity with a linewidth of 20 GHz, this would require a magnetic field in excess of 9 T just to reach a spin splitting

comparable to the cavity linewidth. This extreme of a magnetic field poses significant experimental challenges. On the other hand, our composite system with a cavity decay rate of 30 MHz only requires a field of 0.013 T to achieve Zeeman splitting equal to the cavity linewidth.

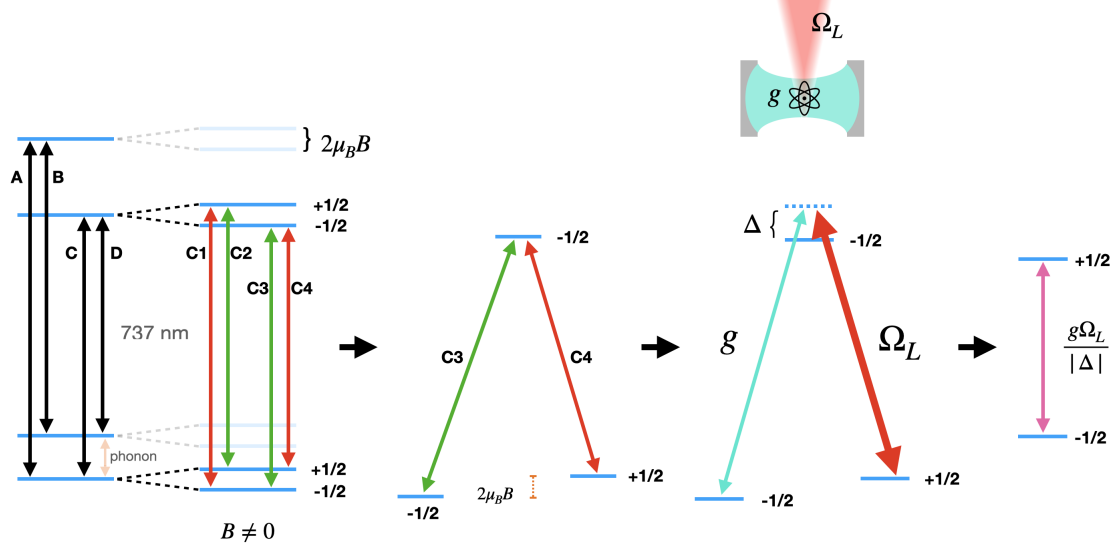


FIGURE 1.3. Example of how the SiV spin state can be optically controlled using a classical laser field  $\Omega_L$  and an optical cavity  $g$  to drive a three-level  $\Lambda$  system when a magnetic field is applied to lift the SiV spin degeneracy. [43]

The cQED system developed in this work is complementary to the photonic crystal design in that it should achieve a three-order magnitude improvement in the cavity linewidth, while at the same time result in a smaller single-photon coupling rate (8 GHz vs 150 MHz) due to the larger mode volumes of WGMs for realistically sized microspheres. While the composite system will likely be limited to lower cooperativities than the photonic system, its high finesse optical cavity should allow for the exploration of cavity mediated control of the SiV spin state that thus far has not been achieved.

## 1.2. Experimental Confirmation of Murphy's Law

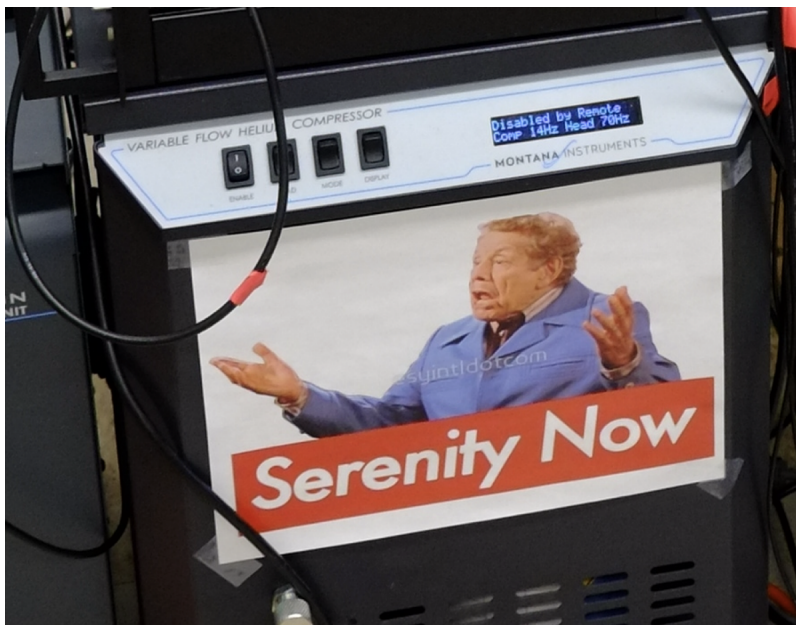


FIGURE 1.4. “Serenity Now!” - a poster haphazardly scotch-taped to the cryostat helium compressor unit.

As I hope will become evident over the course this dissertation, the obstacles that were overcome to reach the point where this project is left at the conclusion of my research were both numerous and incredibly challenging. My intent in including this particular section is to offer some context for the type of challenges that shaped the course of this project and the kinds of tasks that were required to achieve what has been accomplished thus far.

Conceptually, describing the basic mechanics of the experimental system is fairly straight forward: a silica microsphere is moved into contact with a nanometer-thin diamond membrane that allows the cavity to couple to the SiVs within the membrane. Arguably, the general concepts behind the experiments both completed and planned for future work are fairly clear cut as well. In practice, however, the numerous systems required to run this experiment and the

sensitivities of the components used presented numerous challenges that drastically complicated an otherwise “simple” experiment. Many of these challenges at their core stem from one of the factors that motivated the experiment in the first place: silica microspheres and their exceptionally narrow cavity linewidths.

Part of what makes microspheres an interesting candidate for cavities in solid state cQED applications is their ability to reach narrow linewidths that thus far have not been achieved in similar cQED systems. Doing so would open up the possibility of cavity mediated quantum control of the SiV spin qubit. While microspheres offer exceptional cavity linewidths, this comes at the cost of exceptional sensitivity to variables that impact the cavity decay rate and/or mode spectral placement. As an example, consider that silica microsphere optical cavities have been used as bio/chemical sensors for their ability to display measurable mode broadening from the presence of a single protein molecule that has attached itself to the cavity surface. This sensitivity means that factors such as sphere/membrane surface contamination, vacuum quality, and vibration sensitivity left unaddressed can lead to decreased performance from the system, even to the point of the sphere or other elements needing to be replaced.

Considerable work was done developing from scratch, and subsequently, redesigning an experimental platform that could perform all the necessary functions required for positioning and controlling the membrane/sphere/taper system, while also being mounted in the sample chamber of a closed cycle cryostat at 4K. The operation within a closed cycle cryostat presented many challenges, including unexpected contamination sources, nitrogen ice buildup on the microsphere, and significant noise in the cavity transmission spectra due to vibration and sound conduction caused by the operation of the cryostat

compressor and cold head. Ultimately, the task was undertaken to completely redesign and re-fabricate the cryostat system to mitigate the noise issues, and several changes had to be made to operating procedures to prevent contamination from particulates and nitrogen ice. In hindsight, while the Montana Instruments Fusion F2 cryostat utilized for this research was refreshingly easy to use and work with (and fun too!), this project is operating at the limits of what it was designed to do in terms of the high sensitivity to vacuum and vibration performance. As will be shown in later chapters, the data collected suggests that the objective of demonstrating cQED coupling between a microsphere and single SiV is achievable with the experiment in its current state; however, a very large portion of time spent refining the experiment involved working around the limits of the cryostat.

Already delicate procedures, such as the fabrication of double stemmed microspheres and tapered fiber waveguides, were further complicated by the need to accommodate the thermal contraction and expansion they experience over the course of a cryostat cool down/warm up cycle. Left unchanged, the fabrication and mounting procedures used for room temperature experiments would result in spheres snapped by the strain induced from thermal contraction of their two anchor points, as well as tapered fibers that are either too loose to couple effectively or snap during cool down because of the different thermal expansion curves for silica and the Invar steel fork used to mount them.

To further complicate things, the fact that this experiment integrated many delicate systems and components also left it vulnerable to the indisputable fact of nature that in experimentation sometimes stuff just breaks. In this particular case, evidence of Murphy's Law was exceptionally clear from failures with the attocube nanopositioners, tapered fiber waveguides, double stemmed spheres, and cryostat

control electronics. Some issues such as malfunctioning attocubes were simple to address but time consuming to repair. Because they are constructed from thin silica optical fiber, components like double stemmed spheres and tapered fibers could sometimes break under the stress of thermal expansion/contraction from cycling the cryostat as well as occasionally stress from normal use or user error. While the general process of making spheres and tapers is conceptually simple, it is a delicate process requiring very specific techniques and precise handling to successfully produce an end result that checks all the necessary boxes for use in the intended experiments. As a consequence, replacing broken tapers and spheres has tended to be time consuming, typically taking several days to completely finish reloading the cryostat. We also experienced dramatic systems damage on the cryostat due to a power bump in the building's mains power which resulted in cooked electronics that took several months to completely diagnose and correct. This is by no means an exhaustive list of the kinds of obstacles faced in the long series of unfortunate events that was such a major component of this project, but I want to make a point of identifying this, as much of the learning and problem solving involved with this project centered around finding, then fixing, broken things. From my perspective, this particular project being what it is resulted in an effort-in to data-out ratio that is lower than what otherwise might be the norm.

### **1.3. Outline**

Chapter two will examine the underlying physics governing the behavior of atomic systems in cavities in general, and SiVs coupled to a microsphere cavities in particular. After covering the basic properties of a coupled cavity-atom system, I

will provide a theoretical estimate for the likely cQED coupling regime achievable based off the assumed characteristics of the sphere-membrane system.

In the next chapter, I will cover silica microsphere optical cavities, reviewing the physics behind the spatial and spectral characteristics of their optical modes. The method of coupling to microspheres via tapered fiber waveguides will be discussed, as well as the methods and procedures used to fabricate double stemmed microspheres and tapered fibers.

In the fourth chapter, I will discuss silicon vacancy centers in diamond, in particular their physical and electronic structure, optical properties, as well as the specific details of the SiV diamond membranes used in this research.

Chapter five will provide a brief explanation of the dynamics of a cavity coupled to an SiV three-level  $\Lambda$  system in the good cavity limit (a longer term objective of this research) and its application in the exchange of quantum information between the SiV spin qubit and the cavity field.

In the sixth chapter, I will describe the experimental design developed from the ground up for these particular experiments. I will also cover the methods and procedures for preparing the system for experimentation and the experiments themselves, as well as the major obstacles that were overcome to reach the project's current state.

Chapter seven will provide and discuss experimental results characterizing the performance of the cQED system in terms of Q-spoiling and WGM strain tuning. Data will also be provided that characterizes the system's susceptibility to noise when driven by vibration and acoustic conduction into the sample chamber from the operation of the cryostat.



Chapter 8 will cover the results of PL and PLE spectroscopy studies of the composite sphere-membrane system that is used to both demonstrate optical coupling between the SiVs and the cavity as well as verify the optical linewidths of SiVs in the composite system. I will then revisit the theoretical estimates of the cQED coupling strength from chapter two in light of the experimental measurements of both  $\kappa$  and  $\gamma$ .

In the concluding chapter, I will discuss next experimental steps for future work as well as aspects of the experimental system that could be modified and improved upon to achieve better experimental results. Finally, I will conclude with a summary review of the current state of the project, results, and potential for further use.

## CHAPTER II

### CAVITY QUANTUM ELECTRODYNAMICS, AN OVERVIEW

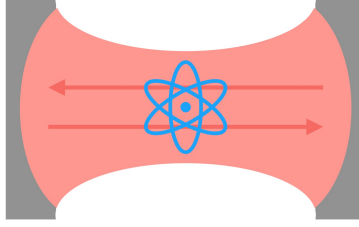


FIGURE 2.1. Cartoon of a simple atom and Fabry-Pérot cQED system.

#### 2.1. Introduction

In this chapter, we will consider the quantum properties and behavior of optical cavities, simple atomic systems, and the dynamics that emerge when the two are coupled via the optical/dipole interaction. We examine these dynamics through the use of the Jaynes-Cummings Hamiltonian for a single cavity field coupled to a single two-level atomic system. The dynamics of a cQED system will be considered by treating the system as two coupled harmonic oscillators to examine the system response to near resonant driving from an externally applied field. This will become relevant in the eventual search for signals indicating successful cQED coupling between microsphere WGMs and SiV optical transitions. I will also provide a theoretical estimate of the single-photon coupling rate for the sphere-membrane system used in this research.

## 2.2. Jaynes-Cummings Model for a Two Level Atomic System

The benefit of using a cavity to couple to an optical transition of an atom or an atom-like system comes from the enhancement of the atomic-optical field interaction that the cavity produces. Here I will provide a brief overview of the basic theory of atom-cavity coupling. The specific model of a single cavity optical mode coupling to a two-level atomic system is described by the Jaynes-Cummings Hamiltonian, which is given by [44],

$$H = \frac{\hbar\omega_o}{2}\sigma_z + \hbar\omega_c a^\dagger a + \hbar g (\sigma_+ a + \sigma_- a^\dagger), \quad (2.1)$$

where

$$\sigma_+ = \begin{pmatrix} 1 & 0 \\ 0 & -1 \end{pmatrix}, \quad \sigma_- = \begin{pmatrix} 0 & 0 \\ 1 & 0 \end{pmatrix}, \quad \sigma_z = \begin{pmatrix} 0 & 1 \\ 0 & 0 \end{pmatrix}. \quad (2.2)$$

Independently, the first term in the Hamiltonian gives the energy level structure of a two-level atomic system. Similarly, the second term alone is the Hamiltonian for an optical field of a particular cavity mode with frequency  $\omega_c$ . The last term is the interaction Hamiltonian linking the cavity and atom. The term  $\omega_c$  is the cavity field frequency,  $\omega_o$  is the atomic transition frequency,  $a$  and  $a^\dagger$  are the raising and lowering operators for the optical field,  $\sigma_+$  and  $\sigma_-$  are the raising and lowering operators for the atomic system, and  $g$  is the single-photon coupling frequency that describes the coupling strength between a single field excitation and the atom. Also known as the vacuum Rabi frequency,  $g$  is defined as,

$$g = \frac{\mathbf{d} \cdot \mathbf{E}}{\hbar}. \quad (2.3)$$

Here  $\mathbf{d}$  is the dipole moment associated with the relevant optical transition, and  $E$  is the electric field at the location of the atom due to a single photon present in the coupling cavity mode. The energy-level structure for the atom alone is just two energy levels with energies  $\pm \frac{\hbar\omega_o}{2}$ , and the energy-level structure for the cavity alone is a ladder with levels evenly spaced by  $\hbar\omega_c$ , where each successive level has one more excitation of the optical field. If there were no interaction term, the eigenstates of the whole system would just be the tensor product of the two different eigen spaces, e.g.  $|e, n\rangle$  or  $|g, n\rangle$ , where  $|n\rangle$  counts the number of photons in the cavity mode, and  $|g\rangle$  and  $|e\rangle$  denote the ground and excited atomic states respectively. However, with the introduction of the interaction term the exact eigenstates become,

$$|n\pm\rangle = \frac{1}{\sqrt{2}} (|e, n\rangle \pm |g, n+1\rangle), \quad (2.4)$$

$$E = n\hbar\omega \pm \hbar\Omega_{n0}, \quad (2.5)$$

$$\Omega_{n0} = 2g\sqrt{n+1}, \quad (2.6)$$

which are now superposition states of the eigenstates of the independent systems, also known as dressed states.

The energy-level structure of the combined system is known as the Jaynes-Cummings ladder. A significant difference between this energy structure and that of the uncoupled case is that when there is zero detuning between the cavity and the atom in the uncoupled system, the states with the same total number of field and atomic excitations are degenerate, while in the Jaynes-Cummings model even at zero detuning the  $|n\pm\rangle$  states are still split by the quantity  $\hbar\Omega_{n0}$ .

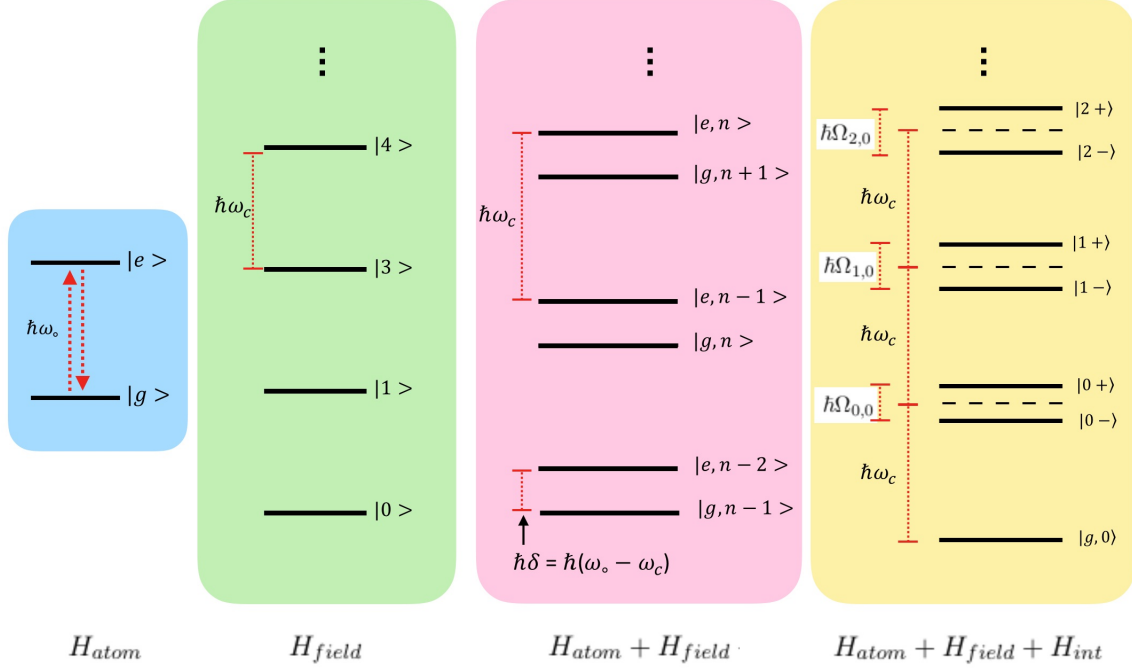


FIGURE 2.2. Energy-level structure for the independent and coupled system Hamiltonians. The energy structure given for the total interaction Hamiltonian is shown for the case when there is zero detuning between the cavity and atomic transition frequencies

### 2.3. cQED in the Linear Regime

It is useful to consider the dynamics of this system using the equations of motion for the expectation values of the field strength and atom polarization in order to incorporate the decay of a realistic cavity and atom. The time evolution of operators in the Heisenberg picture is given by  $\dot{\hat{O}} = \frac{1}{i\hbar}[\hat{O}, H]$ , where the dot notation indicates the derivative with respect to time. From this and the total Hamiltonian of the system, the equations of motion for  $\sigma_-$  and  $a$  are,

$$\dot{a} = -i\omega_c a - ig\sigma_-, \quad (2.7)$$

$$\dot{\sigma}_- = -i\omega_o\sigma_- + ig a\sigma_z, \quad (2.8)$$

We can then add decay terms to these equations, describing finite cavity lifetimes and spontaneous decay of the two level system. When adding decay terms to these equations of motion, we must also introduce Langevin noise operators,

$$\dot{a} = -i\omega_c a - ig\sigma_- - \kappa a + F_a, \quad (2.9)$$

$$\dot{\sigma}_- = -i\omega_o\sigma_- + ig a\sigma_z - \gamma\sigma_- + F_{\sigma_-}, \quad (2.10)$$

Where  $F_{\sigma_-}$  and  $F_a$  are Langevin noise operators, and  $\kappa$  and  $\gamma$  are the introduced decay rates for the cavity and atom respectively. The decay rate  $\kappa$  represents optical loss of the cavity, and  $\gamma$  represents the spontaneous decay rate of the atomic excited state. Next, we take the expectation value of these equations.

$$\langle \dot{a} \rangle = -i\omega_c \langle a \rangle - ig \langle \sigma_- \rangle - \kappa \langle a \rangle + \langle F_a \rangle \quad (2.11)$$

$$\langle \dot{\sigma}_- \rangle = -i\omega_o \langle \sigma_- \rangle + ig \langle a\sigma_z \rangle - \gamma \langle \sigma_- \rangle + \langle F_{\sigma_-} \rangle \quad (2.12)$$

The noise terms drop out since  $\langle F_i \rangle = 0$ . If we consider the case of a weakly excited atom where  $\langle \sigma_z \rangle \approx -1$ , we can linearize the term  $\langle a\sigma_z \rangle \approx -\langle a \rangle$ . We can also rewrite  $p = \langle \sigma_- \rangle$ , and  $\alpha = \langle a \rangle$  where  $p$  and  $a$  are the expectation values of the atomic polarization and the cavity field strength, respectively. The equations of motion then become,

$$\dot{\alpha} = -(i\omega_c + \kappa)\alpha - igp, \quad (2.13)$$

$$\dot{p} = -(i\omega_o + \gamma)p - ig\alpha, \quad (2.14)$$

which describes two coupled harmonic oscillators. Considering the case when there is zero cavity-atom detuning ( $\delta = \omega_c - \omega_o = 0$ ), and switching to the rotating frame ( $p = \tilde{p}e^{-i\omega t}$ ,  $\alpha = \tilde{\alpha}e^{-i\omega t}$ ), we can solve for the motion of the system

$$\dot{\tilde{\alpha}} = -\kappa\tilde{\alpha} - ig\tilde{p}, \quad (2.15)$$

$$\dot{\tilde{p}} = -\gamma\tilde{p} - ig\tilde{\alpha}, \quad (2.16)$$

using the solution  $\tilde{\alpha} = \alpha_o e^{\lambda t}$  and  $\tilde{p} = p_o e^{\lambda t}$ . For the weak coupling regime when  $\kappa \gg g \gg \gamma$ ,  $\lambda$  simplifies to  $\lambda_+ = -\gamma - \frac{g^2}{\kappa}$ , demonstrating how the cavity enhances the atomic decay rate. This also suggests a useful figure of merit for characterizing the coupling between the atom-cavity system. The ratio between the intrinsic atomic decay rate and the enhancement is

$$C = \frac{g^2}{\kappa\gamma}, \quad (2.17)$$

which is known as the cooperativity. When  $C \gg 1$ , the atomic transition and cavity mode are strongly coupled and the transition becomes susceptible to the applied field on the scale of single photons. This also means that the presence of the atom in the cavity will begin to significantly impact the optical characteristics of the cavity.

In the case of strong coupling  $g > (\gamma, \kappa)$ ,  $\lambda$  takes the form  $\lambda_{\pm} = -\frac{1}{2}(\gamma + \kappa) \pm ig$ , which demonstrates two normal modes of the system in addition to the decay with separation  $2g$ . So we again find the splitting of dressed states that we see in the solution for the exact Hamiltonian.

If we consider the case where an external field  $A$  is coupled into the cavity at a rate  $\kappa_{ex}$ ,

$$\dot{a} = -(i\omega_c + \kappa)\alpha - igp + \kappa_{ex}A, \quad (2.18)$$

we can examine the case when the cavity has reached a steady state field to look at the cavity field as a function of driving frequency. Assuming the cavity and atom again have negligible detuning, and that the cavity and polarization oscillate at the same frequency as the driving field ( $\omega$ ), the cavity field and atomic polarization are given by

$$\tilde{\alpha} = \frac{\kappa_{ex}\tilde{A}_o}{(\kappa + i\delta) + \frac{g^2}{\gamma + i\delta}}, \quad (2.19)$$

$$\tilde{p} = \frac{-ig}{i\delta + \gamma} \frac{\kappa_{ex}\tilde{A}_o}{(\kappa + i\delta) + \frac{g^2}{\gamma + i\delta}}. \quad (2.20)$$

Figure 2.3 shows the field intensity and atom polarization as a function of detuning of the driving field for the good cavity ( $g > \kappa$ ), bad cavity ( $g < \kappa$ ), and strong coupling ( $g > (\kappa, \gamma)$ ) limits. In the strong coupling case, we can resolve the two different dressed states of the combined system as two resonances separated by  $2g$  present in both the cavity and polarization response spectra. While strong coupling would be the best case outcome of our system, cQED coupling of the system can still be observed in both the good and bad cavity limits as well. For the good cavity limit, the optical transition with a much greater decay rate will effectively damp the cavity mode as energy is exchanged between cavity and atom and lost through decay via fluorescence. This is evident as a broadening of the cavity linewidth when the coupled atom is both resonant and optically active such that the zero detuned transition can be driven. The atomic polarization will appear as it normally would without the presence of the cavity except for a dip that lines up with the resonance frequency of the cavity. The depth of the dip in



the atomic polarization is determined by the cooperativity of coupled cavity-atom system. Experimentally, atomic polarization will correspond to fluorescence data from photoluminescence excitation spectroscopy (PLE). The case of the bad-cavity limit essentially mirrors that of the good-cavity limit with the roles reversed where the cavity then becomes the mechanism that damps the atom. Other intermediate coupling regimes could be considered as well, but the essential characteristics of cQED coupling are sufficiently depicted by the three cases considered here.

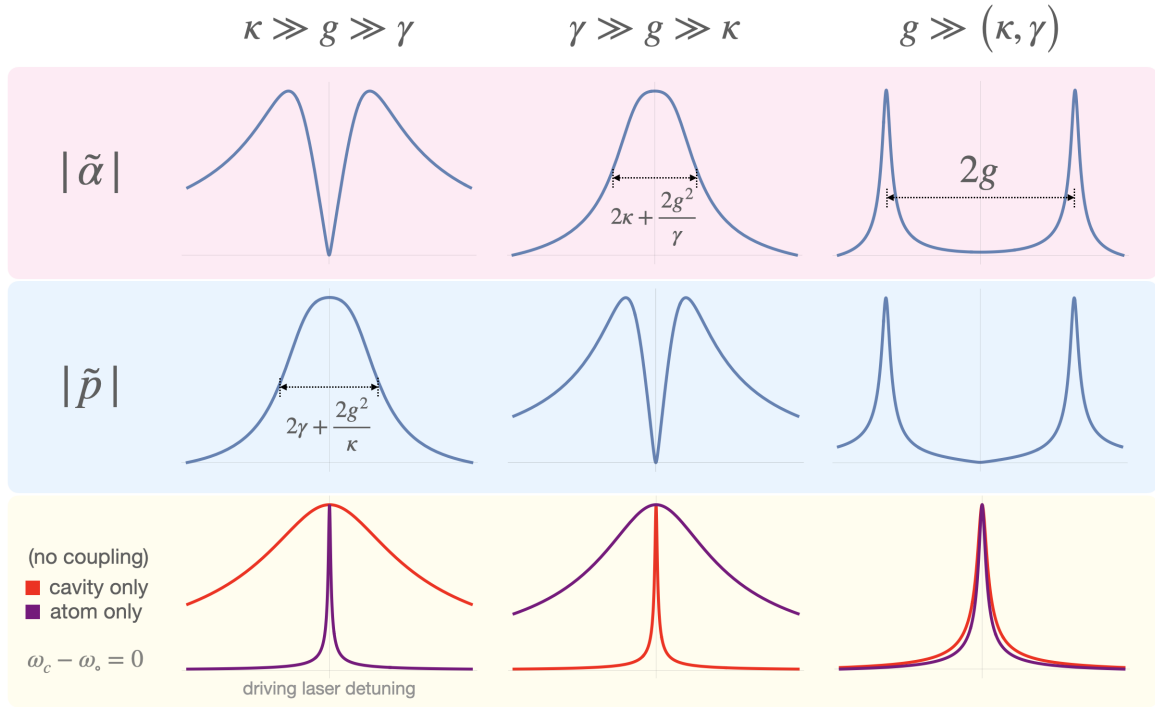


FIGURE 2.3. Plots of the cavity field and atomic polarization for steady state driving of the cavity field in the bad cavity, good cavity, and strong coupling limits. The cavity mode is zero-detuned from the atomic transition

## 2.4. Theoretical Estimation of cQED Performance of the Sphere-Membrane System

As a sanity check, it is worth using the known parameters of the sphere-membrane system and realistic estimate of what is practically achievable in the lab to make a theoretical calculation of the single-photon dipole coupling rate  $g$  to both verify the feasibility of the system and clarify the kinds of signals in the PLE and transmission data to search for. This was found by first using the MATLAB package WGMmode [45] to model a 737 nm equatorial cavity mode within a microsphere with a 30  $\mu m$  diameter. The mode volume was found to be 110  $\mu m^3$ . The optical field strength was then normalized to have the same energy of a single cavity photon of  $\hbar\omega_c$  using the relation for the mode volume,[46, 47]

$$V_{mode} = \frac{\int \epsilon(\mathbf{r}) |\mathbf{E}|^2 d^3r}{\max(\epsilon(\mathbf{r}) |\mathbf{E}|^2)}, \quad (2.21)$$

where  $\epsilon(\mathbf{r})$  is the permittivity as a function of  $\mathbf{r}$ . This then made it possible to determine the optical field strength at any point of the cavity mode. The electric field strength was found for a distance of 25  $\mu m$  away from the sphere surface along the equator. This corresponds to what should be the case with our current membrane sample given the thickness of the membrane and the SiV implantation depth. Using the transition dipole value of 14.3 Debye for the SiV C transition[48], a coupling rate of  $g/2\pi = 150$  MHz was found. This takes into account the potential mismatch between the cavity mode polarization and the SiV axis. For the case of an optical transition with a linewidth of  $\gamma/2\pi = 200$  MHz and an equatorial WGM with linewidth of  $\kappa/2\pi = 40$  MHz, this gives a cooperativity of  $C = 4g^2/\kappa\gamma = 11$ , well within the regime where cQED effects should be

observable in both cavity transmission and SiV fluorescence measurements. The

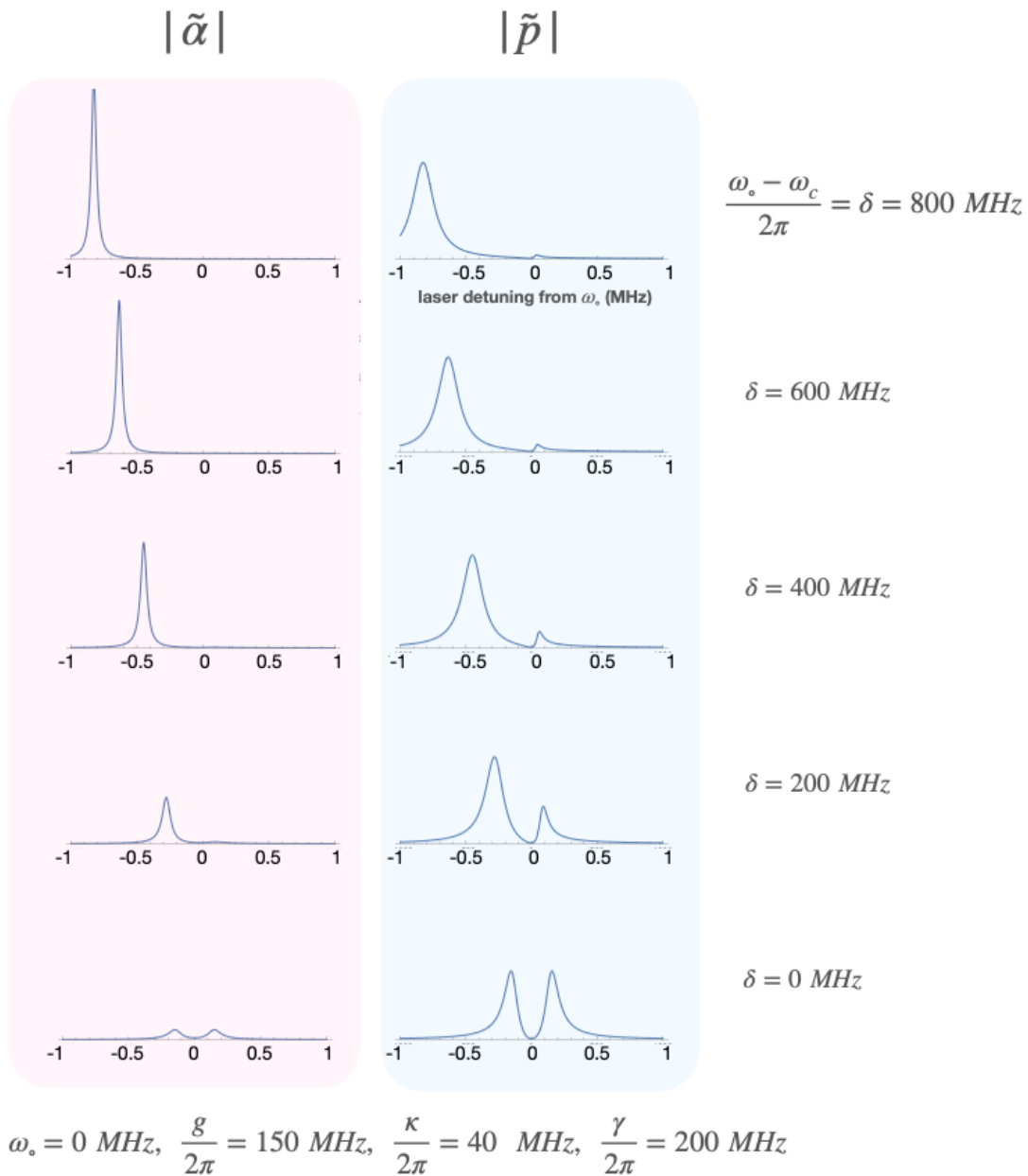


FIGURE 2.4. Plots of the steady state cavity field and atomic polarization for cQED parameters matching the estimates for the SiV-microsphere system. Both are plotted for various values of the cavity-atom detuning.

30  $\mu\text{m}$  diameter sphere is smaller than what is typically employed by most of our experimental runs to simplify the fabrication process but is still certainly

achievable.[49] A larger sphere in the 60  $\mu m$  range should still result in detectable coupling, but the coupling rate will be reduced due to a diminished evanescent field and increased mode volume. The calculation of the single-photon coupling rate also utilized the worst case polarization coupling scenario. In a mono-crystalline diamond, the SiV axis has four possible orientations, corresponding to the four different orientations of carbon-carbon bonds present. For a given optical-field polarization, the dot product of the optical field with the SiV C-transition dipole moment will vary depending on the orientation of the SiV axis. The calculation used to determine the single-photon coupling rate was for the case when the projection of the field polarization onto the most optimally aligned SiV axis was minimized. In other words, for any other case of membrane orientation relative to the WGM, the projection of the polarization onto at least one family of SiV orientations would be increased, resulting in a higher single-photon coupling rate than what is calculated here, at most a 1.7x improvement in  $g$ .

## CHAPTER III

### SILICA MICROSPHERE OPTICAL CAVITIES

#### 3.1. An Introduction to Optical Cavities

The simplest example of an optical cavity is the Fabry-Pérot cavity, which is constructed with two opposing mirrors. Photons trapped within the cavity will be reflected back and forth between the two mirrors. Due to interference effects within the cavity, modes with wavelengths that evenly divide the cavity path length will constructively interfere and are enhanced inside the cavity, whereas all other wavelengths of light will destructively interfere and be suppressed within the cavity. The mode spectrum for this system is a set of resonances evenly spaced by a frequency separation known as the free spectral range, which is given by,

$$\omega_{FSR} = 2\pi \frac{c}{n_s l}, \quad (3.1)$$

where  $n_s$  is the index of refraction of the cavity medium,  $l$  is the cavity path length, and  $c$  is the speed of light in vacuum. In a perfect cavity with 100% reflecting mirrors and no loss mechanisms, photons trapped within the cavity will circulate forever and only modes with exactly the cavity resonance frequency will be supported in the cavity. The resonances for such a cavity are delta functions in frequency space. In actuality, imperfect mirrors or other loss mechanisms in the cavity mean that a photon will have a finite lifetime propagating within the cavity. This finite lifetime ( $\tau$ ) leads to cavity resonances which are broadened into a smooth peak. The width of those resonance peaks directly gives the decay rate ( $\kappa$ ) of the cavity which is related to the cavity lifetime by  $\kappa = \frac{1}{\tau}$ . A useful figure of

merit for describing the ability of a cavity to confine optical energy is the quality or  $Q$  factor:

$$Q = \omega \left( \frac{E_{stored}}{P_{diss}} \right) = \frac{\omega}{\kappa}, \quad (3.2)$$

Which is the ratio of the average energy stored in the cavity to the energy dissipated per round trip. The utility of an optical cavity comes from its ability to spatially and temporally confine light. An external field that is coupled into an optical cavity will lead to a buildup of the cavity field such that the field intensity of the cavity mode is orders of magnitude greater than the applied field.

Fabry-Pérot cavities, while conceptually simple can be more difficult to implement in a cavity-QED system due to of their fabrication methods, mode volume, and limited quality factors. Another type of optical cavity that is the type used in this research is a silica microsphere. In an ideal (perfectly spherical and uniform) microsphere optical cavity, light propagating within the cavity is constrained within the sphere via total-internal reflection at the silica/vacuum boundary due to the discrete change in the index of refraction. This results in optical modes in which the field circulates about an axis of the sphere, generally close to the surface, in what are known as whispering gallery modes (WGMs). In the case of a microsphere formed at the tip of a silica fiber stem, typically, the stem will define the axis of the sphere. In a similar way to how light of a particular frequency within a Fabry-Pérot cavity will constructively interfere to form an optical standing wave within the cavity, in microspheres, light of the proper frequencies will circulate within the cavity and constructively interfere with itself if, upon a complete orbit of its path length, its phase matches the same as it was at the beginning of the path. One distinction is that typically for microspheres, this results in constructive interference as a traveling wave.

### 3.2. Whispering Gallery Mode Solutions

The field solutions to WGMs in a spherical optical cavity can be found by solving Maxwell's field equations, leading to the wave equation,

$$\nabla^2 \mathbf{E} + n^2 k^2 \mathbf{E} = 0, \quad (3.3)$$

where  $n$  is the index of refraction and  $k$  is the free space optical wave number.

Because the system being solved is spherically symmetric, this can be reduced to the scalar wave equation,[50]

$$\nabla^2 \psi + n^2 k^2 \psi = 0. \quad (3.4)$$

The electromagnetic field for the cavity is reduced to two cases of either transverse-electric (TE) or transverse-magnetic (TM) polarization orientations, where the radial component of the electric and magnetic fields are zero in their respective cases. These two different mode families are given by

$$\mathbf{E} = \nabla \times (\mathbf{r}\psi), \quad (3.5)$$

for TE modes and,

$$\mathbf{E} = \nabla \times \nabla \times (\mathbf{r}\psi), \quad (3.6)$$

for TM modes. The general solution for  $\psi$  is described by,[51]

$$\psi_{lm}(r, \theta, \phi) = z_l(nkr)Y_{lm}(\theta, \phi), \quad (3.7)$$

where  $Y_{lm}(\theta, \phi)$  are the spherical harmonics and  $z_{lm}(nkr)$  are the spherical Bessel functions. A physical solution to this equation requires that  $\psi$  be finite at the origin and approach zero as  $r$  approaches infinity. For a silica sphere with index  $n$  and radius  $R$  situated within a vacuum, the solution to the scalar wave equation is constrained to the form

$$\psi_{lm}(r, \theta, \phi) = \begin{cases} \sum_{lm} a_{lm} j_l(nkr) Y_{lm}(\theta, \phi) & r \leq R \\ \sum_{lm} b_{lm} h_l^{(1)}(nkr) Y_{lm}^{(1)}(\theta, \phi) & r > R \end{cases} \quad (3.8)$$

where the function  $h_l^{(1)}(kr)$  for the case  $r > R$  is the spherical Hankel function of the first kind. Boundary conditions at the sphere surface require the continuity of  $\psi$ , as well as the continuity of the derivative of  $\psi$  with respect to  $r$ . This leads to the addition constraints,

$$b_{lm} h_l^{(1)}(nkR) = a_{lm} j_l(nkR), \quad (3.9)$$

and

$$nlj_{l-1}(nkR) - n(l+1)j_{l+1}(nkR) - \frac{j_l(nkR)}{h_l^{(1)}(nkR)} \left[ lh_{l-1}^{(1)}(kR) - (l+1)h_{l+1}^{(1)}(kR) \right] = 0. \quad (3.10)$$

Cavity mode solutions are then determined by finding the roots to equation 3.10, which can be solved computationally. The respective TE and TM WGM solutions for the spherical cavity are described by the characteristic mode numbers  $\mu$  (radial),  $l$  (angular momentum), and  $m$  (z angular momentum), where  $\mu$  is denoting the solution which gives the  $\mu^{th}$  root to equation 3.10.



The mode number  $\mu$  counts the number of field lobes along the radial direction moving from the center of the sphere outwards towards the equator. The mode number  $l$  determines the number of field maxima crossed making a complete trip about the sphere's equator. Lastly, the value of  $l - m + 1$  determines the number latitudinal bands to which the mode is confined. When  $l$  and  $m$  are equal, the mode is constrained to propagate along a single band around the equator, known as equatorial modes.[52, 53] As will be discussed later, these are the particular modes desired for use in this experiment. This stems from the fact that equatorial modes have the smallest mode volumes that are needed to achieve the greatest cavity/atom coupling rate possible. Additionally, only  $\mu = 1$  modes are used. Higher radial number modes have both a larger mode volumes and reduced evanescent field intensity making them less desirable for cavity coupling experiments.

For a perfect sphere, all modes with the same  $n$  and  $l$  will be degenerate in their resonance frequencies. For a realistic sphere, however, subtle defects such as slight eccentricity, local aberrations, or local changes to the index of refraction will cause modes with different values of  $m$  to have their degeneracy lifted. This results from modes that occupy different volumes of the cavity experiencing a slightly different round trip distance and result in a frequency perturbation from the case of an ideal sphere. [40]

One key feature of WGMs is the evanescent field that extends outside the cavity surface. Because the cavity field is contained due to total internal reflection, there is an evanescent field component that propagates around the sphere external to the cavity. The strength of this evanescent field is well approximated by the

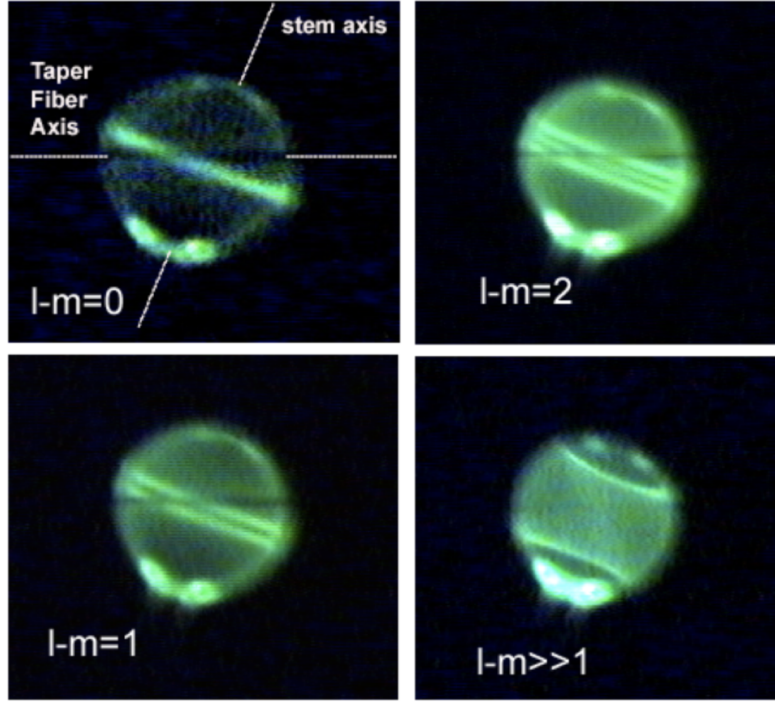


FIGURE 3.1. Micrographs visualizing the cavity mode distribution of several modes with different  $l$  and  $m$  values. [40] The silica sphere is doped with erbium atoms which fluoresces due to the cavity field.

exponential decay,[54]

$$\mathbf{E} \propto \exp\left(i\frac{2\pi}{\lambda} \frac{s}{(1-n)^{1/2}}\right) = \exp\left(-\frac{s}{\tau}\right) \quad (3.11)$$

where  $s$  is the distance from the sphere surface,  $l$  is the characteristic decay length of the evanescent field, and  $\lambda$  is the WGM resonance wavelength. For the spheres used in this project,  $l$  was a few hundred nanometers, varying depending on the cavity diameter. The presence of the evanescent field is key to this project because it enables the cavity to couple to the diamond membrane as well as the tapered fiber waveguide which allows measurements of the cavity transmission spectrum and the collection of any light that couples into the WGMs. When another media

is brought into the external evanescent field, the overlap allows for the evanescent field to couple to the optical modes supported by the adjacent object. Effectively, the evanescent overlap allows light to tunnel from the cavity to the waveguide, sample, etc..

### 3.3. Coupling to a Microsphere via Tapered Optical Fiber Waveguide

With a WGM optical cavity, we need some way to couple an external optical field into and out of the cavity in order to drive the WGM and monitor the transmission of the system. Because of the difference in indices of refraction between the silica and external vacuum (or air), coupling a free space laser to the cavity is highly inefficient. Most of the light is simply scattered.[55] This can be made more efficient by fabricating resonators with outer diameters that are slightly elliptical; however, a simpler, more efficient alternative is to use a tapered optical fiber (which is roughly index matched) to couple to the cavity.[56, 57] By stretching an optical fiber so that it has a smooth transition from full diameter ( $125\text{ }\mu\text{m}$ ) to only a few microns, more and more of the optical mode will be outside of the taper, propagating as a decaying evanescent field. By bringing the tapered fiber to a short distance from the cavity, the taper evanescent field will overlap with the cavity mode and light will couple into the cavity, essentially tunneling from the taper to the cavity. This similarly allows light to couple from the cavity back into the taper, which can then be detected at the fiber output.[40]

The overlap between the two modes is increased by bringing the fiber closer to the sphere, which results in a higher  $\kappa_{ex}$ , which should be thought of as both the rate that light is coupled into the cavity mode as well as the decay rate of the cavity due to loss out through the tapered fiber. In addition to  $\kappa_{ex}$ , every sphere

also has some intrinsic cavity decay rate,  $\kappa_o$ , which is actually the sum of the decay rates for the various loss mechanisms of the cavity. These loss mechanisms include things such as scattering from surface deformations, absorption/scattering from surface contamination, and the small but non-zero absorption coefficient of silica. Another source of loss comes from absorption due to water on the cavity surface. In normal ambient conditions, water vapor in the air will deposit on the sphere surface creating a mono-layer of water molecules that have an increased rate of absorption compared to silica. Whereas the intrinsic coupling rate is due to properties of the sphere,  $\kappa_{ex}$  is dependant solely on the geometry of the taper/sphere system. One benefit to the use of tapered fiber wave guides is their ability to selectively couple to certain groups of WGMs depending on their position relative to the sphere. A tapered fiber position at or near the equator will couple strongly to modes with a small  $l - m + 1$  values. Similarly, a taper coupled to a sphere nearer to the poles will preferentially couple to modes with large  $l - m + 1$  values. Since this project depends on the use of equatorial and near equatorial modes, the positional dependence on taper fiber coupling offers a tool for simplifying the process of coupling to and identifying the necessary WGMs.

The actual transmission spectrum of an individual cavity mode will vary with the taper-sphere distance. If light is sent into the tapered fiber at one end and the output of the tapered fiber is measured with a photo-detector, when the taper is removed from the sphere, the spectrum will be a constant power with respect to laser frequency. As the taper is lowered and the modes begin to overlap, a dip in the transmission spectrum will begin to appear, which corresponds to the WGM resonance. Light is being coupled into the cavity, and due to the other decay mechanisms, some of the light is lost via scatter or absorption which results in

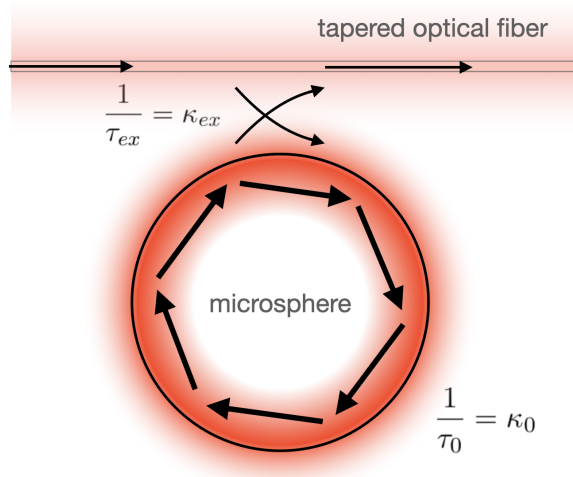


FIGURE 3.2. Illustration of the optical coupling between sphere and taper via overlapping evanescent fields.

reduced transmission. Transmission spectrum for a WGM is given by

$$T = \left| \frac{\kappa_{ex} - \kappa_0 - i\delta}{\kappa_{ex} + \kappa_0 + i\delta} \right|^2 \quad (3.12)$$

where  $\delta$  is the detuning of the driving laser field relative to the WGM resonance frequency, not to be confused to the atom-cavity detuning from chapter 2. Note that this function is a lorentzian and the linewidth (full width at half max) is simply  $\kappa_{ex} + \kappa_o$ . As the taper is brought closer to the sphere, the transmission on resonance will decrease and the linewidth of the dip will expand as the total cavity decay rate increases with  $\kappa_{ex}$ . This regime where  $\kappa_{ex} < \kappa_o$  is referred to as being under coupled.

When  $\kappa_{ex} = \kappa_o$ , the system is referred to as critically coupled. While light is coupled into the cavity, there is a  $\pi$  phase difference between the fiber waveguide mode and cavity mode coupling back into the fiber. This results in total destructive interference which leads to a complete extinction of the cavity

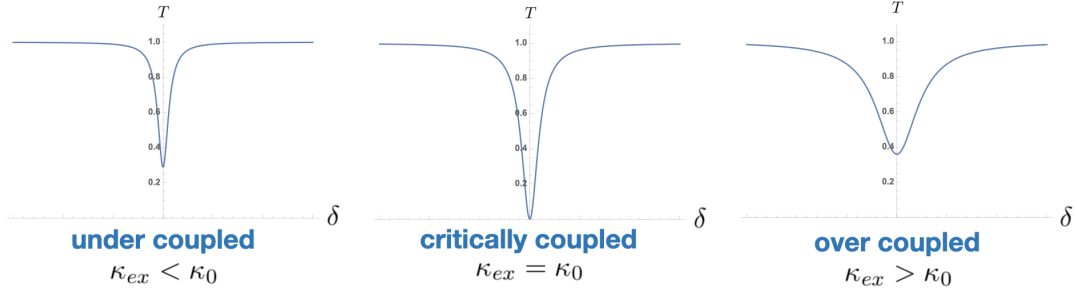


FIGURE 3.3. Plots of the cavity transmission spectrum for a single WGM in under coupled, critically coupled, and over coupled regimes.

transmission when precisely on resonance with the WGM. The case of  $\kappa_{ex} > \kappa_o$  is referred to as over coupled. As the sphere-taper gap is further reduced, the transmission on resonance begins to rebound as the cavity linewidth continues to expand. In this case, most of the cavity loss comes from light coupling back into the taper leading to increased fiber transmission.

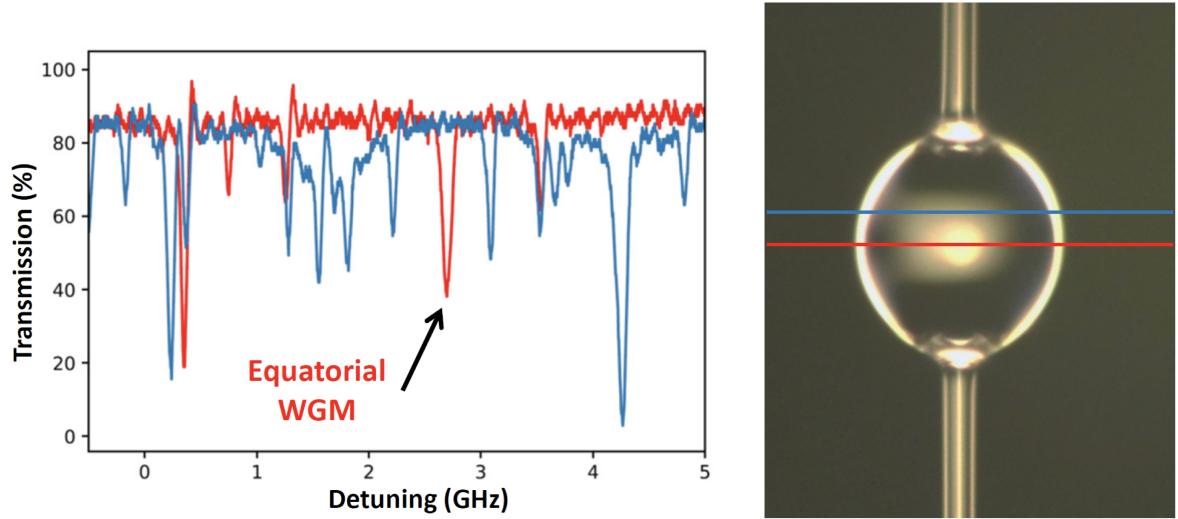


FIGURE 3.4. Cavity mode transmission for the case of a tapered fiber aligned with the equator (red) and the case a of taper positioned away from the equator (blue). The presence of a specific WGM in the red spectrum while being absent in the blue spectrum indicates it is an equatorial mode.

### 3.4. WGM Strain Tuning

For silica microspheres, the fabrication process (discussed in the following section) does not result in perfectly controlled and reproducible cavities.[40] That is, we do not have precise control of the sphere size while fabricating it. Very slight differences in the subtle asymmetries of the sphere results in essentially no control over the resulting modes structure for each sphere. This fact, in tandem with the need to have control of the frequency detuning between cavity modes and SiV transitions for cQED experiments, necessitates a means for shifting cavity modes in a controlled repeatable manner. In the case of the research done by Lukin et. al using monolithic diamond optical lattice cavities, this is achieved by incrementally depositing or evaporating minute amounts of nitrogen gas on to the cold cavity.[21] The presence of the nitrogen causes a change in the effective index of refraction of the cavity, changing the frequencies for which light can constructively interfere within the cavity forming cavity modes.

As will be discussed in the following chapter, nitrogen deposition onto the cavity due to the inherent leak rate of the cryostat sample chamber results in unwanted Q-spoiling brought about by scattering and absorption of the modes via the deposited nitrogen. Without changing the effective index of refraction, the only other method to tune the cavity modes requires modifying the cavity path length itself. This can be accomplished by stretching the sphere along the stem axis.[52, 53, 58, 59] For tension tuning of the cavity modes, a second stem opposite and parallel to the first is necessary to allow for two separate mounting points. When tension is applied to the cavity, it causes it to deform very slightly from its normal geometry, essentially slightly elongating it along the direction of the stem axis and reducing the circumference around the equator slightly, which in turn,

leads to a blue shift of the WGM relative to its natural position in frequency. A second concurrent mode of tuning comes from the change in refractive index of the silica due to the applied tension. Strain modulation of the cavity optical length is by far the dominant tuning mechanism. The frequency shift is approximately linear and is given by,

$$\Delta\omega = \frac{\Delta d}{d}\omega \quad (3.13)$$

where  $d$  is the diameter of the microsphere. Divergences from a linear response in a measured tuning curve is typically due to the smaller strain induced modulation of the index of refraction. [58]

Key advantages to this means of cavity tuning over the use of nitrogen deposition are that it is both fast, quickly reversible, and precise. The change in WGM mode frequency is immediate as the tension is changed, and there is no functional difference between tuning in the positive or negative direction. In the case of this project, tuning was accomplished using an attocube ANP/x/101/LT nanopositioner. This positioner features both a course grain step function for large scale movements, as well as a continuous fine grain positioning mode in which a DC offset signal is used to control a piezoelectric crystal. When using the DC offset mode, the precision of the tuning is functionally limited only by the precision and noise limit of the voltage supply used to control the attocube. For the 0.1 V step size of the ANM 300 attocube controller used for this project, that practically means that the resolution of tuning control is well below even the 10MHz and less linewidths of non-equatorial modes of a completely intact sphere.



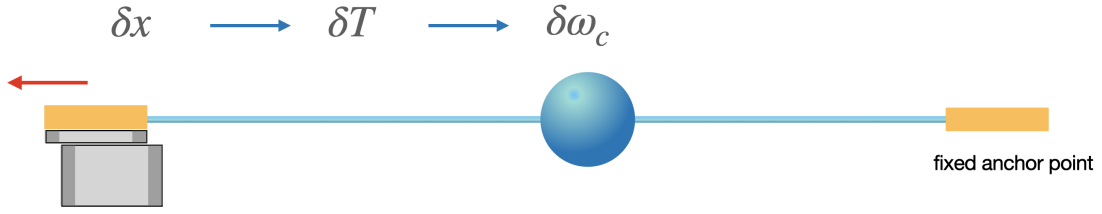


FIGURE 3.5. Illustration depicting the process of WGM resonance tuning via tension provided by an attocube nanopositioner. Displacement of the nanopositioner causes a change in the stem tension which causes a small deformation of the cavity geometry, and in turn results in a frequency shift of the cavity resonance.



FIGURE 3.6. Like beads of water, molten silica will naturally relax into a spherical geometry from the presence of surface tension.

### 3.5. Fabricating Double Stemmed Microsphere Cavities

For a portion of this research, bottle resonators were used in place of microspheres because of their simpler fabrication methods and physical strength while still allowing for strain tuning.[52, 53] However, this was later dropped in favor of returning to double stemmed microspheres, as the non-spherical geometry of the bottle resonators made focusing of the resonant and off-resonant laser beams onto the membrane extremely difficult. For fabricating both silica

microspheres and tapered fiber waveguides, we use methods similar to those outlined by Kippenberg[40], with several modifications in particular for the fabrication of double-stemmed spheres (DSS). Silica microspheres are fabricated by melting/reflowing bare silica optical fiber with a high power CO<sub>2</sub> laser. CO<sub>2</sub> lasers emit at 10.6 microns. That wavelength has an extremely high absorption coefficient for silica, making it efficient at melting silica when focused down to a sufficiently small beam spot. The laser used is a Synrad 32-1SAC 5 watt CO<sub>2</sub> laser. Power modulation of the laser is achieved by modifying the duty cycle of square wave generated from an arbitrary function generator (AFG) that is fed to the laser's gating input. The beam of the laser is then sent through a convex ZnSe long IR lens with a 80 mm focal length to focus the beam down to a point. The focusing lens is mounted on a three axis positioning stage to allow alignment of the beam path past the lens.

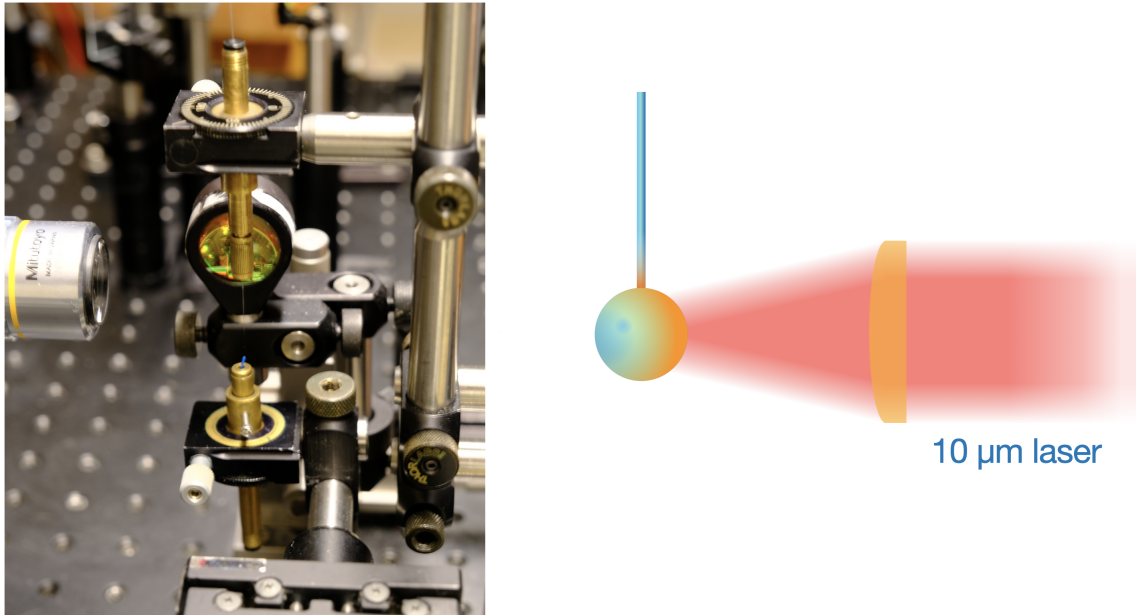


FIGURE 3.7. System for making double stemmed microspheres. Top and bottom fiber chucks are visible, with the CO<sub>2</sub> laser focusing lens visible behind the top fiber chuck, and the imaging objective visible to the left.

The process of making microspheres, especially DSSs, is very sensitive to the laser power. The CO<sub>2</sub> laser naturally has a periodic power fluctuation of about 10 percent with a characteristic fluctuation timescale of tens of seconds. When the pulse width of the gating signal is significantly below the 200  $\mu$ s rise time of the laser, the power fluctuations are even more exaggerated. This means that without attenuation, the laser power can be adjusted to effectively reflow the sphere, but over time, the power will climb to the point of beginning to vaporize the sphere or drop to the point that no reflow occurs. For this reason, a SnZN 50:50 beam splitter and a high absorptive reflector (glass slide) are used to attenuate the laser beam before it passes through the focusing lens. This allows for running the laser with longer pulse widths while maintaining a usable amount of IR power incident on the sphere. As a consequence, the appropriate power for reflowing the sphere is achieved, but at a driving power further above the lasing threshold resulting in a more stable power output.

Two three-axis translations stages hold rotation stages used to mount the fiber chucks that hold the two fibers stems used to make a DSS. Each stage axis is controlled using a manually operated micrometer. A 10x objective is used with a CCD detector and display to image the fiber during the fabrication process. The objective is aligned so that its field of view coincides with the beam waist of the laser.

Fabricating double stemmed spheres was by far the most delicate procedure required to prep the cryostat system for an experimental run. A portion of optical fiber is threaded through a fiber chuck that will later be used to mount it in the CO<sub>2</sub> laser setup. A fiber stripper is used to remove the plastic jacket from a roughly 2 cm section of fiber, which is then placed in the hydrogen torch pulling

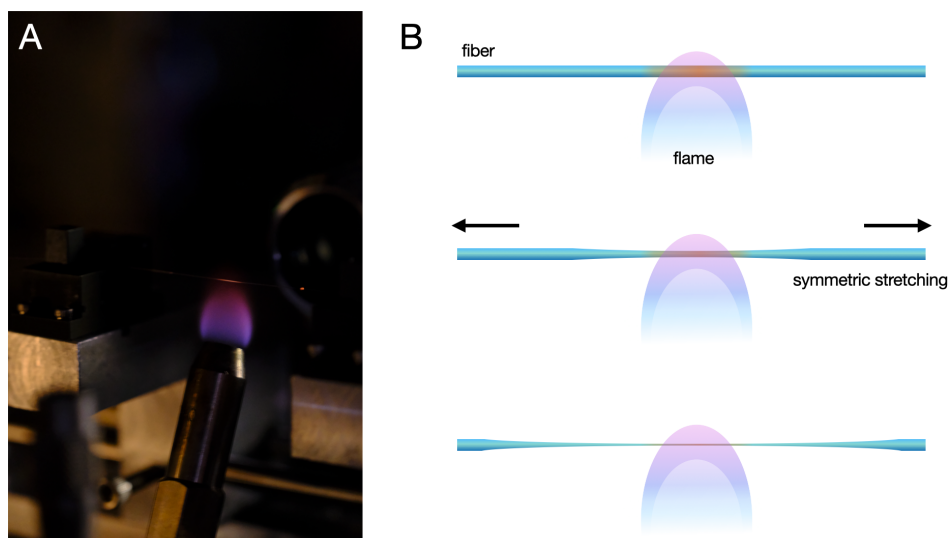


FIGURE 3.8. A) The hydrogen torch heating optical fiber while stretching it. B) An illustration of the stretching process.

system and clamped down. The torch is then ignited and the fiber stretched as the fiber waist is observed on a CCD camera. The torch and pulling are stopped once the fiber waist reaches around 20 microns. The fiber is then removed and brought to the CO<sub>2</sub> laser where the fiber chuck is mounted on a x-y-z translation stage to allow the fiber to hang in the beam path of the CO<sub>2</sub> laser. A small piece of aluminum foil is then attached to the dangling end of the fiber using a section of kapton tape to act as a ballast. Other kinds of tape will not work as they require some level of pressure to adhere to the fiber, which typically results in enough shearing force to break the fiber. Most of the time, electrostatic forces cause the hanging fiber to be repelled by the kapton tape making it difficult to make contact with the fiber. By lowering the fiber and first bringing it in contact with the foil, it will be attracted/stick to the foil, which helps to mitigate the repulsive static force between the fiber and tape. Once the lower portion of the hanging fiber has gently stuck to the foil, the fiber can then be gently adjusted to bring the rest in contact with the kapton tape.

The imaging CCD is used to find the CO<sub>2</sub> beam waist, and the fiber is raised until the diameter of the fiber in the beam path is just slightly larger than the target width for the stem at the base of the sphere. The CO<sub>2</sub> laser is then used at high power, causing the fiber to melt and the fiber segment below the laser spot to fall off. The presence of the weight attached to the bottom of the fiber is what enables the removed stretch of fiber to drop away when it is cut with the laser. If no weight is used, the force of gravity on the excess fiber alone is not enough to counteract the force of surface tension when the silica is melted and the fiber will only be deformed.

The CO<sub>2</sub> laser power is then turned down and used to melt the tip of the fiber enough to form a small sphere not much larger than the fiber diameter at that point. The fiber is then removed from the chuck and cut so that there is only 1-2 cm of un-stripped fiber remaining. The un-stripped portion of this taper is inserted into the emptied out 500  $\mu\text{m}$  jacket of a FT200-EMT multimode fiber, which is itself mounted in a second fiber chuck. This taper will eventually form the bottom stem of the DSS. Inserting it into an empty fiber jacket allows it to be held in a fiber chuck for positioning, and because it is only being held by the friction of the jacket, it is possible to pull it out of the chuck using minimal force, allowing it to be removed without the DSS breaking under the tension of removing it.

This process is repeated a second time, except in the second iteration, the fiber is cut with the laser at a much thicker point than the first, leaving extra material that will form the body of the sphere. The laser is then used to reflow the fiber to the point that the sphere reaches a point where the fiber is the desired thickness for the stem. If the sphere becomes larger than the desired diameter, the sphere can be exposed to the laser at very high power, which will cause some

of the silica to vaporize, shrinking the sphere diameter. At this point, the second fiber chuck is placed on the second x-y-z translation stage and is moved so that the two stems are in contact at their tips. This essentially resembles a sphere of the desired size in contact with a much smaller sphere. The CO<sub>2</sub> laser is then used to heat the spheres just to the point of melting while one of the the two z stages is used to gently push the two together until they form a single, asymmetric mass. The z-stage for the top fiber chuck is slowly raised until the bottom stem is completely removed from the bottom chuck and is hanging free.

The next step is crucial to forming a usable sphere, but is also extremely delicate. At this point in the process, the sphere is more of a blob and needs to be slowly and repeatedly heated in order to form a perfect sphere. If the annealing process were performed with the bottom taper as-is, there would be too much mass from the bottom stem hanging from the sphere, which would stretch the sphere along the axis of the stem as it is heated. This produces an elongated and asymmetrical DSS which cannot support the high Q equatorial WGMs necessary for the experiment. Similar problems occur if the hanging stem is too short. Because the CO<sub>2</sub> laser is heating the silica through optical absorption, this causes asymmetric heating of the sphere, i.e. the side facing the laser is heated more than the opposite side. If the bottom hanging stem is too light when annealing the sphere, it can lead to greater asymmetry as well as causing the bottom stem to bend towards the laser beam. In order to achieve the proper weight for the bottom stem, it needs to be cut just above the the point where the fiber jacket is still present. This is an extremely delicate process as the cutting process can cause unintended tension or shearing forces on the DSS, causing it to break. It took considerable trial and error to refine the technique for successfully cutting the

stem using the cutting edge of a fiber stripper. Using a Greenly Communication Fiver Optic stripper, the bottom stem should be suspended close to the vertex of the inner cutting edges as possible such that the transition from jacketed to un-jacketed fiber is hanging just below the cutting edges. Before cutting the fiber, the chuck holding the DSS should be held at a slight angle such that there is some slack on the fiber and a bend around the thinnest section where the sphere is located. This is necessary to prevent the stem from snapping under tension when the fiber is being cut. While the cutting edges are engaged with the fiber, small hand movements can cause an excess tension on the fiber, and it is also possible the act of cutting also inherently causes some tension as well. By maintaining a slight bend in the fiber with a small amount of slack, the DSS has more freedom to move/flex when it is cut rather than snap under tension.

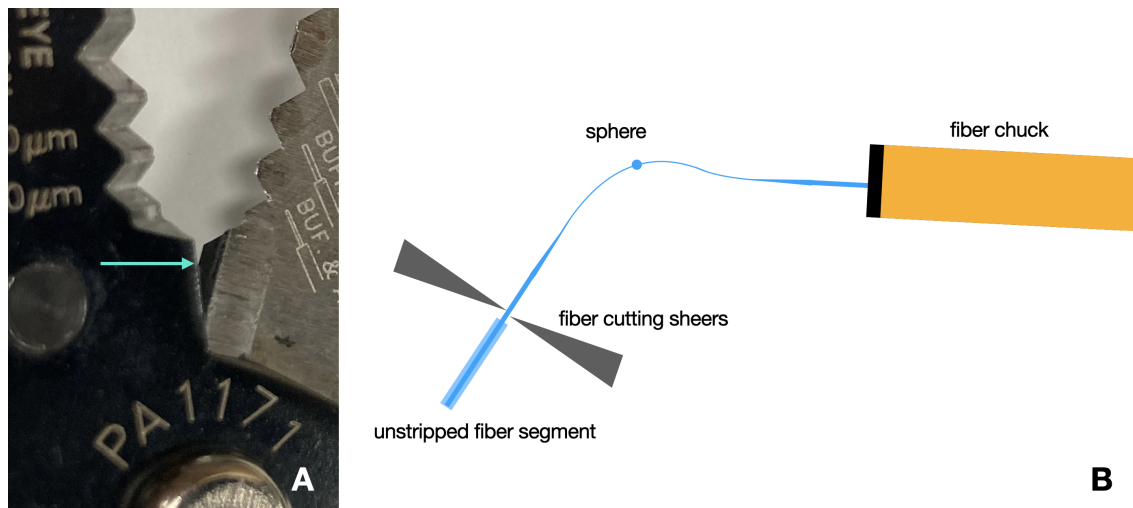


FIGURE 3.9. Trimming the excess fiber from the hanging stem of a double stemmed sphere. A) An arrow points to the specific point where the fiber needs to rest during cutting. B) An illustration showing roughly the necessary angles for holding the fiber strippers and fiber chuck to successfully cut the excess fiber without breaking the sphere. Note that in addition to the bend as the fiber transitions from the chuck alignment to the alignment of the hanging stem, there is a slight second segment of curvature on the fiber chuck end of the sphere which indicates there is slack on the the fiber.

Once the fiber has been clipped, the sphere is brought back into the beam path of the laser, and is heated until the two fused spheres appear as a one single (if asymmetric) sphere. If the right mass for the hanging fiber stem has been achieved, when the sphere is heated enough to reflow, it should not elongate, and it should appear to very slowly move upward along the top stem leaving behind a longer bottom stem as it moves up, maintaining its same stem diameter. This indicates that during the reflow process, the surface tension of the molten silica is significantly out-competing the downward pull of gravity on the bottom taper. This is in contrast to a bottom taper that is too heavy, in which case, the sphere will appear to stay stationary and will take on a more elliptical profile and possibly grow as material from the bottom stem is heated and becomes part of the sphere.

The sphere is then rotated about the chuck axis and repeatedly annealed with the CO<sub>2</sub> laser at moderate power for 1 second bursts at 8 different angles, each 45° apart. First, the sphere is annealed at 0° and 180°, 90° and 270°, 45° and 265°, 135° and 315°. This is necessary to achieve a sphere that is as rotationally symmetric as possible. Since the laser causes asymmetric heating, it can still cause some unwanted deformation of the sphere. Annealing the sphere from several angles helps compensate for heating induced asymmetry. Because the sphere is rotated about its stem axis during the annealing process, it is essential that care is made to ensure that the stem axis lines up with the fiber chuck/rotation stage axis. If it does not, this will lead to the two stem axes being misaligned, or even a sphere with enough asymmetry that it cannot support WGMs. Once the sphere has been repeatedly annealed at each angle multiple times, it is ready to be mounted on the DSS mounting assembly.



The fiber chuck and rotation stage are removed from the CO<sub>2</sub> laser setup and transferred to a x-y-z stage so that the top fiber is suspended parallel to the table. The DSS is then lowered down onto the mounting assembly so that each stem rests at the base of its respective v-groove. The x stage is then used to align the DSS so that the sphere rests at the midpoint the sample mount access recess. A small drop of UV epoxy (Norland Optical Adhesive 81) is applied to the v-groove above the tensioning attocube and then is cured under UV light for 10 seconds. This is not enough to completely cure the epoxy, but it is enough to allow for a hold that is plastic enough that the DSS can then be tightened to remove any slack without breaking the DSS. This step helps to ensure the stem axes are co-aligned. Once the slack is removed from the DSS, the epoxy is cured for one minute, and then a second drop is added to the other v-groove and cured for one minute. After this, a third drop of UV epoxy is typically added to the first v-groove at the very inside edge of the grove. This serves the purpose of minimizing the distance between the anchor points of the two stems to help maximize the resonance frequencies of the guitar string vibrational modes of the DSS to limit susceptibility to noise from the cryostat.

### **3.6. Fabricating Tapered Fiber Waveguides**

For fabricating tapered fiber waveguides for coupling to the sphere, we use an approach based on designs developed by Kippenberg [40], utilizing a hydrogen torch to heat a small section of fiber and a pair of servo motors that are used to continuously apply tension as the fiber stretches. The flame is created using a standard torch (typically used for acetylene/O<sub>2</sub> cutting) that is fed using an HGH-500E electrolysis hydrogen generator. A needle flow valve, along with a 90 degree

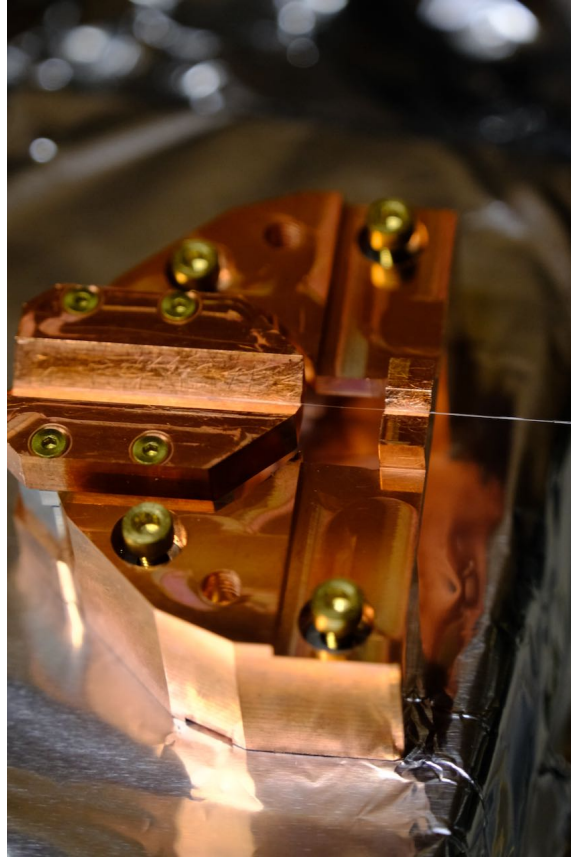


FIGURE 3.10. A double stemmed sphere in the process of being mounted and epoxied on to the sphere assembly. The both stems rest in their respective v-grooves and the sphere (not visible) rests at the center of the gap between the two grooves.

ball valve, are placed in-line with the torch to allow flow regulation and a quick method to immediately stop the flame when necessary. Hydrogen is preferred for taper fabrication because of its high burning temperature and completely clean combustion products. A hydrogen flame will only produce water vapor whereas organic fuels can sometimes leave behind incomplete combustion products that can contaminate the fiber surface.

The two translation stages used to clamp both ends of the taper are driven using a pair of computer controlled stepper motors. A custom fiber mount rests on both translation stages and uses fiber clamps to secure the taper over the hydrogen

flame. During the pulling process, both stepper motors rotate at the same rate, leading to symmetric pulling of the fiber. The computer control software allows for precise control of the pulling rates of the stepper motors, which is necessary to produce a fiber with usable transmission efficiencies. Lastly, a 20x objective mounted on a translation stage in tandem with a CCD are used to image the fiber at any point along the pulling region.

The taper process begins by stripping a 2-3cm section of SM600 single-mode fiber, and then cleaning using an organic solvent such as IPA or methanol. The segment of cleaned fiber is then secured in the two fiber clamps on the translation stage. About one meter of extra fiber on the non-spool end is left, and the end is coupled to an amplified photodiode. During the taper pulling process, constant frequency and power laser light is coupled into the fiber spool and the output is measured with the photodiode. This makes it possible to observe the power transmission of the taper in real time on an oscilloscope while the taper is being pulled.

When the torch is ignited, it is allowed to burn for about a minute before starting the pulling process to allow the flame to stabilize. The position of the fiber within the flame has a large impact on the length of fiber being heated and subsequently has a large effect on the pulling rates necessary to achieve an adiabatic fiber with an acceptable rate of transmission loss. The flame characteristics are extremely sensitive to air currents in the room as well as the hydrogen flow rate from the H<sub>2</sub> generator. The H<sub>2</sub> generator flow rate changes over time due to the constantly reducing volume of water in the electrolysis chamber, which often necessitates making several adjustments to the flame height and pulling rate to produce a good taper.

After the flame has stabilized, the servo motors are started at a speed of 30 mm/min. Once the heated section of fiber has been stretched by 30 mm, the rate of pulling is increased to 70 mm/min. Typically, the longer the fiber is stretched at slow speed before the pull rate is increased, the more adiabatic the fiber, yielding lower transmission loss. Transmission of 99 percent are achievable; however, the size constraints of the cryostat system limit the stretching distance to about 180 mm before the taper is susceptible to breaking during handling.

As the fiber is stretched and the core diameter of the fiber decreases, it departs from functioning as a single-mode fiber to allowing propagation of non-Gaussian spatial modes. Due to a constantly diminishing diameter of the fiber waist as the fiber shrinks, the relative phases of the various spatial modes will interfere, leading to an oscillation of the transmission amplitude, which can be observed on the oscilloscope. Eventually, the fiber core shrinks small enough that it can only support a single Gaussian mode again and the oscillation ceases. A few seconds after the transmission flatlines, the torch is put out and the stepper motors stopped. Observing the return to single mode transmission is useful as a benchmark for ensuring that the fiber is thin enough to allow effective coupling to the DSS. If the fiber core is too thick, the evanescent field of the waveguide mode will not be strong enough to allow an effective mode overlap with that of the DSS WGMs. Coupling can sometimes be achieved with a thicker fiber, but typically at the expense of greater cavity loss and difficulty maintaining taper-sphere coupling without the two contacting.

Once the taper is stretched, it is cut from the spool end about one meter from the taper point, and then lifted out using the removable taper clamp stage. After it is moved to a separate table, a micrometer on the taper stage is used

to adjust the taper tension to remove any slack and limit its susceptibility to vibration. The Invar mounting fork is held by a three axis positioner stage and brought into contact with the taper in the approximate position that it will be epoxied to the fork. Since the tapered fiber assembly in the cryostat only has an x and z stage, it is not possible to translate the taper horizontally (along the taper axis). Because the taper does not have uniform thickness it is essential that the narrowest part of the fiber be aligned with the midpoint of the fork to be usable. This is done by shining a bright white light at the taper. Near the fiber waist, the taper is thin enough such that it produces thin-film interference resulting in colored bands around the center, typically with one larger solid band surrounded by many thinner bands indicating the taper waist. Once the positioning stage has been used to align the taper center, two small drops of UV epoxy are applied to either end of the fork and cured, fixing the taper in place.

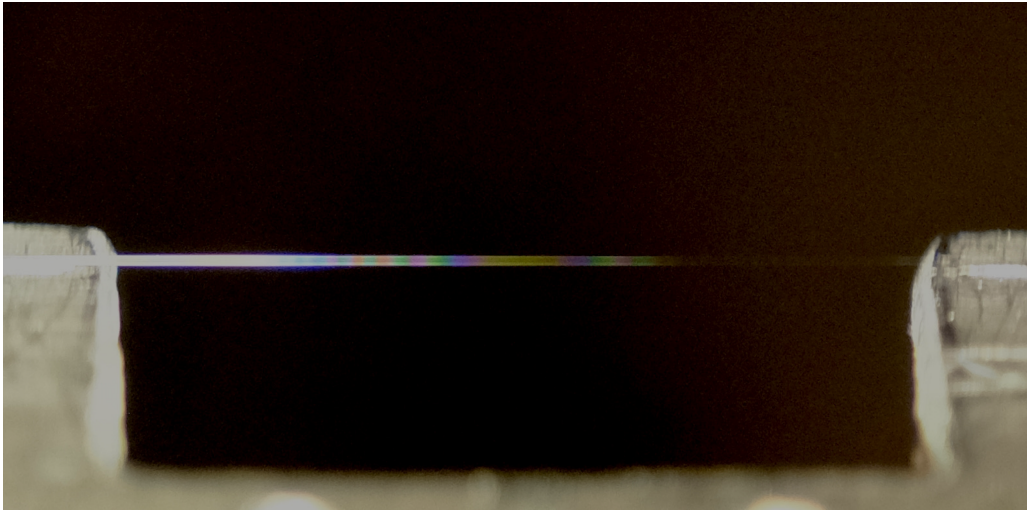


FIGURE 3.11. Color bands due to thin-film interference indicate the taper waist location during gluing of the fiber to the carrier fork. The center (wide yellow band) is surrounded by many other colored bands. The apparent thickness of the taper is an artifact from camera motion during the exposure.

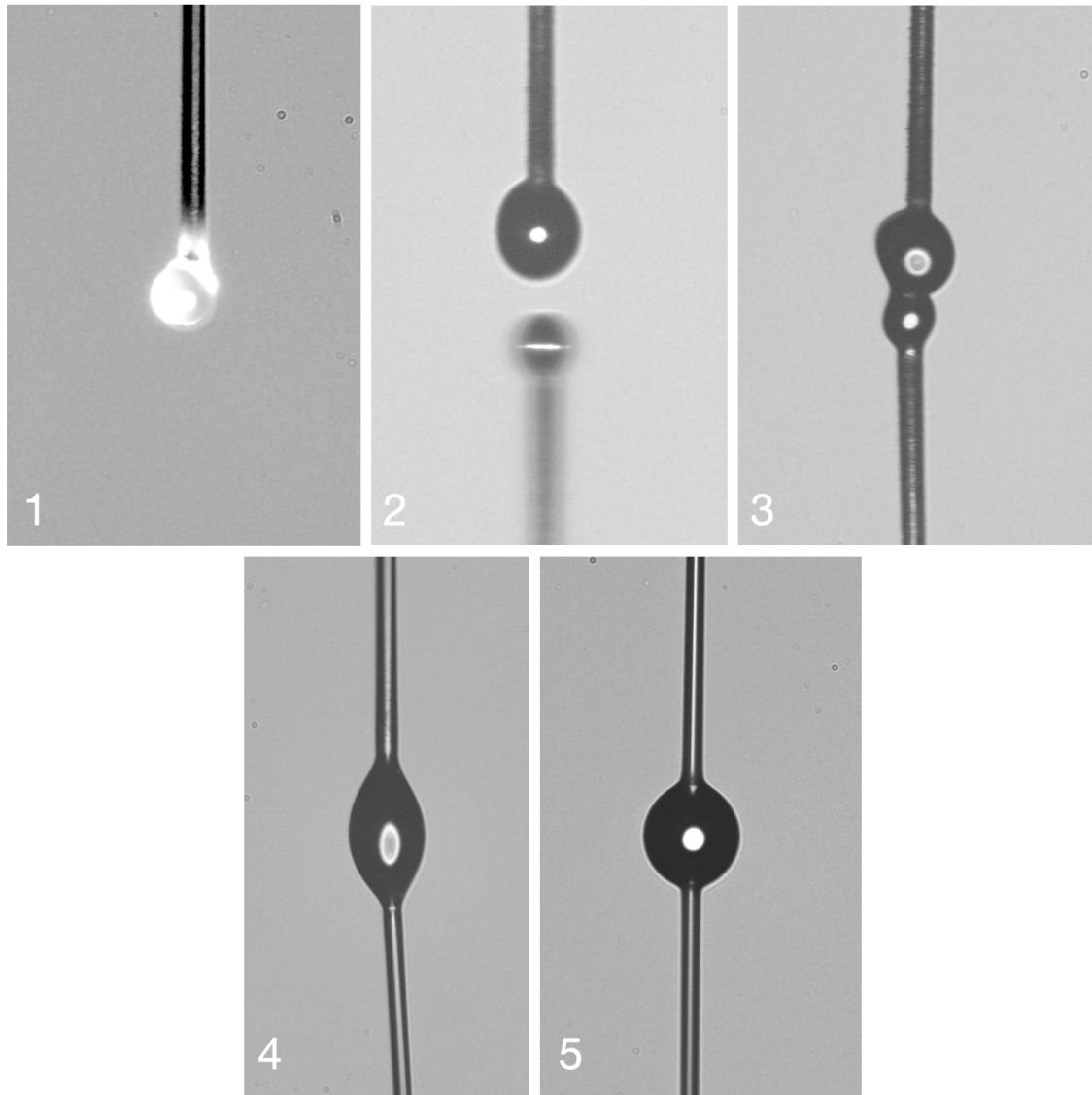


FIGURE 3.12. A series of photographs taken at successive steps of DSS fabrication. 1) A tapered fiber is cut with the laser and the tip is melted into a small droplet. The sphere can be seen glowing from the heat of the CO<sub>2</sub> laser. 2) The process is repeated for a second larger sphere and the first sphere is mounted on the translations stage below. 3) Both spheres are brought into contact and fused with low laser power. 4) Continued annealing of the fused spheres results in a single elongated almond shape. Also note that at this stage, the stems are not parallel to one another. 5) The hanging stem is trimmed and the sphere annealed repeatedly from multiple angles until it produces a nearly perfect sphere with co-aligned stems.

## CHAPTER IV

### SILICON VACANCY COLOR CENTERS IN DIAMOND: THEIR PROPERTIES, AND FABRICATION OF SIV IMPLANTED MEMBRANES

#### 4.1. An Introduction to Color Centers

Color centers in diamond are given their name precisely because they are responsible for the colors observed in diamond in some natural diamonds as well as lab grown diamonds that have been intentionally implanted with impurities to produce color. Perhaps the most well known diamond color center from its study in solid state physics, nitrogen vacancies (NVs) are responsible for the pink to red coloring sometimes seen in diamond. Color centers in diamond are a local defect in the covalent diamond lattice. Both nitrogen vacancies and silicon vacancies are di-vacancy type defects, where two adjacent carbon atoms are missing and either a nitrogen or silicon atom is situated in the vacancy left by the missing carbons. With the two missing carbons, the adjoining carbon atoms are no longer covalently bonded to one of their former nearest neighbors. As a result, the vacancy center contains several overlapping electron orbitals for the carbon nearest neighbors as well as those from the substituting non-carbon atom, and the interaction of these dangling orbitals results in an atomic-like system with its own energy levels and transitions governed by selection rules. In the case of NVs, the red color is due to its 637 nm optical transition, which is absorbing and then re-emitting resonant ambient light, hence the red hue associated with their presence in diamond.[10]

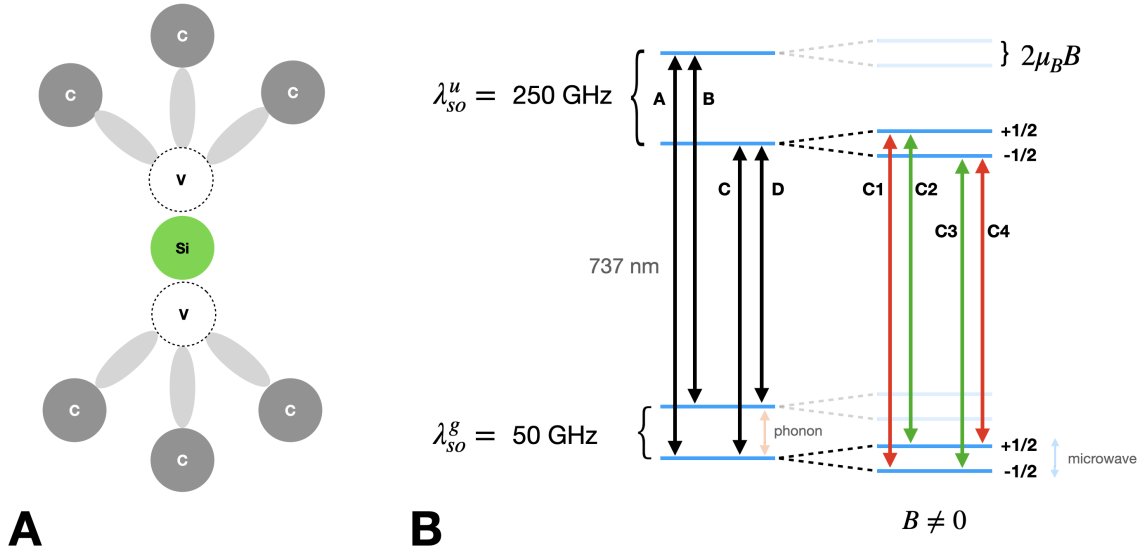


FIGURE 4.1. A) A 2D representation of the SiV geometry. B)  $\text{SiV}^-$  energy-level diagram for zero B field, and the case when an applied magnetic field lifts the spin state degeneracy. Green arrows indicate dipole-allowed transitions and red arrows indicate dipole-forbidden transitions. Dipole-forbidden transition may be allowed due to state mixing from the presence of an off-axis magnetic field. [43]

## 4.2. SiV Electronic Structure and Optical Properties

In its negative charge state, denoted  $\text{SiV}^-$ , the SiV color center has a fairly simple energy level structure compared to the negatively charged NV center. It features a degenerate ground state and a degenerate excited state with an optical transition wavelength of 737 nm. Both the ground state and excited state have these degeneracies lifted via spin-orbit coupling that results in both ground and excited states split into an upper and lower branch. Under zero strain in the diamond lattice, the ground and excited state splittings are 50 GHz and 250 GHz respectively. There are four distinct optical transitions corresponding to a transition from either excited state to either ground state. Local strain in the diamond can lead to variation of the excited and ground state splitting. The  $\text{SiV}^-$  is a spin-1/2 system, and consequentially, each of the four energy levels



are actually two degenerate level corresponding to either spin  $1/2$  or  $-1/2$ . This degeneracy can then be lifted through the application of a magnetic field resulting in Zeeman splitting. Optical dipole transitions are spin conserving, therefore only transitions between ground and excited states with the same spin state are allowed. However, this is only the case for a B-field aligned along the axis of the SiV and the application of a B-field off-axis will result in Zeeman splitting as well as state mixing, which allows spin non-conserving transitions.[43, 60] This is particularly important for the optical control of the SiV spin state, as selectively only utilizing for example the two transitions between the excited state lower branch spin  $+1/2$  energy level and both spin states of the lower branch ground state allows for optical processes involving a three level  $\Lambda$ -type system.

Transitions between spin  $-1/2$  and  $1/2$  states whose degeneracy has been lifted via Zeeman splitting can be driven by microwaves.[32, 60, 61, 62] The ground state splitting of 50 GHz is the primary source of spin decoherence in the system, as state mixing between the upper and lower branches of the ground state are driven by phononic coupling. While at higher temperatures, the spin decoherence times are fairly short; below about 700 mK  $k_bT$  is sufficiently low such that spin decoherence times greater than 10 ms are achievable. The SiV<sup>-</sup> also emits 70% of its florescence in the phonon side band compared to the 10% emission in the zero-phonon line (ZPL) of the NV<sup>-</sup>. The excited state lifetime for the SiV<sup>-</sup> of 1.7 ns gives a lifetime limited transition linewidth of 94 MHz, and observed SiV linewidths in bulk diamond tend to be within 200 to 400 MHz.[1] The SiV energy levels also couple to the local strain of the diamond lattice which impacts the spectral position of all four SiV optical transitions and consequentially, can be used as a method for controlled tuning of optical transitions.[32, 60, 61, 62]

A key physical distinction between the SiV and NV color centers that motivates the use of SiVs for this project is the position of the substitution atom within the di-vacancy defect. In the case of nitrogen vacancies, the nitrogen substitution sits at either of the two adjacent vacancy locations, exactly overlapping where the missing carbon atom would otherwise be. In the case of SiVs, the silicon atom is situated at the center of the defect, equidistant to both vacancy sites. The physical outcome of this slightly different arrangement and its value for this work comes down to symmetry. Unlike the NV, SiVs have inversion symmetry. Imagine that the silicon atom is the center of our transformations and the position of every atom is inverted through that center point. The result of that transformation would be indistinguishable from the original lattice. Because of this inversion symmetry, the SiV lacks any permanent electronic dipole moment. NVs on the other hand, being asymmetrical, result in a charge distribution that does have a permanent electric dipole moment. For the SiV, this means that it is comparatively robust to the effects of electric field noise in its local environment, making it much more stable.[2, 21, 25, 26, 27, 28]

The motivation for using SiVs in this system stems in part from the requirements imposed on the diamond membrane to limit Q-spoiling of the cavity while the two are in contact. To keep the diamond membrane from introducing excessive amounts of cavity loss, the membrane needs to be as thin as possible to limit dissipative coupling. For membranes that are approaching 100 nm in thickness, this means the actual distance from the surface to the SiV implantation depth may only be a few dozen nanometers. One constraint to fabricating nano-scale systems are the added impacts of surface effects on the local charge environment. The electric field noise produced by surface defects and mobile

surface charges is quite substantial compared to noise present in bulk diamond. For color centers close to the surface, the field noise can have a variety of negative impacts, including spectral broadening of optical transitions and spectral diffusion. For NVs, because of their permanent dipole, they are particularly sensitive to electric field noise making them generally unusable in applications where they need to be close to the diamond surface. When present in a diamond membrane less than 500 nm, even with processing to limit surface defects, NV transitions will consistently show linewidths of 500 MHz or larger. SiVs, on the other hand, are capable of being implanted near the surface while still maintaining relatively constant transition frequencies over time and able to achieve transition linewidths consistent with linewidths observed in bulk diamond.

Both SiVs and NV are produced artificially in similar ways. A particle accelerator is used to implant the respective ions into the diamond. This results in Silicon/Nitrogen atoms that are embedded in the lattice and also produces local points of damage in the lattice from the momentum of the embedded atoms as they collided with the carbon atoms. The kinetic energy of the silicon ions will also roughly determine the implantation depth where they are stopped. While the implantation process will result in silicon atoms within the diamond lattice, that implantation alone is not sufficient to produce SiVs. Since the SiV is a di-vacancy color center, the silicon atom needs to combine with a di-vacancy defect, which are not inherently formed at the location where the silicon atom ends up. The SiVs are finally formed by annealing the sample under high vacuum ( $10^{-6}$  torr) at high temps ranging from 400 to 1200 C, which allow vacancy defects to become mobile and combine with the stationary embedded silicon atoms forming SiVs.

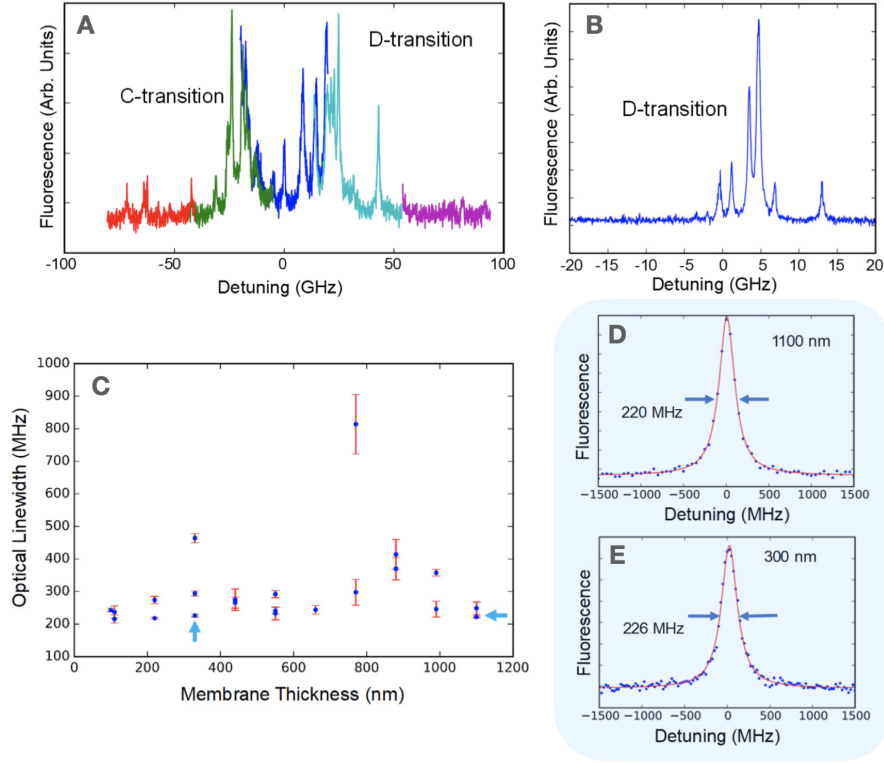


FIGURE 4.2. Confocal PLE of SiVs in the diamond membrane with no sphere present. A) PLE spectra of the SiV C and D transitions constructed from five individual narrow frequency laser scans. B) PLE of the D transition only. C) Scatter plot showing measured SiV transition linewidths as a function of membrane thickness demonstrating good optical coherence even when integrated in a nanophotonic device. D and E) Scans of individual SiV transitions corresponding to the two data points in C identified with blue arrows.

This annealing process also helps to repair other damage in the diamond lattice caused during the implantation process.

### 4.3. Fabricating SiV Implanted Nano-Membranes in Diamond

The diamond membranes for this work were fabricated by Ignas Lekavicius and Xinzhu Lee. Here I will provide a brief overview of the fabrication steps used to produce the membrane and the characterization of the resulting SiVs in the finished product. For a more detailed description of the fabrication process, please

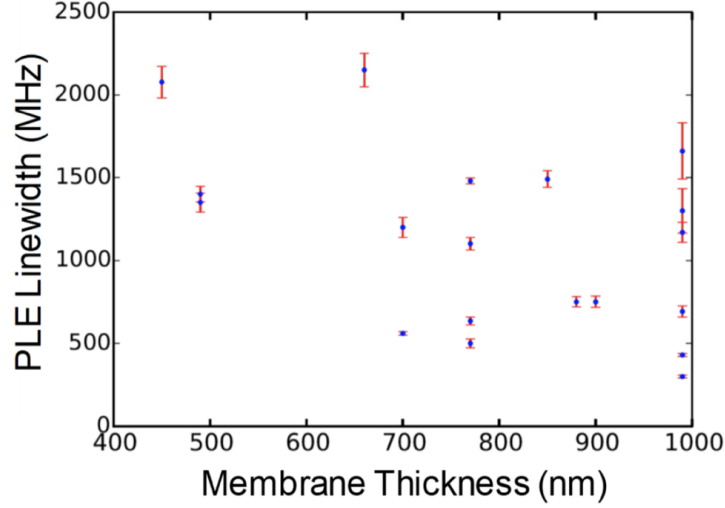


FIGURE 4.3. Scatter plot showing measured SV transition linewidths as a function of membrane thickness. In contrast to the SiV membrane samples, the NV linewidths are dramatically broadened. Membrane thicknesses of less than 600 nm result in linewidths greater than 1 GHz.

refer the paper on their design and characterization published in Optics Express [63]

The diamond membranes are fabricated from pre-cut monocrystalline diamond films that measure 2 mm by 4 mm with a thickness of 30  $\mu\text{m}$ . The process of slicing the larger diamond into these films results in some surface damage. The top 2 to 3  $\mu\text{m}$  of damaged diamond are then removed via an Argon/Chlorine inductively coupled plasma reactive ion etch. To remove any chlorine atoms potentially left behind on the surface, another few hundred nanometers of material are etched using an Oxygen plasma, before finally being cleaned using a tri-acid solution of 1:1:1 nitric, sulphuric, and perchloric acids to remove any residual contaminants.

After surface processing is completed, the sample is then implanted with Si<sup>+</sup> ions. In order to achieve the lower SiV density membranes needed to spectrally resolve individual SiV transitions in this experiment, an implantation

dosage of  $1 \times 10^{10}/\text{cm}^2$  was used. An implantation energy of 150 keV was used, which resulted in a mean stopping depth of 100 nm and a straggle (the range of implantation depths) of 20 nm. After implantation, the sample is annealed under vacuum to allow the formation of SiVs and repair unwanted implantation damage as described above. Following the annealing process, the sample is then cleaned again with the tri-acid solution to remove any layers of graphite that may have formed during the annealing process.

The fabrication of the membranes themselves was performed by depositing a 280 nm layer of silica nitride ( $\text{Si}_3\text{N}_4$ ) onto the top surface of the diamond film using plasma enhanced chemical vapor deposition. A thin layer of titanium is also deposited to facilitate SEM microscopy without surface charging. Lastly, a 500 nm layer of PMMA photo-resist is applied above the titanium and e-beam lithography is used to develop the PMMA layer according to the desired membrane pattern. Plasma etching with  $\text{CHF}_3$  is used to etch the PMMA and underlying silica nitride resulting in a silica nitride hard mask. The sample is then etched using  $\text{O}_2$  ICP to etch the pattern into the diamond itself. The sample is then flipped over and etched from underneath until the membrane cantilevers are released from the excess diamond.

To achieve the desired tapered thickness profile of the membranes, the sample is then flipped over and etched from underneath using a series of  $\text{Ar}/\text{Cl}_2$  and  $\text{O}_2$  plasma etches. This etch releases the excess diamond not indented to form membranes and also produces the tapered profile of the membranes with their thinnest segments being at their tips. Lastly,  $\text{O}_2$  soft plasma etching is used to remove the top layers of the membrane potentially damaged and embedded with ions from the plasma and reactive ion etching. PLE studies of the completed

membranes show that reasonable transition linewidths are maintained even after fabrication from the bulk material.

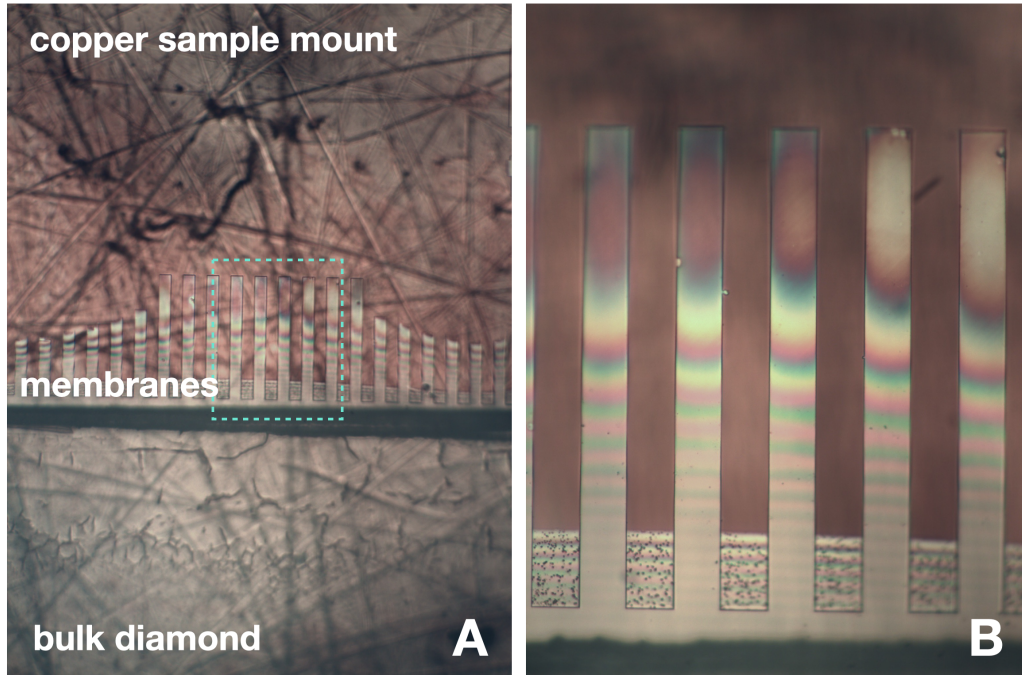


FIGURE 4.4. A) Optical microscope image of the low SiV density membrane mounted on the copper sample mount. B) An enlarged view of the blue box. Color bands indicating a tapered membrane thickness are visible.

## CHAPTER V

### SIVS AND CQED: APPLICATIONS IN THE GOOD CAVITY LIMIT USING THREE-LEVEL $\Lambda$ SYSTEMS

#### 5.1. Introduction

While the initial objective of this system is to observe cQED effects of single SiV optical transitions coupling to cavity modes, the real utility of this system for further study and application in quantum information emerges when using SiV energy level to form a three level or “ $\Lambda$ ” systems to enable quantum level control and interactions between the cavity field and SiV spin state via cavity mediated dark states/EIT.[64, 65] Similar control of SiVs, but with only classical field driving, has already been demonstrated.[22, 23, 24, 61] In this chapter, I will provide a brief overview of how an SiV would be used in a cavity mediated  $\Lambda$  system and briefly cover the different applications of that system for use in quantum computing and networking.

#### 5.2. A $\Lambda$ System for the SiV Spin State

In the case where a magnetic field is applied to an SiV, the degeneracy of the spin up and spin down states for each energy level is lifted.[24, 60] If the applied magnetic field has some component perpendicular to the SiV axis, this will also lead to state mixing, which will allow previously forbidden spin non-conserving optical transitions.[43, 60] The result of this splitting and state mixing is that now an optical system can be formed utilizing one excited-state energy level and two previously degenerate spin ground states with two optical transitions of slightly



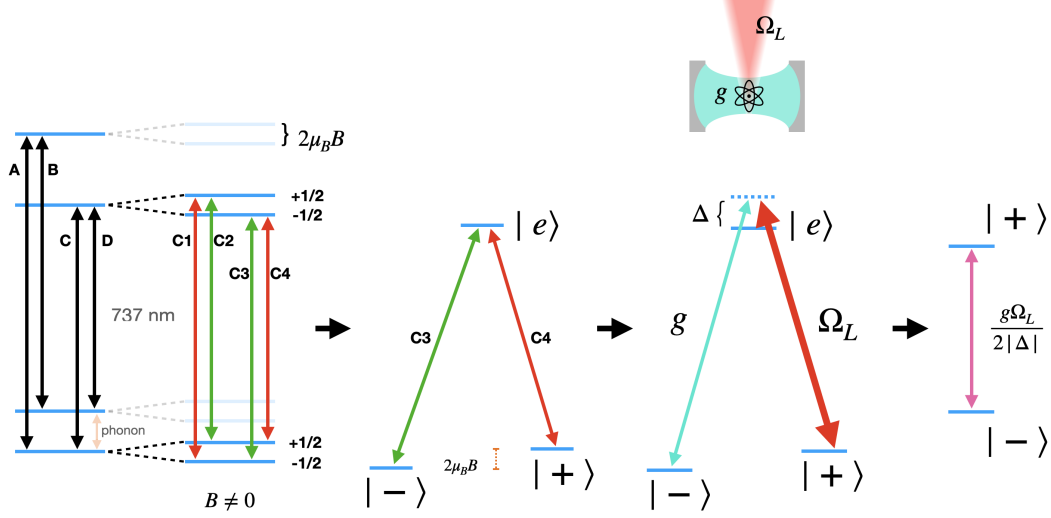


FIGURE 5.1. Three level  $\Lambda$  system of the SiV spin state using the cavity mode and classical driving field.[66, 67]

different frequencies. Provided the SiV is initially in one of these three states, both transitions can be driven by external fields to control the SiV state. In the case where the cavity couples to one transition while a classical driving field couples to the other, the interaction Hamiltonian is given by,

$$H_{int} = \hbar g \left( \hat{a}^\dagger |-\rangle \langle e| + \hat{a} |e\rangle \langle -| \right) + \frac{\hbar \Omega_L}{2} \left( \hat{a}^\dagger |+\rangle \langle e| + \hat{a} |e\rangle \langle +| \right) \quad (5.1)$$

where  $\hat{a}^\dagger$  and  $\hat{a}$  are the cavity mode creation and annihilation operators,  $|e\rangle$ ,  $|+\rangle$ , and  $|-\rangle$  are the excited state and two ground states of the SiV  $\Lambda$  system,  $g$  is the single-photon coupling rate, and  $\Omega_L$  is the Rabi frequency of the classical driving field. The states  $|+\rangle$  and  $|-\rangle$  correspond to the two different spin states of the SiV ( $1/2$  and  $-1/2$ ), but the assignment of spin states to  $|+\rangle$  and  $|-\rangle$  depend on the direction of Zeeman splitting governed by the magnetic field orientation.

The eigenvalues for this three level system are three nearly degenerate energies given by,

$$E_0 = \hbar\omega_c, E_{0,\pm} = \hbar\omega_c \pm \hbar \frac{\sqrt{4g^2 + \Omega_L^2}}{2}. \quad (5.2)$$

One of the eigenstates of this system, known as the dark state, is given by,

$$|D_0\rangle = \frac{2g |+, 0\rangle - \Omega_L |-, 1\rangle}{\sqrt{4g^2 + \Omega_L^2}} \quad (5.3)$$

where the integer in the ket denotes the number of photons in the cavity mode. Notably, the dark state is defined without the use of the excited state. This is the reason for it being given the name dark state; it is completely decoupled from the excited state of the  $\Lambda$  system. Consequentially, this means the dark state is also decoupled from the optical decoherence associated with spontaneous decay from the excited state to the two lower ground states. The coefficients for the two separate spin states are determined independently by  $g$  and  $\Omega_L$ . The presence of cQED dark states can be experimentally observed through the cavity transmission spectrum of the system. Figure 5.2 shows how the transmission peak of a cavity mode is perturbed when coupled to lambda system with zero Raman detuning ( $\Delta = 0$ ). Through the process of adiabatic following, it is possible to adjust these parameters at a suitably slow rate resulting in the evolution of the system into the desired superposition states of the SiV spin, which is determined by the final values of  $g$  and  $\Omega_L$ . Using this three level system would allow for optical control of the SiV spin state through control of the power of the classical optical field used to drive one transition, while the other transition is mediated on the level of single photons by coupling to the cavity mode.[69, 70, 71] If the classical driving field is adiabatically ramped from  $\Omega_L = 0$  to  $\Omega_L \gg g$ , the dark state will evolve from

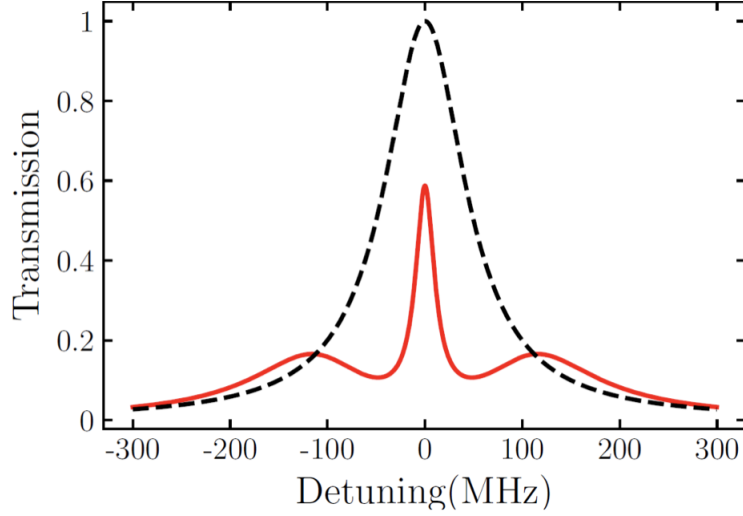


FIGURE 5.2. Calculated transmission spectrum (solid curve) of a cavity QED system containing a  $\Lambda$ -type 3-level system driven by a classical control field, with  $\Delta = 0$ ,  $\gamma/2\pi = 200$  MHz,  $\kappa/2\pi = g/2\pi = \Omega_L = 100$  MHz, and  $\gamma_s/2\pi = 4.5$  MHz. The dashed line shows the transmission spectrum of the empty cavity.[68]

$|+, 0\rangle$  to  $|-, 1\rangle$ . This process can similarly be reversed by instead ramping down  $\Omega_L$ , evolving the system from  $|-, 1\rangle$  to  $|+, 0\rangle$ . If, however, the system is in the state  $|-, 0\rangle$ , no change will occur from the evolution of  $\Omega_L$ . Through the use of a suitable pulse shape of the control field, this can be used to reversibly swap quantum information between the spin state and cavity mode:

$$\left(\alpha |+\rangle + \beta |-\rangle\right) \otimes |0\rangle \rightleftharpoons |-\rangle \otimes \left(\alpha |1\rangle + \beta |0\rangle\right). \quad (5.4)$$

This is useful for applications in a quantum network because it enables the transfer of quantum information between a stationary solid state spin qubit and an optical qubit which can then be coupled into an optical fiber and sent elsewhere.

This method of control and state swapping can be further extended through the use of multiple SiVs within the cavity to achieve cavity mediated state

swapping and entanglement between SiVs. For the case of two slightly detuned SiVs, it is possible to use the same cavity mode to perform state swapping between each SiV and the cavity via resonant Raman transitions without needing to tune the cavity field for each state swap. State swapping can be performed on the first SiV using a Raman detuned classical field and cavity field. This transfers the spin state of the SiV to the cavity mode. Successively performing a state-swap on the second SiV using a second Raman detuned classical field will result in the cavity state being swapped with the second SiV. Provided this procedure is completed on a time scale below  $1/\kappa$ , this will effectively result in a state transfer of the first SiV spin to the second. Being that for our system  $g > \kappa$  and  $C \approx 10$ , it will be possible to demonstrate such processes with the cavity-membrane system.

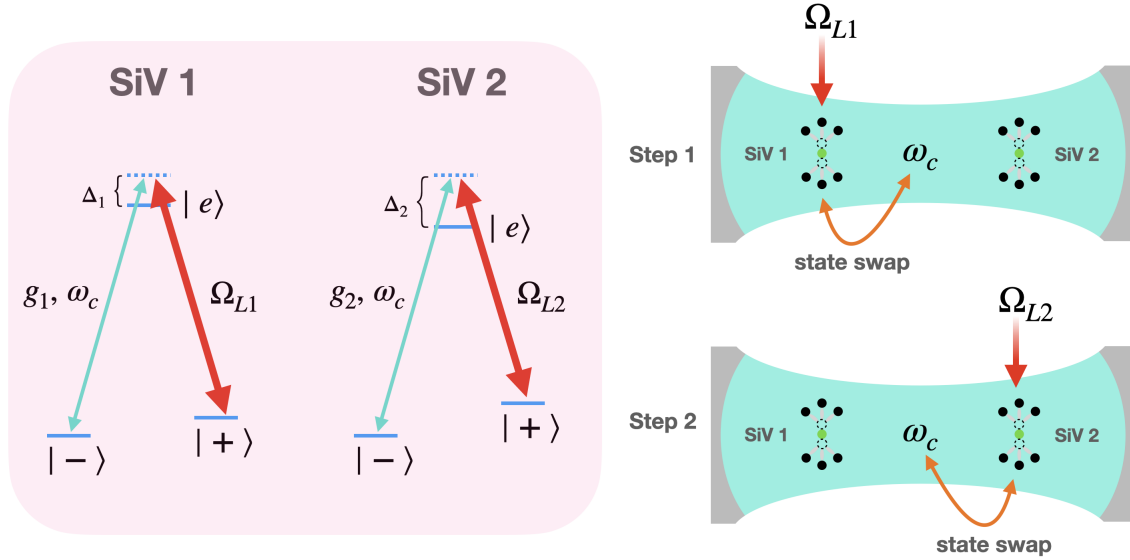


FIGURE 5.3. Cavity mediated spin state transfer between two SiVs within the same optical cavity.

A similar process can also be used to generate entanglement between two SiV spins in the cavity by instead applying a  $\pi/2$  pulse of the effective single-

photon coupling rate on the first SiV-cavity system, followed by a  $\pi$  pulse of the second SiV-cavity system, resulting in a maximally entangled spin state of the two SiVs.[29][72] This three level system can also be used to mediate interactions between SiVs within the same cavity utilizing through exchange of virtual cavity photons[67, 68, 73, 74], and has been demonstrated using SiVs however not utilizing the SiV spin state.[34] Cavity QED quantum control of SiV spins could be applied to quantum error correction, [69, 70, 75] used to create quantum cluster states for the development of quantum repeaters,[14, 76, 77, 78, 79, 80] as well as serve an interface between optical channels and scalable chip based platforms for quantum information. [81, 82]

## CHAPTER VI

### "THINKING ON YOUR FEET:" EXPERIMENTAL DESIGN, METHODS, AND CHALLENGES

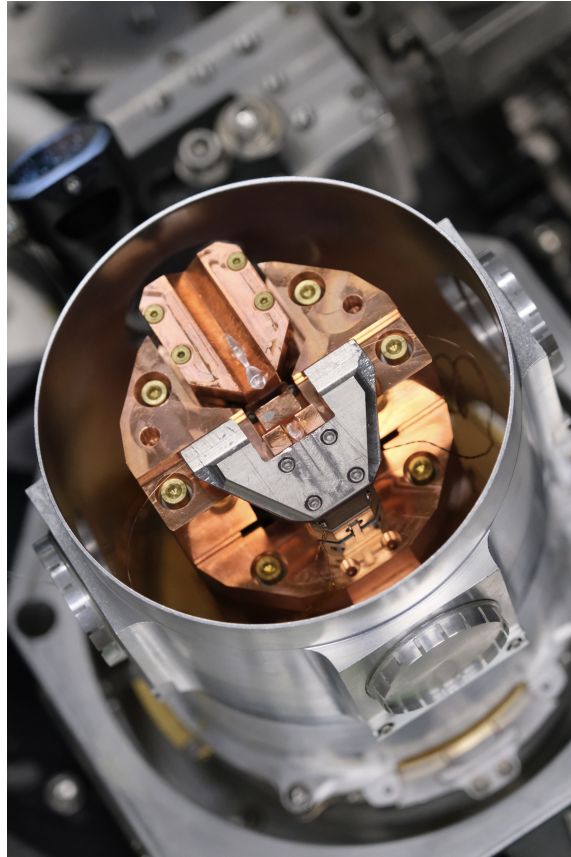


FIGURE 6.1. Top view of the last evolution of the cryostat system design, installed in the cryostat sample chamber with the radiation shield in place.

#### 6.1. Constraints and Objectives of the System Design

To a large extent, the system used to run the experiments for this project was developed from the ground up. While the optics setup outside of the cryostat vacuum chamber were largely based off of prior work done in the Wang Lab, the

task of designing an experimental system within the cryostat to control all the necessary degrees of freedom for coupling the taper-sphere-membrane system meant starting from a blank slate. A new experimental platform needed to be designed and fabricated based off of the constraints imposed by the cryostat and the conditions required to spectrally resolve single silicon vacancy centers and couple them to high-Q whispering gallery modes.

In addition to the challenges of designing a system that could properly position the sphere, taper, and membrane relative to one another, other major concerns were thermal conduction and cooling performance, vacuum quality, and sensitivity to noise and vibration. In this chapter, I will elaborate on the development and evolution of the cryostat system design. The larger experimental design and methods for preparing the system for experimentation, as well as the methods used for data collection, will also be discussed. Lastly, I will also discuss the major challenges encountered through multiple iterations of experimentation and optimizing the system design.

## **6.2. Cryostat System Design**

The basic function of the experimental setup contained in the cryostat is to allow the positioning of the diamond and taper relative to the sphere in order to achieve effective coupling and to allow strain tuning of the cavity resonances. The system is designed to do this while maintaining a sample temperature near 4K to achieve the necessary SiV transition linewidths. In addition to these basic criteria, the system also needs to minimize the effects of mechanical noise from the cryostat on the mode spectrum of the cavity.

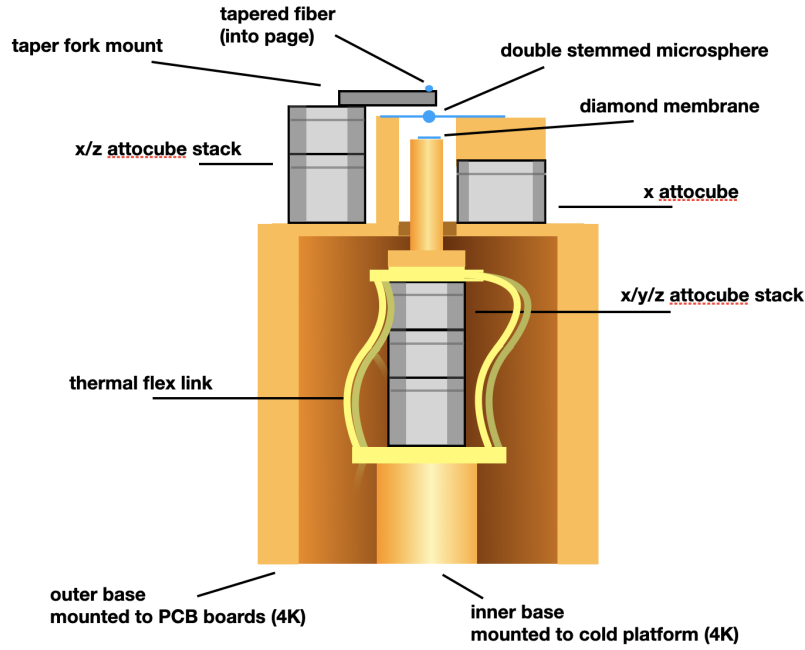


FIGURE 6.2. A cross section sketch of the cryostat setup.

The system design consists of three separate systems that serve the purposes of mounting and positioning the diamond, sphere, and taper. There are two separate mounting pedestals, a central pedestal that rests on the cryostat cold platform, and an outer platform that rests on the 4K PCB boards that encircles the cold platform. The center pedestal is used exclusively for mounting the sample positioning assembly, and the outer pedestal is used for mounting the taper and sphere assemblies. The center pedestal is used for the sample assembly because it is essential that the diamond receives the optimum cooling power possible.

While the system does cool down the PCB boards to 4K as well, the PCB boards are not highly conductive, and further, the PCB boards are connected to the cold platform via an aluminum mounting bracket, which also has very poor thermal conductivity at cryogenic temperatures. While the outer pedestal



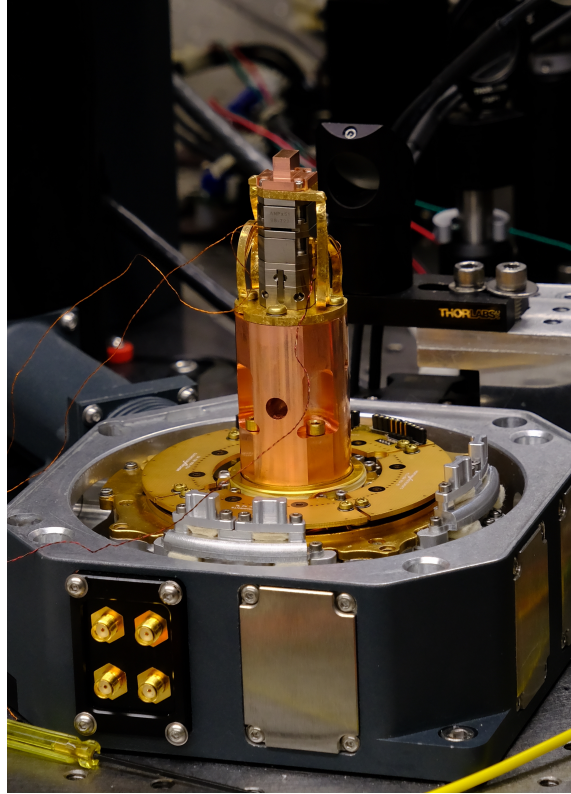


FIGURE 6.3. Cryostat sample chamber with central pedestal, attocube nanopositioners with flex link, and sample mount installed on the 4K cold platform. The 4K PCB boards (gold) are visible surrounding the pedestal.

temperature has not been measured when the system is operating at target temperature, it is likely it does not reach the target temperature, whereas there is only a 0.2 K  $\Delta T$  from the cold platform to the sample mount. Because the outer pedestal is still contained within the cryostat radiation shield, which is held at 30K, it is likely that the temperature of the assembly mounted on the outer pedestal is somewhere between 30K to 4K when the cryostat has reached its target temperature. This might at first seem like a problem, if the sample needs to be kept at 4K while the sphere it is in contact with is significantly warmer. Fortunately, at cryogenic temperatures, the thermal conductivity of silica is

extremely poor and well below that of diamond, so minimal heat of the sphere occurs due to conduction from the outer pedestal.

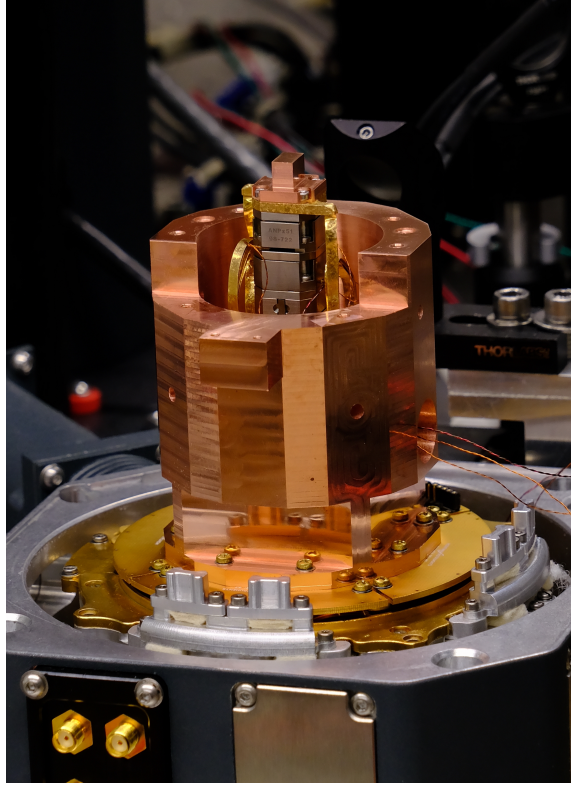


FIGURE 6.4. Outer pedestal mounted on the 4K PCB boards.

When the sphere is brought into contact with the diamond, it cools down rapidly and reaches a steady state temperature in a matter of several seconds. This can be seen from observing the cavity mode spectrum when the diamond is brought into contact with the diamond, as the changing temperature shifts the cavity resonances due to the thermal dependence of silica's index of refraction. As will be discussed later, PLE scans of the SiV transitions indicate that the contact of the sphere to the diamond does not present a significant heat load and the sample is able to maintain a continuous temperature low enough to reach suitably narrow SiV transition linewidths. An advantage of using a fairly massive piece of

copper as the outer pedestal is that it also acts as a thermal battery and prevents rapid temperature changes when the cryostat is stopped for short periods of time, potentially allowing alignment or brief experimentation with limited mechanical noise from the cryostat while still operating in the required temperature range.

The sample assembly consists a stack of three attocube nanopositioners (one ANP/z/51/LT and two ANP/x/51/LT) and a small platform mount to which the diamond is fixed using silver thermal paste. The nanopositioners are not effective thermal conductors, especially at cryogenic temperatures, so the top and bottom of the attocube stack is thermally bridged using a Montana Instruments flex link adapter, which allows for the normal range of motion of the positions while still maintaining a good thermal connection to the sample.

The taper mount assembly consists of a base plate that fits on the outer pedestal and an x/z attocube stack for positioning the taper. The fiber itself is epoxied on either end to a mounting fork that is secured on the top x attocube. The fiber fork has to be made out of Invar 36, which is a stainless steel alloy engineered to minimize thermal expansion/contraction from large changes in temperature. Once the sphere has been epoxied to the fork, it is important that the thermal contraction/expansion match that of the silica fiber as much as possible. If the fork contracts significantly more than the taper, the taper will become extremely loose and makes it impossible to achieve effective coupling of the taper to the sphere. If the taper contracts significantly compared to the fork, it will eventually snap during cool down. Ideally the fork would be made out of the same material as the taper: fused silica. This option was considered; however, there were a few design challenges associated with that option and the Invar fork worked well enough, so it was not made a priority.

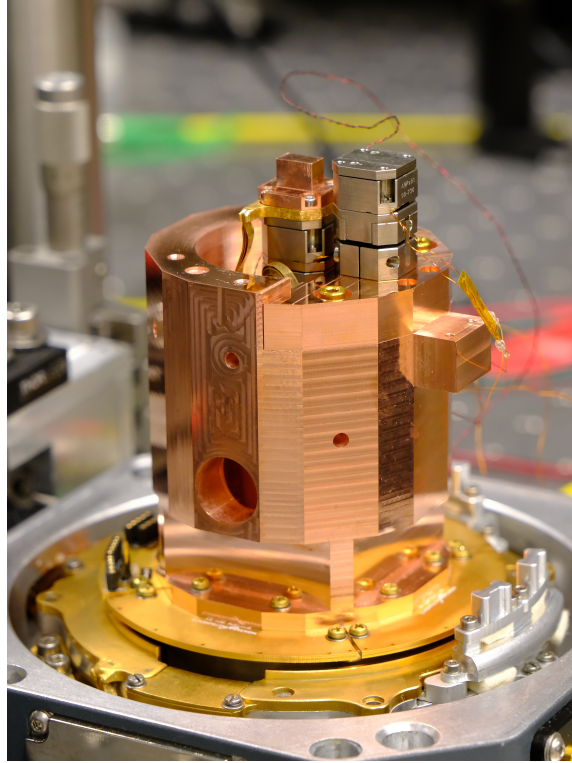


FIGURE 6.5. Taper assembly (missing the Invar fork) mounted on the outside pedestal

The sphere mounting assembly consists of a monolithic copper plate, an ANP/x/101/LT nano positioner, and a v-groove mounting plate that secures to the top of the attocube. There is a second v-groove on the monolithic mounting plate that is aligned with the attocube v groove, which are separated by a hole in the monolithic plate to allow the diamond sample mount to protrude up and contact the sphere. The v-grooves are used for aligning the DSS during the epoxy process to 1) insure that both stem axes are properly co-aligned and 2) to guarantee that the stem axis will be parallel to the plane of the diamond membrane sample. If the stem's axes are not co-aligned, as more and more tension is applied, the DSS will straighten out, but as it does so, the sphere will move as the DSS straightens out under tension. This is undesirable, as motion of the sphere

while it is coupled to the diamond and tapered fiber will also impact coupling rates or potentially even break the membrane coupled to the sphere. Secondly, the DSS axis needs to be parallel with the plane of the diamond membrane to allow coupling without the stem contacting the sample or sample mount. For a  $70\text{ }\mu\text{m}$  DSS with a stem diameter of  $20\text{ }\mu\text{m}$ , which is reflective of those used for this experiment, if the angle of the stem axis relative to the membrane exceeds  $1.25^\circ$ , the stem will contact the sample mount before the sphere can contact the membrane, making coupling between the two impossible. In order to keep the stem axis angle small enough to allow the system to function properly, the two v-grooves cannot be offset in height by more than  $180\text{ }\mu\text{m}$ , the width of a human hair, which is indicative of the machining tolerances required while fabricating these components.

### **6.3. Optics Setup and Data Acquisition**

Optically, the experimental setup outside of the cryostat consists of free space and fiber optics used to perform PL and PLE experiments and image the system, as well as an optical fiber system used to couple to the cavity and to collect the fluorescence from the system. The free space aspect of the experiment follows a typical design used for confocal microscopy. There are two lasers used, a  $532\text{ nm}$  diode pumped solid state laser used for charge state initialization and photoluminescence spectroscopy, and a tunable ( $730\text{-}739\text{ nm}$ ) New Focus diode laser, which is used for resonant SiV excitation and observing the cavity transmission spectrum. For both red and green optical paths, acoustic optical modulators are used as optical gates for pulse sequencing as well as power attenuation of the lasers. The  $737\text{ nm}$  beam is then coupled into a single-mode

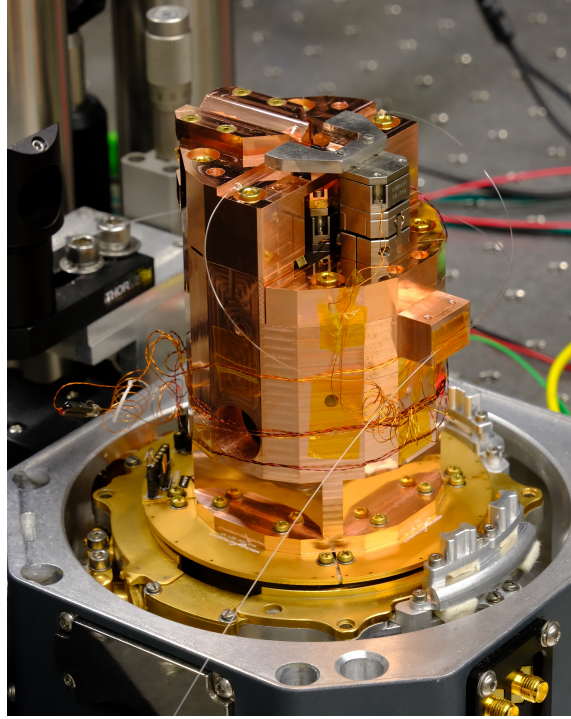


FIGURE 6.6. Cryostat setup with the top sphere mounting assembly installed and fiber fork mounted to the fiber positioning attocubes. Note that the fork pictured is from the first design iteration and the improved design used for experimental runs with the low SiV density sample is pictured in the first figure of this chapter.

fiber. When the system is being used for PLE experiments, the output of the single mode fiber is launched via a collimator and then merged with the 532 optical path via a dichroic beam splitter which transmits the 737 nm beam but reflects the 532 nm. The shared red/green beam path is then launched vertically from the bench into an x-y galvo mirror system mounted on a platform above the cryostat sample chamber. The beam from the galvo goes directly to the 20x objective, which is focused onto the diamond, passing through the sphere before it reaches the membrane. In addition to the green and red paths, two beam splitters just before the light is launched into the galvo mirrors are used to illuminate the sample with white light and to image the reflection via a CCD and monitor.





FIGURE 6.7. Closeup of the cryostat system (without tapered fiber). The DSS is visible suspended across the two v-grooves. The diamond membrane is seen mounted to the copper pedestal with silver paste.

One way the optical system differs from a typical confocal microscopy setup used for PLE is that while the objective can be used to optically excite the SiVs, it cannot be used for efficient free space collection of the fluorescence due to the presence of the microsphere in the beam path. The geometry of the system is such that the excitation beam must pass through and be focused by the sphere before it is incident to the diamond membrane. As a consequence, it would be incredibly difficult to achieve the necessary alignment of the free space collection path.

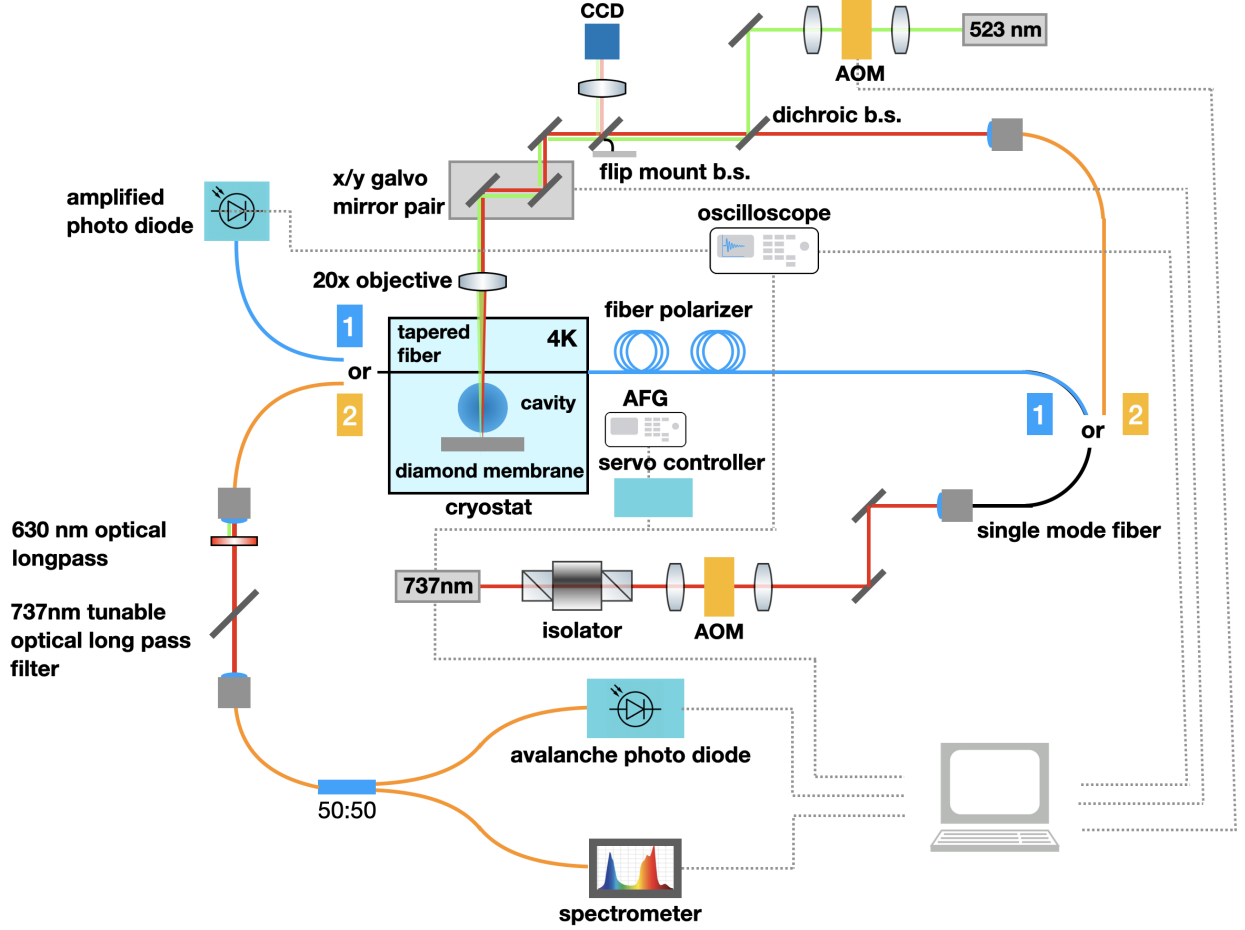


FIGURE 6.8. Schematic of optical and data acquisition setup.

Instead, the SiV fluoresce is collected via the cavity. When the sphere is in contact with the membrane, some of the fluorescence of the SiVs couples into the cavity, which can then be collected via the tapered fiber coupled to it. One of the fiber outputs from the cryostat is sent to a collimator to launch the fiber and then coupled back into a multimode fiber, which can then be sent to either the avalanche photodiode detector (APD) or spectrometer. The short space in which the collection path propagates through free space allows for the use of several long-pass filters to attenuate the unwanted 532 nm light which also couples into the collection path. When the system is used to run PLE experiments, a tunable



long pass filter is inserted as well to block the 737 nm laser while allowing the fluorescence of the SiV in the phonon side band to pass.

While at first glance, it would seem simpler to use the fiber input to the cavity for the excitation path, it is not, in fact, a suitable option. While it would greatly simplify the need for optical alignments, the optical driving field experienced by the SiV would vary wildly at different excitation wavelengths due to the response of the cavity resonances. For the purposes of having a uniform 737 nm optical driving power across the range of frequencies being scanned for PLE spectroscopy, free space excitation is necessary.

When the system is used to observe the cavity transmission spectrum, the 737 nm light is not re-launched into free space but connected to one of the fiber feed-through outputs from the cryostat, and the other output from the cryostat is sent to an amplified photo diode for detection. The fiber optical path of the 737 nm input also contains a fiber polarization controller which is used to adjust the laser polarization to selectively excite either the TE or TM family of WGMs.

The cavity transmission spectrum is measured through the use of a 2 V peak-to-peak ramp wave signal input to the 737 nm New Focus laser frequency control input. The frequency control input modulates the voltage applied to a piezoelectric crystal that controls the diffraction grating responsible for tuning the laser cavity. Adjusting the input voltage will slightly adjust the grating angle, leading to change in the frequency of the laser output. One volt applied to the piezo corresponds to a 10 GHz frequency shift from the laser's usual set point, with a maximum tuning range of  $\pm 30$  GHz. An arbitrary function generator (AFG) is used to generate the ramp wave with a frequency of 80 Hz. The AFG output is then sent to a New Focus laser controller unit which allows for manual fine tuned adjustments

of the ramp wave amplitude and offset, the output of which is then sent to the frequency control input on the New Focus laser. An amplified photodiode is used to detect the transmission via the other fiber optic output from the cryostat. The output signal from the photodiode, as well as the frequency sweep from the laser controller, are observed via an oscilloscope. The resulting waveform collected is the cavity transmission power as a function of time, and because of the linear ramp wave used to modulate the laser frequency, the horizontal axis of the scope can be mapped to the laser frequency, and thus the cavity transmission spectrum measured.

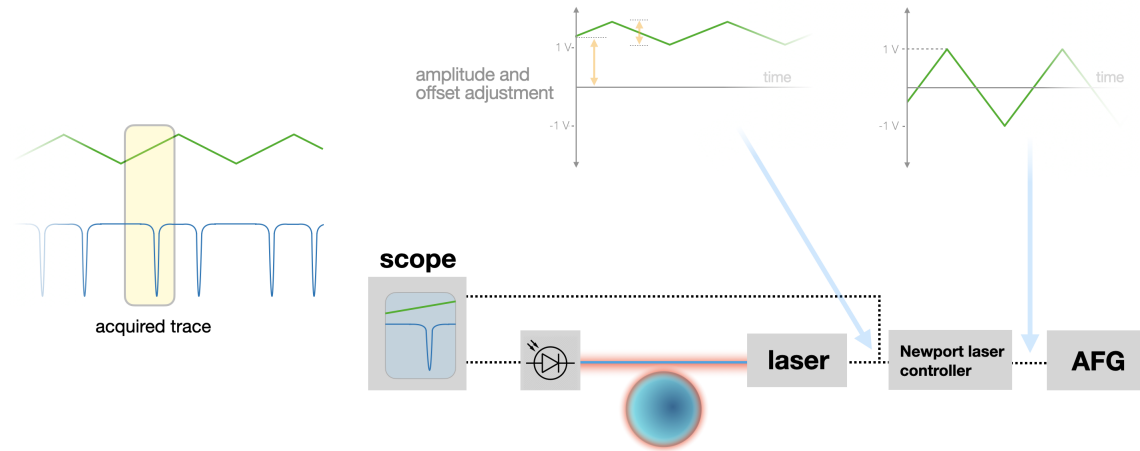


FIGURE 6.9. Illustration of the method used to measure the cavity transmission spectrum.

#### 6.4. Configuring the Cryostat System

The first step in preparing the system for experimentation is to bring the taper into contact with the sphere. The taper needs to be aligned with the sphere's equator. This can be roughly accomplished by scanning the fiber along the DSS axis while the fiber is in contact with the sphere. The evanescent cavity loss is visible through the CCD as light being emitted tangentially from one edge

of the sphere. The pattern of light essentially makes the spatial distribution of the WGMs visible, and the taper is positioned such that light is primarily emitted from the equator. This alignment method is typically effective enough for PL and PLE experiments, but to be more precise, after that alignment method has been completed, the taper is stepped away from the DSS and then coupled to the sphere without touching. Fine adjustments can then be made with the piezo offset mode of the x nano-positioner to find the fiber position that optimizes the coupling rate to the equatorial modes while minimizing coupling to lower  $m$  value modes. Once the alignment is complete, the fiber is stepped down into contact with the sphere.

After the taper is configured properly, the diamond is raised until it is roughly 100 microns below the sphere. The CCD image is used to pick the specific membrane to use for experimentation and the sample is positioned to bring the chosen membrane underneath the sphere. The diamond is then slowly raised step by step. Quickly scanning the diamond position up risks damaging the diamond, as well as the sphere and taper, if it continues to move after the diamond has made contact with the sphere. Contact of the diamond to the sphere can be confirmed by monitoring the sudden change in the cavity transmission spectrum as well as visually through the CCD image. When the diamond contacts the sphere, concentric newton rings appear at the contact point. It is important to confirm that the center of the newton rings has a dark spot, and that the dark spot does not appear to “blink” when the cryostat is running. This indicates that the membrane does not have continuous contact with the sphere and needs to be raised slightly to maintain constant pressure at the contact point. To find the optimum coupling point on the membrane that produces the least q-spoiling, the membrane should be moved and the q-spoiling checked at multiple points about

the membrane. While doing so, it is extremely important to drop the sample down away from the sphere while translating the membrane in the x/y plane to limit the accumulation of contamination on the sphere. It is also necessary to avoid bringing the sphere in contact with the edges of the membrane which can scratch the sphere. In general, the membranes are surprisingly resistant to breaking under the typical conditions of contact forces with the sphere; however, at the edge, small pieces of the membrane can break off and become stuck to the sphere.

Since occasionally the taper or membrane can move away from the sphere during long experimental runs, it is useful to have a method to confirm contact without needing to adjust alignment optics to view the system through the CCD, which would require realignment. The membrane can be tested by observing the count rate with the APD for CW 532 nm while stepping the attocube down several steps. If the membrane is in contact with the sphere and then releases, there will no longer be an object to cause significant scatter of 532 nm light into the cavity and the APD counts will drop significantly. If the counts instead increase significantly when the membrane is removed, this indicates that considerable contamination has accumulated on the sphere and it needs to be replaced. A similar method can be used with the taper as well.

## **6.5. Cavity Transmission Spectrum Measurement**

To observe the cavity transmission spectrum, CW 737 nm is sent through the tapered fiber and the output from the fiber is measured using an amplified photo diode. Typically, the optical power is not allowed to exceed 100  $\mu$ W. This is important both for preserving the taper as well as preventing thermal drift of the resonances due to optical absorption induced heating. Particularly when the

system is under vacuum and cold, the thermal cooling of the taper is very poor. As a consequence, if high power 737 nm light is used, any contaminant or defect on the taper that will absorb the 737 nm light will heat up rapidly and quickly burn out the taper.

An 80 Hz 3 V peak-to-peak ramp wave is generated from an AFG, which is then sent to a New Focus servo controller, which allows for fine tuned adjustments to the ramp wave amplitude and offset. The output of the servo controller is then sent to the frequency control channel of the 737 nm laser which modulates the optical frequency by adjusting the laser cavity just slightly through a piezoelectric crystal that controls the cavity diffraction grating. The laser is calibrated such that a 1 volt input signal corresponds to a 10 GHz frequency shift of the laser from its normal set point. The output from the amplified photo diode is then measured via an oscilloscope. The continuous ramp of the laser frequency input signal results in a constant sweep of the laser frequency through a set range, which allows the cavity transmission spectrum to be seen in real time through the oscilloscope.

## **6.6. Optical Alignment and Spectroscopy Experiments**

The first step in PL/PLE experiments after the membrane, sphere, and taper are all properly coupled is to use the galvo mirror to find the point where the cavity contacts the membrane, the point where the SiVs will couple to the WGMs. Using the manual micrometers on the galvo/objective stage, the laser spot is coarsely positioned at the center point of the sphere and focused onto the back side of the sphere. The 532 laser is then scanned over an area around the center of the sphere while the output of the taper is measured with the APD to generate a two dimension raster image of the APD signal. Ideally, the long pass filters in the

collection path would block out all of the 532 nm excitation light and the detected photons would be only from the SiV PL. However, even with multiple long pass filters, the green vastly outshines the red PL, so the resulting image is a map of green scatter into the cavity and not the SiV fluorescence. On a clean sphere, the image will typically show a silhouette around the edge of the sphere, and near the center, the contact point is visible as two spots of scatter separated by a dark section of minimal scatter. The dark spot is the contact point.

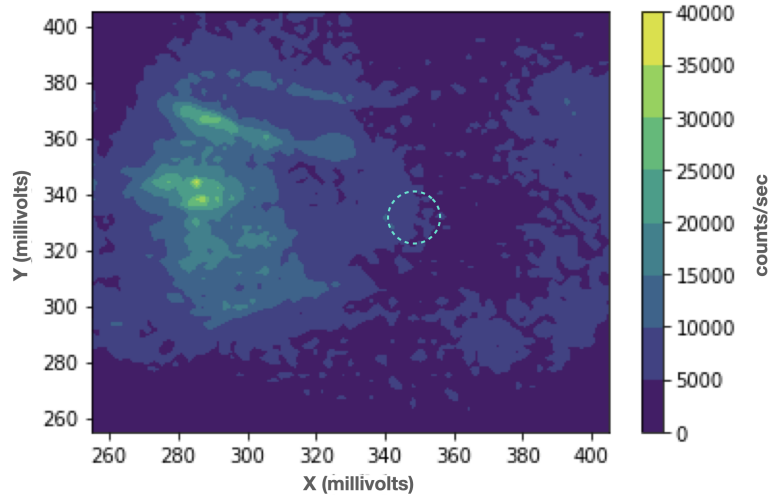


FIGURE 6.10. 532 nm scan raster image of the sphere-membrane system. The silhouette of the sphere can be seen, and the point of high intensity at the left edge of the sphere is due to free space coupling of the 532 nm light into the sphere. The blue dotted circle denotes the approximate contact point.

To confirm the location of the contact point and optimize the beam alignment for fluorescence experiments the collection output is switched from the APD to the spectrometer. Systematically sampling points at and around the center by running 3 min integrations on the spectrometer with the 532 nm CW at maximum power, the location can be confirmed by finding the point of maximum PL amplitude from the SiVs. PL is the preferred method for optimizing the laser spot because all of the fluorescence coupled into the fiber is collected, whereas for

PLE experiments, it is necessary to block the zero phonon-line which accounts for 90% of the SiV's emission, requiring significantly longer integration times. The image produced by detection of green scatter into the cavity can vary from sphere to sphere. For this reason, it is recommended to optimize using the PL method for a few days until you are familiar with the pattern and can skip straight to PLE experiments.

For PLE experiments, a tunable long pass filter is needed in the collection path to block the driving 737 nm laser. The alignment process is delicate and care needs to be taken as to avoid over saturating and damaging the APD detector. The filter is placed in the collection beam path so that it is initially normal to the incident beam. The APD counts are monitored with CW 737 nm focused at the contact point while the filter angle is slowly adjusted. When the filter is normal to the collection path, there is still a red leak rate of a few hundred counts per second when using max red power. The filter should be adjusted to let in no more than three times that leak rate into the detector. Because only 10 percent of the fluorescence from SiVs comes from the phonon side band, the filter cutoff should be tuned as close to the ZPL as possible without collecting too much of the driving laser. If the filter is tuned past about three times the red leak lower limit, the light from laser scatter into WGMs will become significant, and in addition to the desired SiV spectroscopy data, the PLE scan will also show peaks from the cavity mode structure. For anything other than low optical power high resolution scans, it is extremely difficult to do background subtraction to identify the actual SiV transition peaks from the unwanted WGMs in the scan.

## 6.7. Challenges of Working in the Cryostat Environment

Our Montana Instruments closed cycle cryostat simplifies this experiment in some ways but also poses challenges that had to be overcome. The main advantage of the cryostat is that it can be cooled down with the press of a button and can essentially maintain the target temperature for months at a time. A helium flow cryostat, on the other hand, requires a large dewar of liquid helium and can only maintain the target temperature as long as there is still liquid helium remaining. The drawbacks of the system for this experiment are its noise/vibrational isolation and its vacuum performance. The narrow linewidths of silica microspheres make them an ideal cavity for a cQED system, but their high Q modes also means they are very susceptible to noise and contamination in the system.

## 6.8. Vacuum Performance

When the Fusion is at its target temperature, it can maintain vacuum pressures of approximately  $10^{-8}$  torr. The system achieves this pressure by utilizing charcoal absorbers that act as cryopumps when the system is cold. At cryogenic temperatures, gas molecules that collide with the charcoal stick to its surface. The only difference between the charcoal absorbers and every other component in the cryostat at cryogenic temperatures is the porous nature of the charcoal provides a very large surface area for gas molecules to stick to. Every other cold component in the sample chamber also cryo-pumps to some degree, and that includes the microsphere as well. This can pose a problem when enough nitrogen has deposited onto the surface of the sphere leading to scattering loss and a significant degradation of the cavity linewidths.



Whereas most high and ultra high vacuum systems utilize copper ConFlat flanges to provide seals, the Fusion utilizes rubber o-rings which have a significantly higher inherent leak rate even when properly installed. While the system can reach pressures of  $10^{-8}$  torr inside the sample space, the constant low level leakage of atmosphere into the system means that nitrogen deposition will always occur and eventually degrade the sphere. Unlike other causes of sphere degradation like scratches and surface contamination from microscopic particulates, q-spoiling from nitrogen deposition is reversible. Stopping the cryostat and heating the sample platform to 100 K causes the frozen nitrogen to sublime off of all heated components. Running an external turbo vacuum pump during the heating process removes the gas which has accumulated in the system and then the cryostat can be started again. Depending on the quality of the o-ring seals, the system can go weeks between low temp burn off cycles.

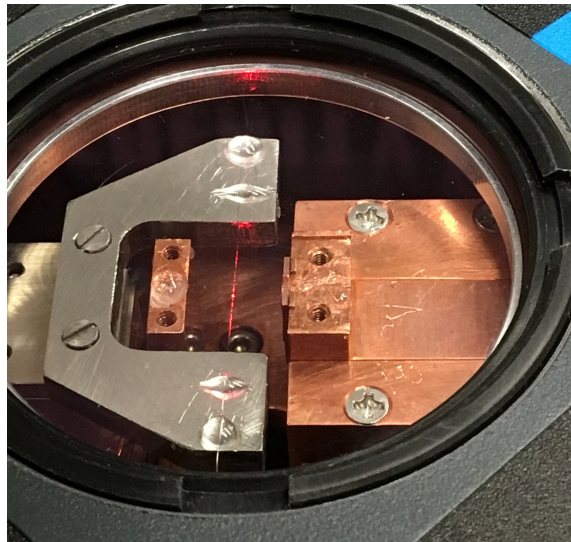


FIGURE 6.11. An extreme case of nitrogen ice deposition during an initial test run without the top radiation shield lid installed. Sub-micron sized spots of nitrogen ice deposition cause scattering of nearly 100 percent of the light propagating in the fiber into free space, causing it to glow red from the scattered laser light.

This process was used extensively to maintain the microsphere linewidths; however, after one particular burn off cycle, I forgot to valve off and shut off the external turbo pump before restarting the cryostat. The external turbo pump used was backed by a “wet” roughing pump that uses a silicone lubricant. When oil pumps run, they tend to create tiny microscopic droplets of oil. Normally, when a turbo pump runs, those droplets do not make it past the turbo pump due to the pressure gradient from the pump. When the pump was left running and open to the vacuum chamber after the cryostat was restarted, the charcoal cooled back down to 30 K and began to cryopump again. The turbo being used could only pump down to around  $10^{-5}$  torr, while the charcoal absorbers pump down to  $10^{-8}$ . Having both pumps run at the same time created a pressure gradient opposite of the nominal direction for the turbo to function properly. That reverse pressure gradient caused the oil droplets created by the roughing pump to drift into the sample chamber and cryopump onto all of the components at cryogenic temperatures. This led to such a high buildup of oil in the sample chamber that the diamond was completely coated in oil and the optical modes of the cavity were effectively destroyed.

This oil leak was a significant setback as it took well over a month to sufficiently clean the system. Any oil left in the system could still potentially cause further contamination to the diamond during the process of warming the cryostat up to room temperature. If a contaminated surface on the first stage of the cryostat reaches higher temperatures while the sample platform is still at cryogenic temperatures, it could cause the deposited oil droplets to be cryopumped back onto the sphere and diamond again.

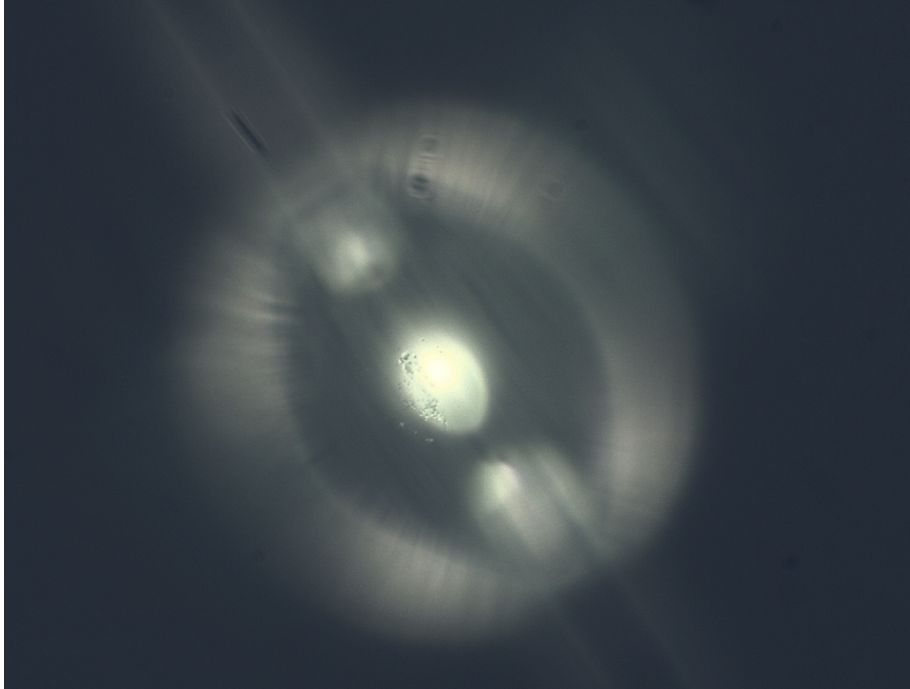


FIGURE 6.12. Micrograph of the sphere after the oil leak into the sample chamber. Significant oil accumulation is visible where the sphere was in contact with the membrane.

It took several iterations of washing/wiping components with acetone and IPA and performing a system bake-out until the vacuum chamber was clean enough to proceed. After all the experimental components were reinstalled, including a new sphere and taper, the system was cooled down to run the experiment. After a few days, the cavity linewidths degraded to the point that it was worth running a low temp burn off cycle. I was much more conservative with how I utilized the turbo for that burn-off. I let the system rise to 150 K and only ran the turbo for roughly 15 minutes before valving it off and restarting the cryostat. Unfortunately, even with the extra precautions, it was still apparent that there was increased q-spoiling due to oil contamination.

In hindsight, oil contamination has probably always occurred during these burn off cycles, but was misattributed to other sources of cavity loss. Generally,

over time, spheres tend to degrade to the point that they need to be replaced. I attributed this to accumulation of dust contamination and scratches from the sphere coming in contact with a diamond membrane that is not perfectly clean. While that probably still contributes to q spoiling, a burn off cycle could still incrementally degrade a sphere even if it appears to be improving the linewidths after every burn off. A burn off cycle might lead to a temporary significant reduction in the line width, but the slow accumulation of oil droplets would increase the irreversible scattering loss each time. This issue has likely been a root cause of gradual q-spoiling over time, and it was only identified because of one particularly acute instance of oil contamination.

## **6.9. Noise and Vibrational Performance**

The cooling mechanism for the Fusion closed cycle cryostat is a two stage cold head which uses pistons to adiabatically expand compressed helium gas. While the cryostat is running, these pistons cycle, typically at around 1 Hz. This action of the pistons creates a significant source of noise in the system through vibration and sound conduction into the cold platform. For most applications, the Fusion's sample chamber has been engineered to be well isolated from vibrations from the cryostat, with platform peak-to-peak vibration amplitudes on the order of 5 nm. While this is exceptionally small, a DSS coupled to a tapered fiber is extremely sensitive to noise. The two parameters of the sphere-taper system that are extremely sensitive to noise are the length of the sphere-taper coupling gap and the strain tuning of the cavity resonances.

For the sphere-taper-gap, noise can come from both guitar string vibrational modes in the sphere as well as the taper. For the range of sphere sizes used in

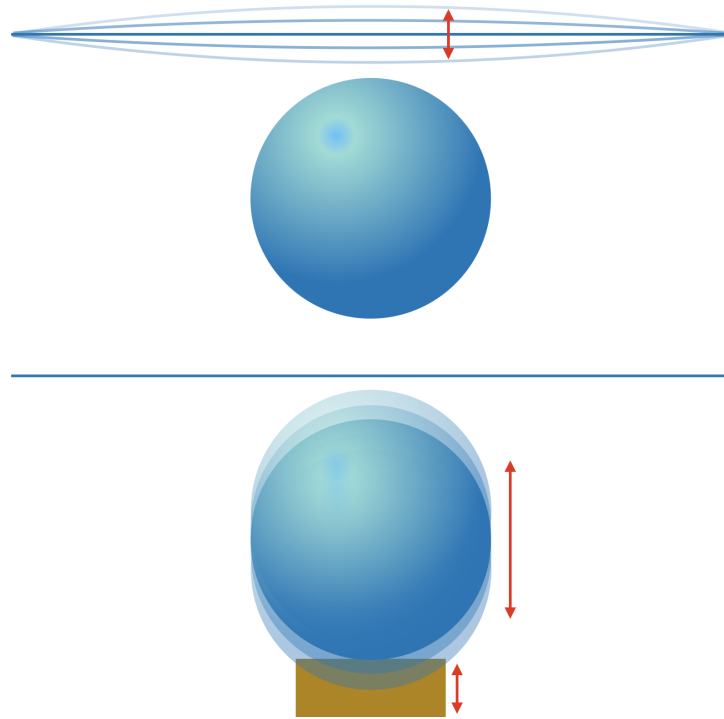


FIGURE 6.13. Illustration depicting cases of vibrational modes of the sphere-taper system inducing coupling noise. In the top example, the sphere is stationary while the taper experiences guitar string vibrational modes. The bottom case depicts vibration of the sphere either due to guitar string modes of the DSS stems, or vibration through contact with a vibrating sample mount.

this experiment, the decay length of the cavity's evanescent field is usually several hundred nanometers. As discussed previously, that decay length also characterizes the dependence of the taper-cavity coupling rate on the separation between the two. A 5 nm peak-to-peak oscillation in a taper-sphere gap of several hundred nanometers would cause minimal noise in the cavity transmission spectrum.

However, the stated spec for vibrational performance of the cold platform is not the same as the vibrational stability of the sphere or taper. Since both can act as mechanical resonators with guitar string-like modes, the 5 nm peak-to-peak oscillation at the base of the system leads to resonant driving of these modes leading to an appreciable source of noise in the transmission signal. Uncorrected,

this noise can make it impossible to accurately observe features like cavity linewidths. Stopping the cryostat can temporarily solve this issue; however, as the platform warms, the system will experience thermal drift, which can effect the relative positions of the membrane-sphere-taper system, and will also lead to a steady drift of the cavity resonances due to the thermal dependence of the sphere's index of refraction. Warming the system will also lead to broadening of the SiV optical transitions.

Apart from system design considerations to limit noise, which will be discussed in the next section, one method for reducing the susceptibility to vibration is maintaining adequate tension on the sphere and the taper. Increasing the tension on the sphere and taper raises the resonant frequency of their fundamental vibrational modes so that there is less effective driving of the mode by the lower frequency noise/impulse of the cryostat piston.

A second way for vibrations/sound to generate noise in the WGM spectrum of the cavity comes through vibration driven frequency modulation of the cavity resonances. Maintaining a stable cavity resonance frequency requires that the sphere have a static tension applied to it, i.e. that both anchor points where the stems are glued remain fixed relative to one another. If vibration/sound conduction through the system causes any vibrations at the anchor points of the double stemmed sphere, that will result in a rapid oscillation of the WGM resonance frequencies. In the case of the first system design for this experiment, one of the anchor points for the stems was on a pedestal-like post (20mm x 10mm x 3mm). A downside to this design was that this post would essentially behave as a cantilever-like tuning fork. Each time the piston in the cryostat would cycle, it would cause an impulse that would ring the pedestal. When the sphere was

under tension, this would result in an oscillation of the resonance about the set frequency by as much as tens of gigahertz. Considering the fact that the cavity linewidths of the WGMs being observed are typically on the order of 50 MHz or less, and that the mechanical oscillation frequency of the pedestal was on the order of 10 kHz, it was essentially impossible to accurately observe the linewidths of the WGMs while the cryostat was running. The frequency sweep of the laser to scan the cavity mode spectrum generally should not cycle faster than 100 Hz, and as a result, the cavity resonance would oscillate about the set point hundreds of times during a given sweep of the laser frequency. At best, this oscillation would cause the mode to appear artificially broadened, and at worst, it was impossible to observe anything that could be considered a peak.

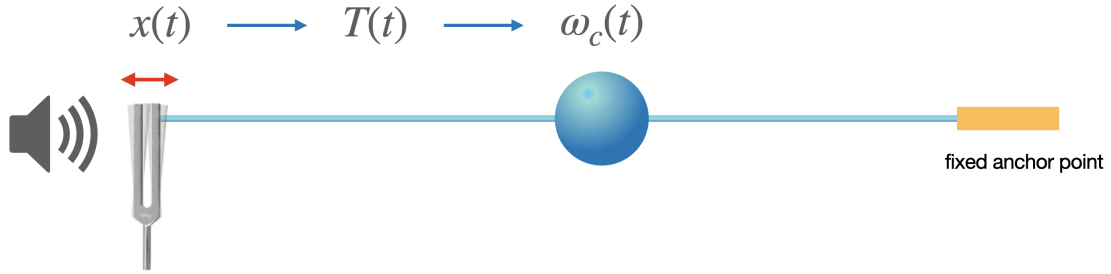


FIGURE 6.14. A simplified illustration of the process responsible for vibration and acoustically induced cavity frequency noise. Sound and/or vibration from the cryostat excites resonant vibration of one of the anchor points of the double stemmed sphere. The resulting vibration at the anchor point results in high frequency variation of the stem tension leading to rapid modulation of the cavity mode resonance frequency.

To give an anecdotal example of the system’s sensitivity to sound conduction, when the system is running and the taper is coupled to the DSS and the cavity mode spectrum is being observed in real time, the sound of someone sitting next to the cryostat talking can be enough to significantly disturb the transmission background. By humming a scale next to the vacuum chamber, you can find the

pitch of the taper or sphere resonance frequencies, and by humming or singing at slightly higher volume, drive the vibration enough to cause the taper to stick to the sphere. In the past, sources of noise as small as a heat sink fan on a laser, or the vibrations of a powered but not running stepper motor on the far end of the optics bench 15 feet away, was sufficient to make collecting usable data impossible.

Another major flaw with the initial system design was the mount for the diamond membrane sample. The original configuration had the sample sitting on top of an approximately 30 mm pedestal that was secured onto an x-y-z attocube stack. This also acted as a cantilever that could vibrate, but this was further exacerbated by the fact that the three attocubes it rested on were much less rigid compared to monolithic copper and can act as very rigid springs. This resulted in vibrations of the diamond sample on the order of several microns when the cryostat was running, and when the diamond was brought into contact with the sphere while the cryostat was running, it was impossible to effectively observe the cavity mode spectrum or even maintain taper-fiber coupling without the taper sticking to the sphere.

## **6.10. Redesigning the Cryostat System to Limit the Impact of Vibration**

When it was determined that the first iteration of the experimental setup inside the cryostat was too susceptible to vibration to be useable in the desired experiments, a revised system design was made to limit the susceptibility to noise from the cryostat. Most of the major changes to the system design were made to the top plate that is used to mount the taper and sphere. The new mounting plate design was monolithic, fabricated as one single piece as opposed to the old design



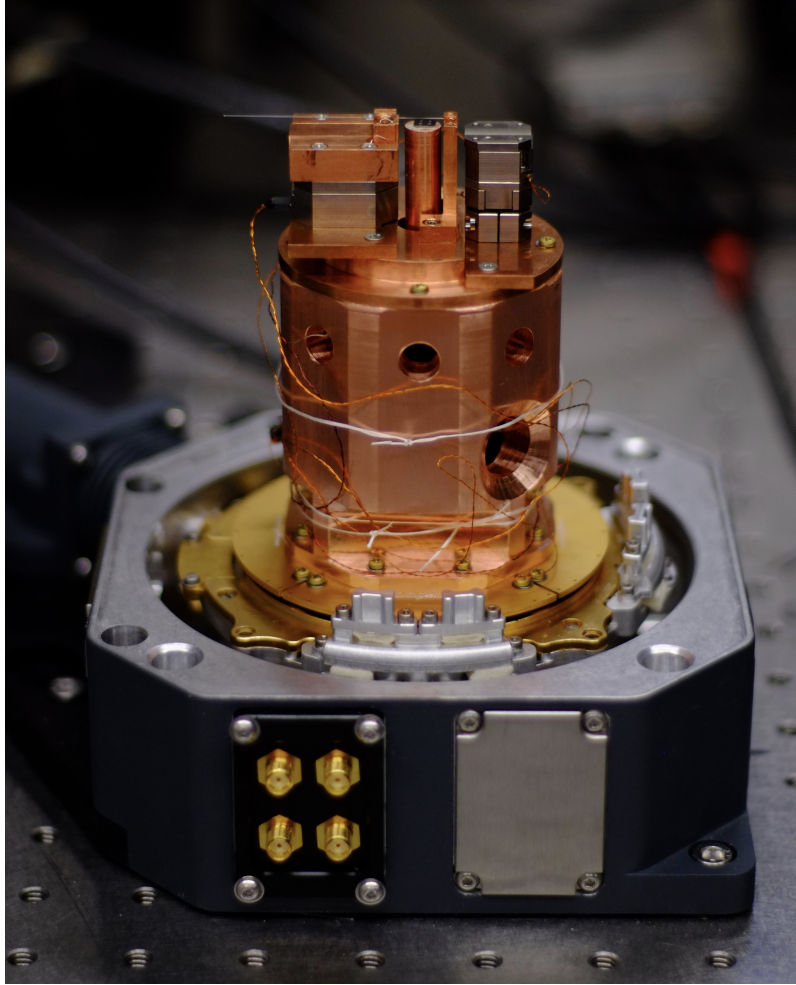


FIGURE 6.15. The original cryostat system design. Note the relatively tall and thin sample mount and taper anchor point which posed major issues for vibration and acoustic sensitivity.

which consisted of four separate pieces secured with screws. The new design also increased the thickness and mass of the sphere mounting plate to limit structures that would be prone to vibrating. Lastly, the new design eliminated the presence of long pedestal-like components used to mount the sphere and sample which were extremely sensitive to vibration.

The impact of this redesign was dramatic and reduced the effect of the cryostat noise to the point that it is possible to effectively observe the cavity

transmission spectrum and make measurements of cavity linewidths while the cryostat is running. Further reduction of vibration and sound conduction into the experiment would be ideal for obtaining very precise cavity linewidth measurements; however, most further steps to limit vibrational effects entail modifications to the cryostat itself, which was beyond the scope of what was achievable in the time necessary to complete this project.

## CHAPTER VII

### CHARACTERIZATION OF THE TUNABLE CAVITY QED SYSTEM

#### 7.1. Introduction

In this chapter, I will cover data collected on the performance of the tunable microsphere cavity. Cavity transmission measurements are used to verify minimal Q-spoiling of equatorial WGMs upon contact with the membrane, as well as verify the range of cavity mode tuning achievable using the strain tuning method. Lastly, I will also characterize the noise present in the cavity transmission spectrum resulting from acoustic and vibrational conduction into the cryostat sample chamber due to the operation of the cryostat's compressor and cold head.

#### 7.2. WGM Q-Spoiling

The key condition this system needs to achieve cQED coupling in the good cavity limit is the preservation of narrow linewidth equatorial cavity modes even when in contact with the sphere. Figure 7.1 shows the mode spectrum of a single equatorial cavity mode before contact and while in contact with the diamond membrane. Note the minimal broadening of only 3 MHz. The extent of Q-spoiling is particularly dependant on the choice of contact point on the membrane and it can at times be tricky to achieve such a result. The optimum location on the membrane for minimizing the Q-spoiling is generally near the thinnest point of the membrane where the color interference fringes are not present, and roughly equidistant from either edge of the membrane. The high degree of sensitivity to location suggests there might be additional unexpected behavior in the interaction

of the cavity mode with the membrane which impacts the coupling behavior. This could also have implications for the field strength of the WGM at the SiV depth. The minimal Q-spoiling induced by the membrane indicates that cavity linewidths can be preserved while integrated into the taper-sphere-membrane composite system.

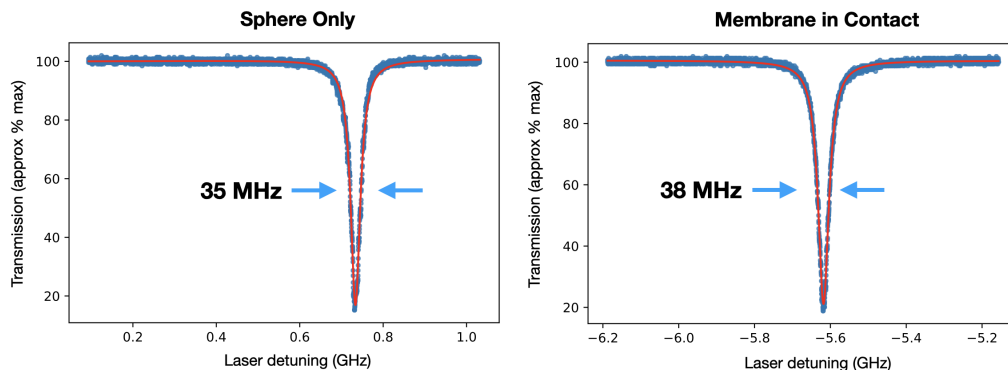


FIGURE 7.1. Cavity transmission spectra of an equatorial WGM with the sphere alone, and the case when the diamond membrane is in contact with the sphere.

### 7.3. Tension mediated cavity tuning

Given the fact that the DSS fabrication process results in an unpredictable mode spectrum, the need to achieve a zero SiV-cavity detuning for cQED experiments necessitates a working tuning cavity tuning range somewhat comparable to the free spectral length of the cavity. Figure 7.4 shows data collected from a test of the tuning performance of the system at room temperature. Using the step positioning mode of the nanopositiner, a frequency shift of nearly 200 GHz was achieved with just over 250 steps. In this case, data collection was limited by researcher fatigue, not any limits of the system itself. Even after data collection was concluded, it was possible to continue stretching the

sphere for several hundred steps before the attocube was seen to hit its stick-slip limit and fail to apply further tension.

Even though the data were collected at room temperature, the only practical difference between this data and the capabilities of the attocube at lower temperatures is finer resolution. When the attocube is cooled down to cryogenic temperatures, a 30 V step input will produce a considerably smaller displacement of the stage that using the same step size at room temperature. The result is simply that the step count required to shift a WGM a fixed amount is increased when cold. The non-linearity present in the long range tuning data is likely due to an additional tuning effect from the applied tension also modulating the index of refraction in the silica sphere. [58]

It should be emphasized that for performing fairly long range tuning (300+ steps) of DSSs with narrow (20 microns or less) stem waists, the sample should be lowered away from the sphere and a lower step voltage closer to 30 V used. The dynamic force on the DSS during each individual step exceeds the static stretching force, and if a higher step voltage is used with a thin stem, it increases the chance of the sphere snapping. The sample should be lowered down for the long distance tuning process in case the stem does in fact fail under tension. If the sphere is in contact with the sphere or close by when it fails under high tension, the energy it releases is enough to damage any of the membranes it hits. This occurred once and damaged approximately 50 percent of the best membranes.

Given the capacity to tune several hundred megahertz and the ability to choose from four different sets of SiV transitions, we are well situated to be able to tune an equatorial WGM into resonance with an SiV even if it is initially relatively detuned from the closest SiV transition.

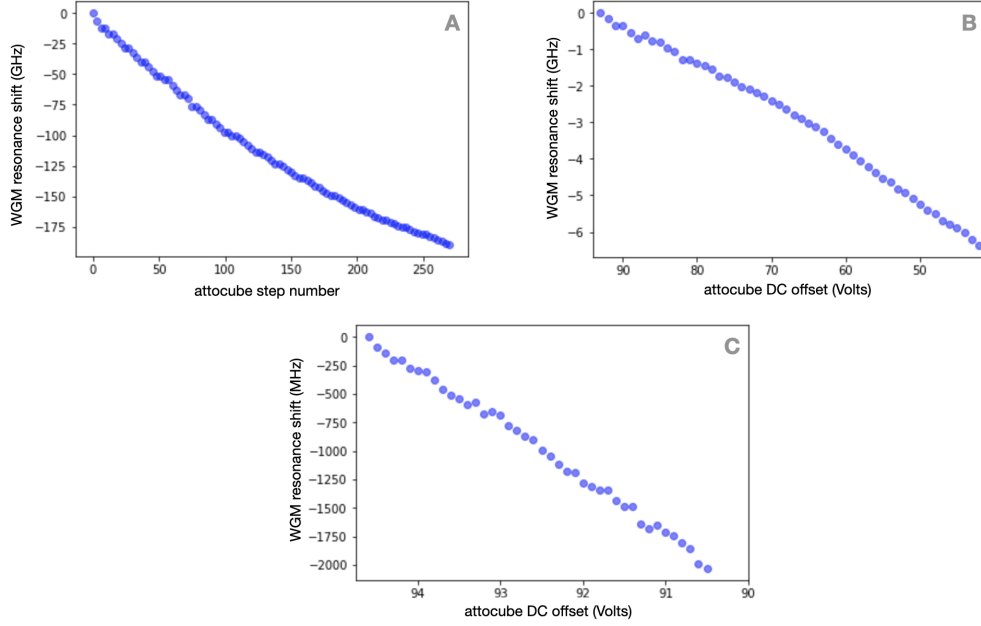


FIGURE 7.2. Data showing WGM frequency shift data from strain tuning experiments. A) Long range tuning data utilizing the attocube step function. B) Tuning data using the continuous DC offset mode over 60 volts of its 150 volt range. C) DC offset tuning data over a narrower 5V range to demonstrate the tuning resolution. Note that this data was taken using the first cryostat system design which was more sensitive to ambient system noise. Also note that the need to readjust the taper coupling over the course of the experiment introduces some variation due to frequency shifts from the taper coupling.

#### 7.4. Vibration Performance

Because vibration proved to be such an issue with the original cryostat design, data were taken using the new redesigned system to verify the system's stability when the cryostat is in operation. These data were collected by taking the traces of the cavity transmission spectrum while the cryostat was running, and gating the data collection at fixed delays relative to the 1 Hz trigger signal output from the cryostat which is synced with the operation of the cold head. In addition to this data, the various modes observed for this experiment were also measured

with the cryostat fully stopped to obtain the "natural" linewidths of the modes when they are not being effectively broadened by cryostat noise.

For the 1 second cycle period of the cryostat, data was collected at delay intervals of 100 ms. For each mode, the data set consists of 9 traces. Due to inefficiencies of the oscilloscope trigger, the scope would not consistently acquire at the proper moment of the signal burst which scanned the laser frequency. As a result, data acquisition of all 9 traces for each trigger delay time took place over several minutes, rather than the 9 second time it would take for the cryostat to complete 9 piston cycles. As a consequence, longer timescale drifting of the modes was a significant factor in the broadening of the average linewidths. This drift was likely due to intermittent contact of the membrane with the sphere and will be discussed in more detail later in this section.

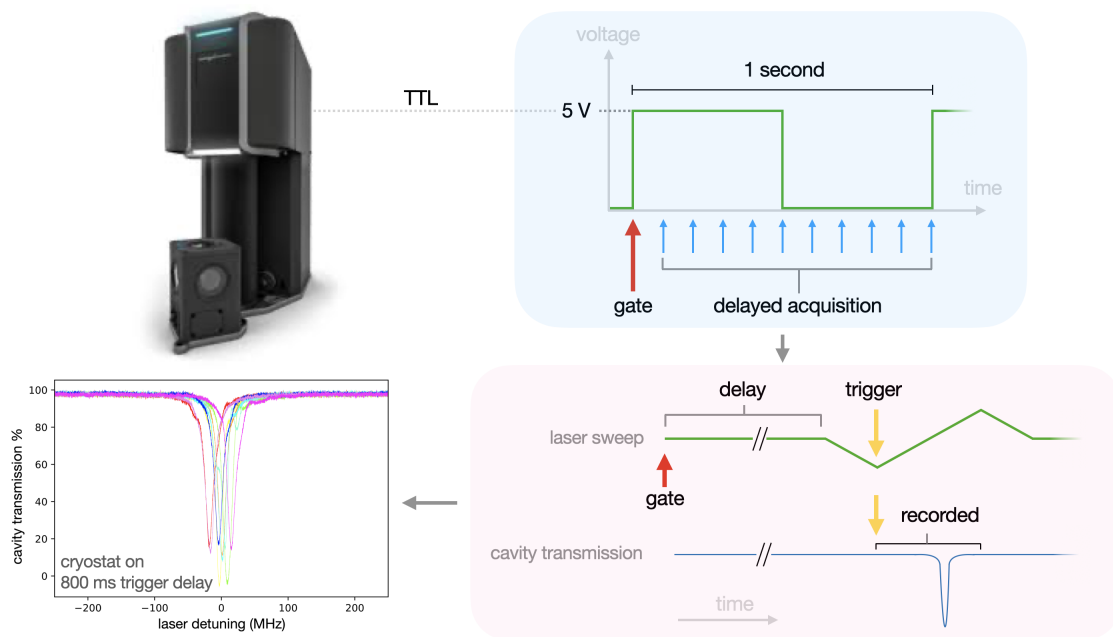


FIGURE 7.3. Illustration of the data acquisition scheme used to measure the effective cavity broadening at different points in the cryostat cold head cycle.

It is important to emphasize that the broadening of the modes discussed in this section is not physical in that it is not due to any change of the cavity decay rate, but instead an artifact of a non-stationary mode in frequency that results in apparent broadening due to the averaging/integration time inherent to the data acquisition process.

Data were collected of an 18 MHz near-equatorial mode ( $l - m + 1 = 3$ ) not in contact with the membrane and slightly under-coupled. Tension on the sphere was 200 attocube steps past being slack using a 30 volt step size for driving the positioner. Note that using higher voltage step sizes increases the risk of snapping the sphere due to higher dynamic forces over the duration of the step. Unless using a sphere with stems much thicker than 15 microns at the taper waist, using step voltages of 40+ volts will consistently result in structural failure before the attocube hits its stick-slip limit.

Note that of the different trigger delay values used, the maximal average linewidth observed was 30 MHz, giving a maximum effective broadening of 15 MHz. Also note that the reference trace of the mode taken when the cryostat is stopped was 60 percent coupled compared to the 80 percent coupling while the system was running, so the relative broadening is actually slightly less than the data suggests. This demonstrates minimal sensitivity to sound conduction and vibration, the effects of which can be further reduced by gating data collection using the cryostat trigger output to collect data only during the intervals of the cycle with minimal effective mode broadening. As an example, if data were only taken around the 700 ms delay period, the apparent broadening due to cryostat operation would only be 2 MHz.



Even without gated data collection or post-selection, these results are promising, especially when taken into consideration that the equatorial mode linewidths while in contact with membrane will typically be closer to 30 or 50 MHz. While no noise data were collected for the original system design, this is a significant improvement in performance. With the old system design, while the sphere was under tension, the frequency modulation of modes was so intense that it made it difficult to obtain an average trace that resembled a lorentzian or even a centralized peak. The modes would oscillate hundreds of megahertz about their center frequency and the timescale of the ring-down process was roughly on the same order as the period between piston cycles making gated data acquisition or post selection infeasible. In some cases, the maximum amplitude of the frequency oscillation of the mode could be as large as tens of gigahertz.

Data were also collected for various modes at low and high tension while the sphere was in contact with the membrane. As can be seen from figures 7.5 and 7.6, the effective broadening was greater with the membrane in contact. This is indicated both by the linewidth of the average traces for each time delay as well as the average trace acquired through the scope by integrating 128 successive frequency sweeps for a frequency sweep rate of 80 Hz. One point of interest is that in most cases, the best fit linewidth of the average trace for each time delay is greater than the linewidth found from the average trace obtained using continuous averaging with the scope. A potential explanation for this can be inferred from noting how the center frequency of the mode fluctuates over the course of the 9 scans for a given trigger delay. The successive traces are colored in chromatic order from red (first) to violet (last). Notably in many of the trigger delay plots, the successive mode traces seem to show a continual smooth drift of the mode

frequency in one direction. This is in contrast to a random distribution not ordered in time that would be expected if the only cause of the spread was the rapid frequency modulation caused by sound conduction into the sample chamber.

The likely cause of continual drift in frequency is thermal fluctuations of the sphere. Especially at the cryogenic temperatures used for these experiments, the temperature dependence of the index of refraction in silica is fairly sensitive. Due to the fact that the principal cooling source for the sphere is conduction through the membrane and not cooling through the silica sphere stems, if contact with the membrane is interrupted the heating/cooling, load will change and the sphere temperature will no longer be in a steady state leading to a frequency drift as the system moves towards a new thermal steady state.

The process leading to the intermittent sphere-membrane contact is likely due to motion of the membrane itself. The negligible amount of coupling noise observed from these data (variation in taper/cavity coupling rate) indicates that the sphere-taper gap is stable and neither component experiences significant motion due to mechanical modes driven by impulse or noise from the cryostat piston. This leaves motion of the membrane itself as the source of the intermittent contact. The membranes resembling cantilevers are likely behaving as very poor mechanical resonators that are driven by the vibration/sound conduction from the cryostat. In some cases when the contact between the sphere and membrane is fairly light, intermittent contact can be observed through the imaging CCD for the system. When the membrane is in contact with the sphere and proper objective focus is used, newton rings can be seen at the contact point due to the interference effects of two medium boundaries separated by a small distance. When the membrane is in contact, the center of the newton ring pattern is a dark

circular spot surrounded by concentric interference rings. When the contact force between the two components is fairly light, the center spot of the interference pattern can actually be seen to “blink” in sync with the cycling of the cold head. This blink is also accompanied by a rapid frequency shift in the mode spectrum followed by a drift back to its original position. A variation in the pattern of the newton rings indicates that the separation between the sphere and membrane is varying, in this case from contact to some non-zero separation. If the amplitude of the initial thermal frequency shift is larger than the distance in frequency, the mode is able to drift back towards its initial steady state position. The end result will be a continual shift away from the original frequency position of the mode over time. Thermal fluctuations of the WGM resonances ceases when the cryostat is stopped.

To a certain extent, the intermittent contact can be avoided by slightly raising the membrane a few extra steps, such that the membrane is forced away from its natural equilibrium position by the sphere. In the case of the particular experimental run used to collect the vibration data, the thermal drift was worse than what is typically observed. Generally, slower timescale motion of modes in frequency should be unnoticeable, but for this particular experimental run, it was present, and increasing the pressure of the sphere on the membrane had little effect. Time constraints on concluding research for this project prevented repeating this experiment with different conditions to mitigate the drift.

As has been mentioned in other sections, the most desirable membranes to use are the longest ones with a more gradual taper, because they make it easier to find the region of optimal coupling where the membrane has the least negative impact on the cavity linewidths. The flip side to this is that longer, thinner

membranes are less rigid, and consequentially, their motion is difficult to damp via contact with the sphere. The magnitude of thermal fluctuations for this run was anomalous and it is possible the specific membrane used has a particular problem causing it to move more, as this problem has not been nearly as pronounced for past tests of the system using other long membranes. If this problem persists, it could be mitigated by using some of the shorter membranes which don't tend to have the same issue. This could potentially come at the cost of greater actual q-spoiling due to coupling at a thicker point on the membrane but still a net gain from the reduction of thermal drift.

Because of the manner with which these particular data were taken, there is no way to analytically and precisely decouple the effects of the longer timescale drift from the shorter timescale fluctuations due to strain modulation. Therefore, it is difficult to make a precise quantitative analysis of the stability of the system with regards to noise from acoustically driven strain modulation. That said, qualitatively, the data do seem to suggest that a significant factor leading to broadened average linewidths for each trigger delay is slow drift. At several different values of trigger delay, the linewidths of the individual traces more closely resemble the linewidths of the modes with the cryostat stopped or the trace made from continuous averaging than the linewidth of the averaged trace for the particular trigger delay. This suggests that a large portion of the broadening is due to fluctuations with a characteristic timescale at least as long as the 6.25ms duration of the frequency sweep used to acquire each trace.

Further, as an illustration, looking at the case of a 400 ms trigger delay from figure 7.5, if we make the rough approximation that the rate of drift was constant and the intervals between each successive trace was constant, we can correct the

data for the assumed drift to recover a narrower averaged linewidth. Given these assumptions, the averaged linewidth is reduced from 117 MHz to 56 MHz, which is less than the averaged linewidth of the trace acquired from 128 iterations of continuous averaging over a full cycle of the cryostat piston.

While this model uses a fairly crude approximation of the long time scale drift, the fact that it was able to reduce the averaged linewidth by over 50 percent is indicative of the significant impact of long timescale drift. Similar rough analysis of data with the same model for other trigger delays and tensions suggests slow drift is a major contributor to averaged mode broadening when the membrane is in contact with the sphere. Further, because the model made an overly simplistic approximation of a constant rate of drift and constant intervals between data acquisition, a more accurate model would likely have lead to greater reductions of the averaged linewidths for each trigger delay.

For performing actual cQED experiments where the cavity-SiV detuning is an important variable that needs to be finely controlled and stable, it is not possible to simply analytically compensate for drift in the data analysis for such experiments. The issue needs to be resolved physically. As mentioned previously, the issue will likely be solved through the appropriate choice of membrane and the coupling spot on the membrane used, picking a membrane and spot that minimizes the intermittent contact with the sphere. Given that intermittent contact with the sphere could also be causing frequency modulation of the cavity resonances leading to further broadening, solving the drift issue could result in a reduction of averaged linewidths better than would be suggested by a model that perfectly accounts for slow drift.

If the use of different membranes fails to resolve the issue, it could potentially be managed through feedback control of the stretching attocube, using tension modulation to maintain a stabilized cavity resonance frequency. Lastly, data could always be collected intermittently during intervals when the cryostat is stopped completely. With the drift issue resolved for a running cryostat, gated data acquisition can then be employed when necessary to achieve optimized cavity linewidths.

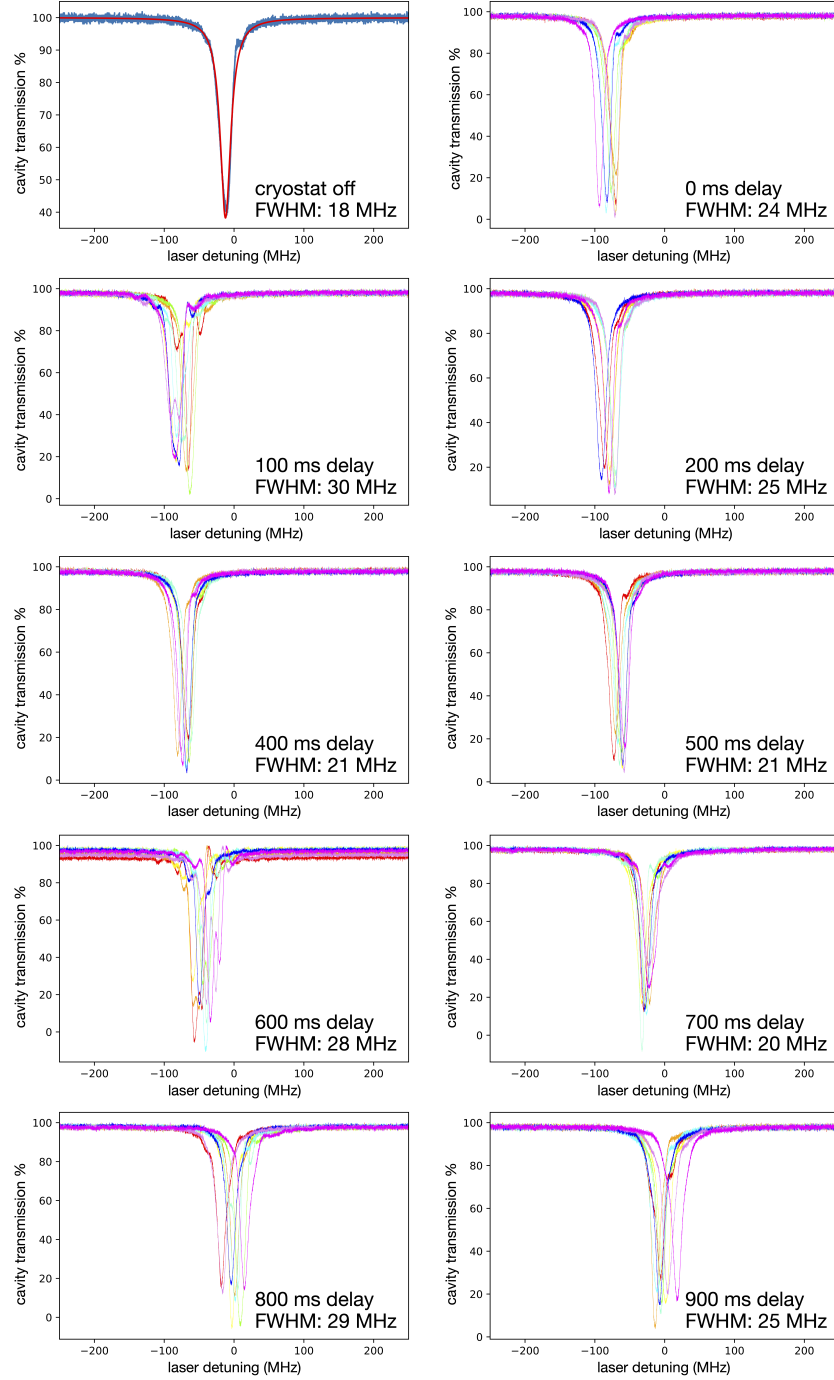


FIGURE 7.4. WGM frequency noise data consisting of 9 successive frequency scans gated by a set delay time relative to the 1 Hz trigger output from the cryostat. A single scan of the mode with the cryostat off is used to establish the natural linewidth of the mode. The linewidth of the averaged trace is given for each delay. The specific WGM is a near equatorial ( $l - m + 1 = 3$ ) mode which has been tightened to 200 attocube steps past being slack using a 30V step size.

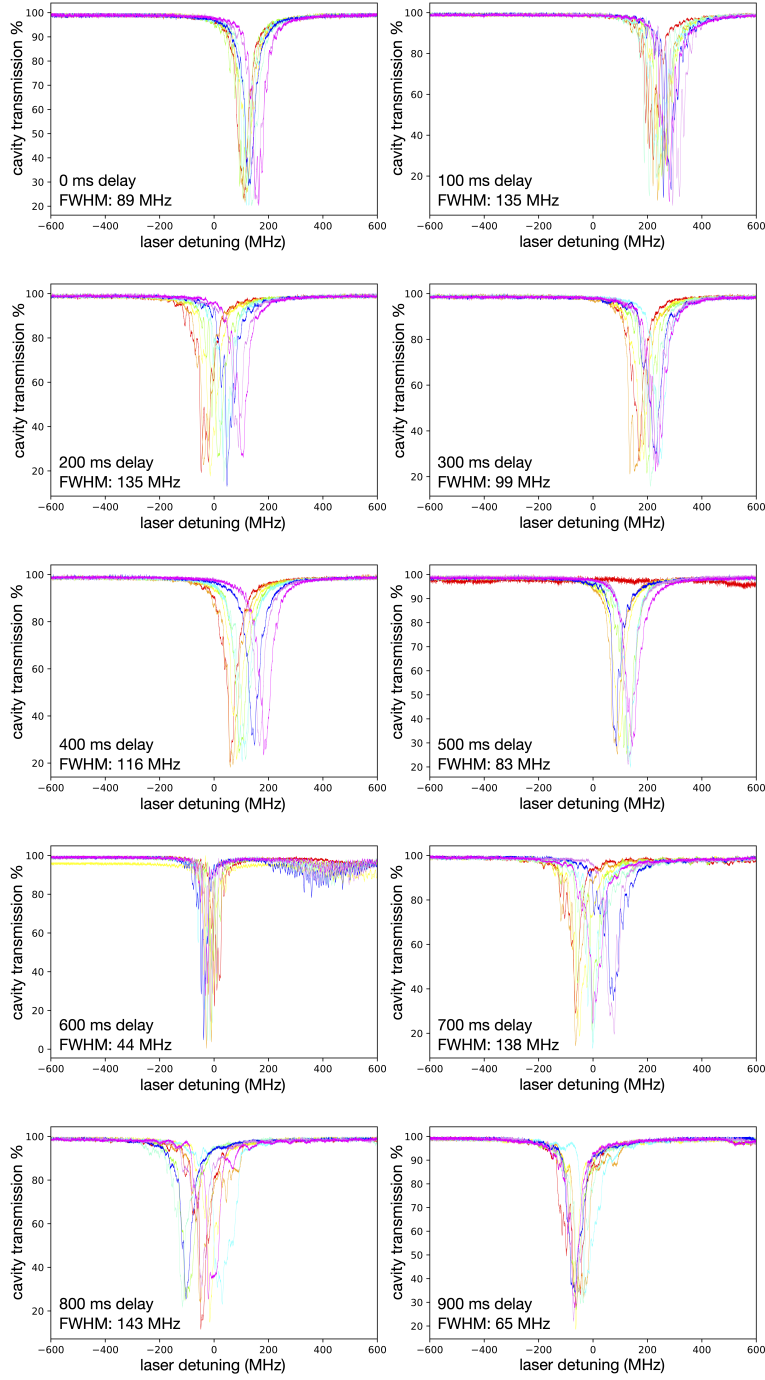


FIGURE 7.5. Vibration data for an  $l-m+1 = 3$  WGM with the DSS tightened to 50 attocube steps past slack. 9 successive WGM traces are taken for each trigger delay, and the best fit linewidth is given for the cumulative average curve for each delay set.



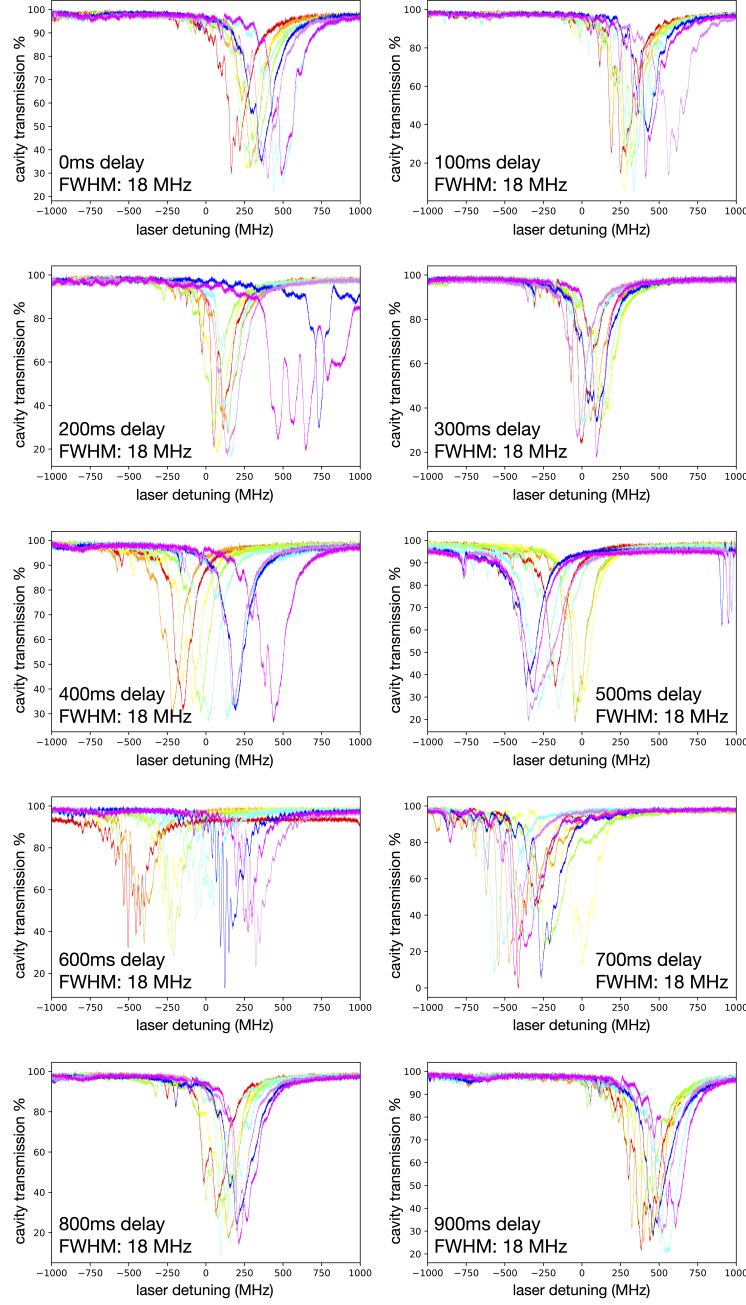


FIGURE 7.6. Vibration data for an  $l - m + 1 = 3$  WGM with the DSS tightened to 150 attocube steps past slack. 9 successive WGM traces are taken for each trigger delay, and the best fit linewidth is given for the cumulative average curve for each delay set. Contamination of the sphere led to a larger intrinsic WGM linewidth.

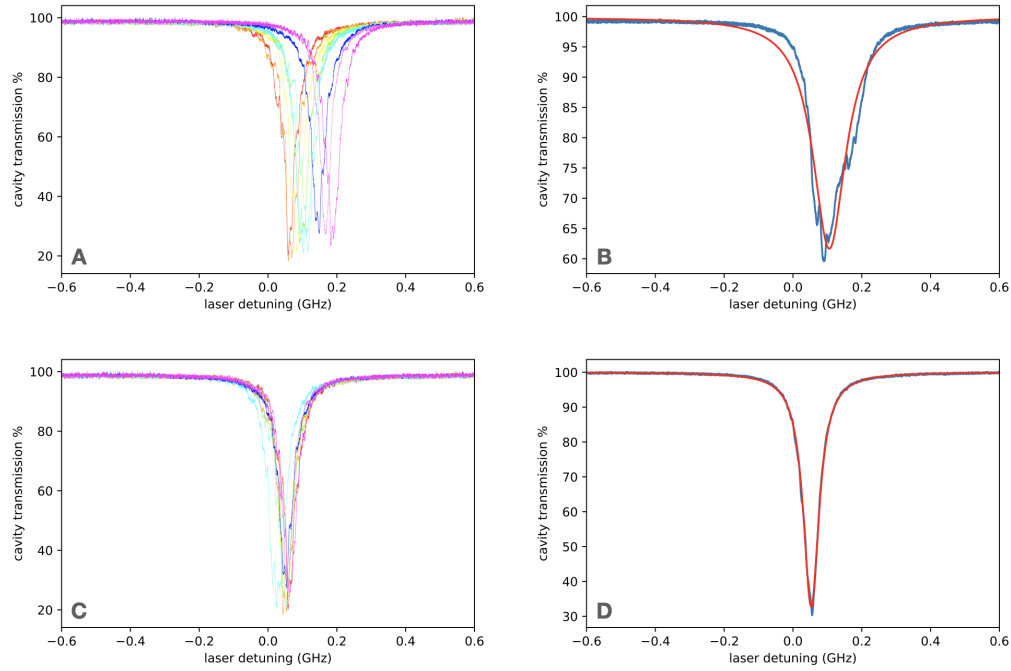


FIGURE 7.7. Reduction of averaged WGM linewidth via a naive drift correction model. A) Successive cavity resonance scans taken at a 400ms delay relative to the cold head trigger signal. Colored in chromatic order from red (first) to violet (last). B) averaged trace (blue) and lorentzian best fit model (red) which gives a linewidth of 117 MHz. C) Corrected WGM traces shifted in frequency assuming constant rate of drift. D) Averaged trace with the correction applied (blue) and lorentzian best fit (red) which gives a linewidth of 56 MHz.

## CHAPTER VIII

# COUPLING BETWEEN SILICON VACANCY CENTERS AND WHISPERING GALLERY MODES

### 8.1. Introduction

In this chapter, I will cover results of spectroscopy of the SiV-cavity system to verify optical coupling of SiVs into the cavity modes. PL and PLE spectroscopy were used to observe SiV fluorescence collected by the sphere and coupled from the tapered fiber into the collection path, demonstrating that the SiVs within the membrane at the diamond-sphere contact point do, in fact, optically couple to the WGMs of the cavity. I will revisit the estimate for  $C \approx 11$  made in chapter 2 in light of the experimentally observed values of  $\kappa$  and  $\gamma$ .

### 8.2. PL and PLE Spectroscopy

For the initial high SiV density samples, both PL and PLE data were taken demonstrating optical collection of the SiV fluorescence through the tapered fiber via optical coupling to the DSS cavity modes. PL spectra were collected via spectrometer using CW green excitation. Typically, three minutes was used as the standard integration time. Initial alignment of the excitation laser with the contact point can take a few tries to optimize, so it is ideal to use the 3 minute integration time to help identify the SiV fluorescence when the initial alignment is off and the signal is low. However, reduced integration times can be used once the system is optimized. PL spectra of the SiV fluorescence reveals two peaks, which indicate the excited state splitting of the transitions. Note that the presence of

only two peaks, and not the four that are expected from the four different optical transitions, is due to the limited resolution of the spectrometer. The roughly 2 angstrom resolution is not sufficient to resolve the 50 GHz SiV ground state splitting. The observation of SiV fluorescence is significant in that it demonstrates there is optical coupling occurring between the SiV and the cavity modes.

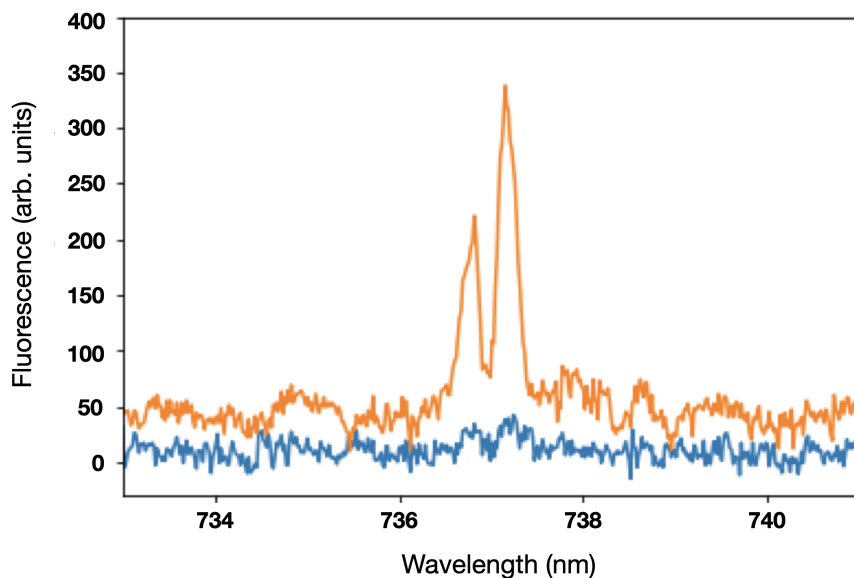


FIGURE 8.1. PL spectra of the sphere-membrane system showing two peaks separated by the SiV excited state splitting. The blue line is from data collected with no 532 nm excitation, using the same integration duration as a control to distinguish SiV fluorescence from background.

Sometimes the PL spectra will show additional peaks, such as multiple peaks red-detuned from the SiV transitions. Typically, these peaks are much weaker and spectrally separated from each other by a distance that seems to possibly correspond to the free spectral range of the cavity. This is likely indicating effective collection of the SiV phonon side band by equatorial and near equatorial modes that are well coupled to the fluorescing SiVs. This could potentially be used as a way to check that the membrane/sphere configuration is optimally configured.

Another phenomenon that is sometimes observed is a third peak, comparable in amplitude to the expected SiV transition fluorescence, and slightly blue detuned by a distance roughly comparable to the SiV excited state splitting. It seems that the presence of this peak is dependant on the sphere being in contact with the membrane, but the actual cause is not understood. Typically, PL can be observed when the 532 nm laser is focused away from the contact point, with a reduced PL count rate the further the 532 nm spot is away from the contact point. This is potentially due to the SiV fluorescence coupling into some sort of waveguide mode within the membrane, that then propagates to the contact point where some of the fluorescence then couples into the cavity and is collected via the tapered fiber. This third peak is only ever visible with the 532 nm focused at the contact point, which indicates that something about the contact with the sphere is necessary for it to be present. The presence of the third peak is not consistent with any expected cQED effects. It was considered that the third peak could in fact be from SiV transitions which have been shifted by strain effects at the cavity site; however, PLE scans taken in cases where the third peak was visible never revealed any features that obviously corresponded to the peak visible in the PL data. Additionally, a survey of SiV strain splitting shows there is limited strain present at the tips of the membranes.[28] It still remains unclear whether this feature results from some sort of interaction with the SiVs, or if it is due to an entirely different color center or another phenomenon.

PLE spectroscopy of the same high SiV density system has a much higher resolution, limited only by the laser linewidth ( $\sim 200$  kHz) and laser tuning step size used. Consequentially, PLE spectroscopy reveals all four SiV transitions. PLE data were taken both with 532 nm initialization and without 532 nm initialization as a

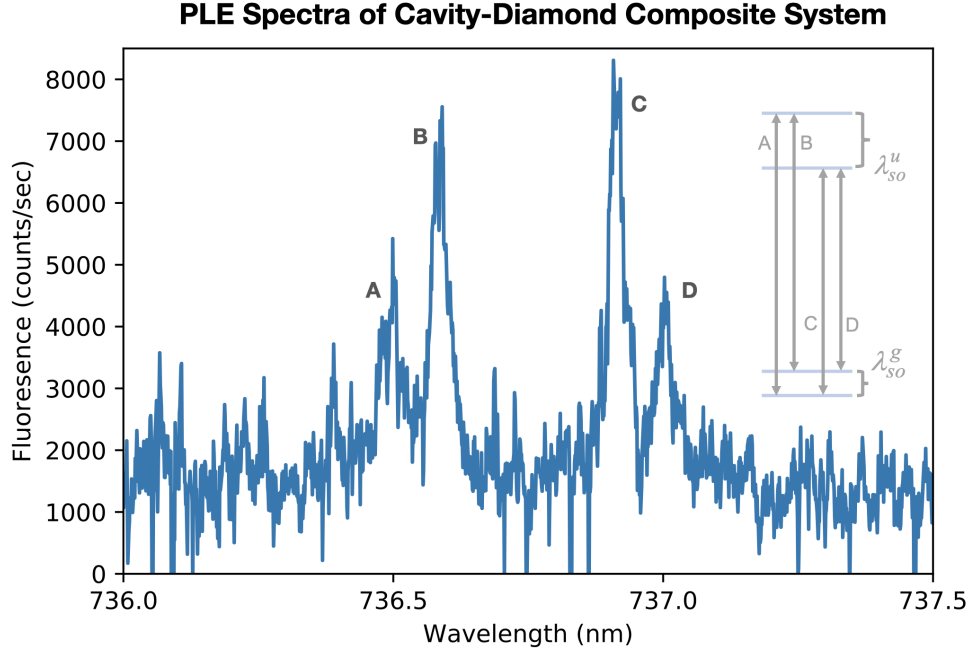


FIGURE 8.2. PLE spectra of the sphere-membrane system using the original high SiV density membrane sample. All four SiV transitions are visible. The data has been background subtracted using an identical PLE scan that was taken without off resonant 532 nm excitation.

means for comparison to identify and distinguish SiV fluorescence from the leakage of cavity mode transmission as well as other potential sources of fluorescence.

While a tunable band-pass filter is used to block the resonant driving laser, there is still measurable leakage of the 737 nm light into the detector that comes from scattering of the 737 nm light into the cavity modes which are then collected by the taper. Identification of fluorescence peaks that are present in both scans with and without 532 nm initialization serves as a means for identifying which peaks are due to factors other than SiV optical transitions.

One important detail lacking in the PLE spectra for the initial higher density samples used is the presence of individual smaller linewidth peaks indicating single transitions from individual SiVs. Assuming the cavity is coupling to multiple SiVs,

unless there are factors causing significant broadening of the transition linewidths, it should be possible to resolve single transitions from a single SiV. PLE scans of the system using greatly reduced excitation power did not result in resolvable peaks with linewidths corresponding to the known linewidths of individual SiVs in the sample (200-500 MHz). This rules out optical power broadening as a limiting factor to single SiV resolution.

One possible contributing factor is thermal broadening. While it is known that the  $\Delta T$  from the cold platform to the sample mount is only around 0.2K, that value does not necessarily reflect the temperature at the sample itself. While the actual temperature of the sphere is not known, the observed frequency shift of the cavity mode spectra upon contact with the membrane indicates a difference in temperature between the two components and cooling of the sphere via thermal contact with the cold membrane. Due to the fact that the membrane is acting as a heat sink for the sphere, it is not known whether the membrane maintains a temperature similar to that when it is not in contact with the sphere, or if the additional heat load from the sphere causes an appreciable temperature increase after the system reaches a steady state. Due to the inability to spectrally resolve single SiV transitions with this data, it was not possible to determine the potential impact of thermal broadening.

A second possibility is that something about the mechanics of the contact between the sphere and membrane, such as charging effects, is impacting the SiVs. Confocal PLE spectroscopy of the membrane alone verifies that SiV linewidths are preserved after the membrane fabrication process. Any mechanisms broadening the transitions would therefore need to be due to the presence of the sphere. While the symmetric structure and lack of a permanent dipole help to protect

the SiV from the effects of electric field noise in its local environment, given a sufficient amount of electric field noise, there will eventually be an impact. Since the silica comprising the sphere and the diamond of the membrane are two different materials with different electronegativities, even stationary contact between the two will result in local charge formation from the triboelectric effect, the phenomenon responsible for the buildup of static charge from surface contact between two materials. We have not attempted to model the potential magnitude and charge mobility of the triboelectric effect at the contact point, so the potential impact on the SiV linewidths is unknown. Again, because individual SiV transitions are not resolvable in the PLE data, it is difficult to make any assessment of its impact.

Lastly, a third factor that could be at play with this data is the spacial density of SiVs in the membrane. If the density is sufficiently high, depending on the typical transition linewidths, the sphere could be coupling to a sufficiently high number of SiVs such that they all overlap in frequency and form a continuous distribution of SiV fluorescence. All three of these factors could be contributing to the inability to resolve single transitions, and it is difficult to tease out the solution from the data.

In an attempt to solve this issue, a new membrane sample was fabricated using a lower SiV implantation dose intended to result in a lower spatial density of SiVs in the membrane. Secondly, the etch process used to form the tapered thickness profile of the membranes was extended, resulting in thinner membranes which also removed more SiVs via etching.

PL spectroscopy of the system incorporating the new lower SiV density membrane sample resulted in the same expected double peak indicating coupling



of fluorescence into the cavity, albeit with a lower intensity likely due to the fluorescence of fewer SiVs. Fortunately, PLE spectroscopy of the system reveals peaks that no longer resemble a smooth distribution of fluorescence around where we expect to find the transitions, and further, some details look as if they could be from single SiV transitions. Note that for wide PLE scans covering the full range of all four transition groups high power 737 nm is typically used. This is because for PLE spectroscopy of the system given the coupling of 737 nm scatter into the modes, it is generally necessary to be more aggressive with blocking the laser beam than you would typically need to be with PLE spectroscopy using a confocal setup only. As a consequence of using a higher cutoff wavelength, more of the already small phonon side band is rejected leading to reduced fluorescence counts. This results in a lower signal to background ratio than what is achievable with PL spectroscopy. This makes it preferable to use higher power to reduce integration times when possible.

A narrow frequency PLE scan of the spectral region corresponding to the SiV B transitions shows multiple resolvable peaks within a frequency range of less than 10 GHz. A narrower view from this scan shows what appears to be 5 or more individual fluorescence peaks with linewidths less than 1 GHz, many possibly closer to 500 MHz in width. This scan was performed at higher 737 nm power which should lead to power broadening. To obtain clearer data of individual peaks, a narrow frequency PLE scan was also taken of the SiV C transition group. Two peaks on the edge of the C transition distribution were chosen for closer scans to reduce the potential for multiple overlapping transitions presenting as single SiVs with broadened linewidths.

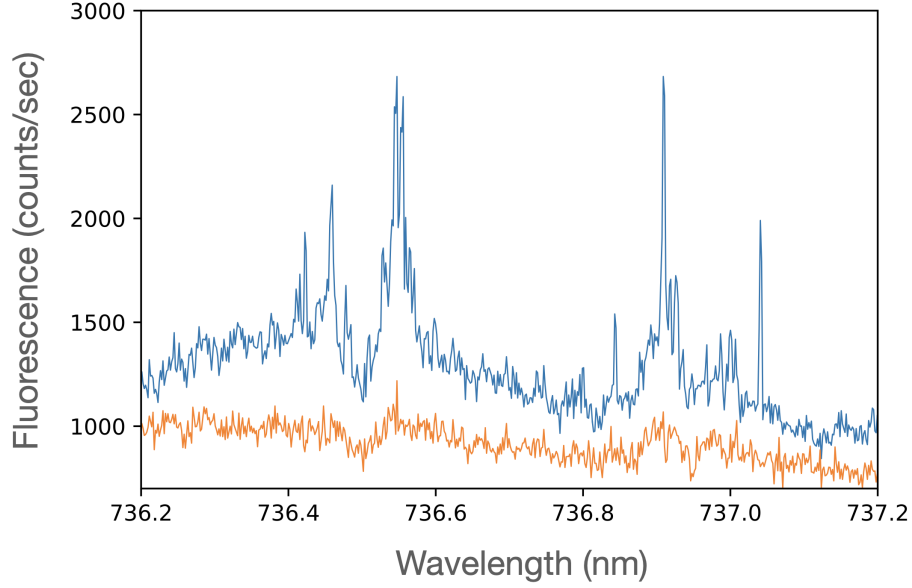


FIGURE 8.3. Blue line: PLE spectra of the sphere-membrane system using the low SiV density membrane sample. Orange line: control scan taken with zero 523 nm initialization pulse. Much sharper features are visible suggesting single SiV transitions.

A narrower PLE scan of the system centered on the group of C transitions reveals two fluorescence peaks with linewidths of 880 MHz and 650 MHz. A repeat of the same scan, but at reduced 737 nm power, reveals reduced linewidths of 250 MHz and 370 MHz respectively, indicating the presence of power broadening in the previous scan. The presence of these peaks, in conjunction with their observed power broadening and linewidths consistent with those measured using confocal PLE spectroscopy of the membrane alone, supports that these peaks indicate transitions of two individual SiVs. This is important because 1) it means that cQED experiments can be performed utilizing individual SiVs and 2) neither broadening from higher membrane temperatures nor electric charge noise from the membrane-sphere contact are dramatically degrading the SiV optical quality. This

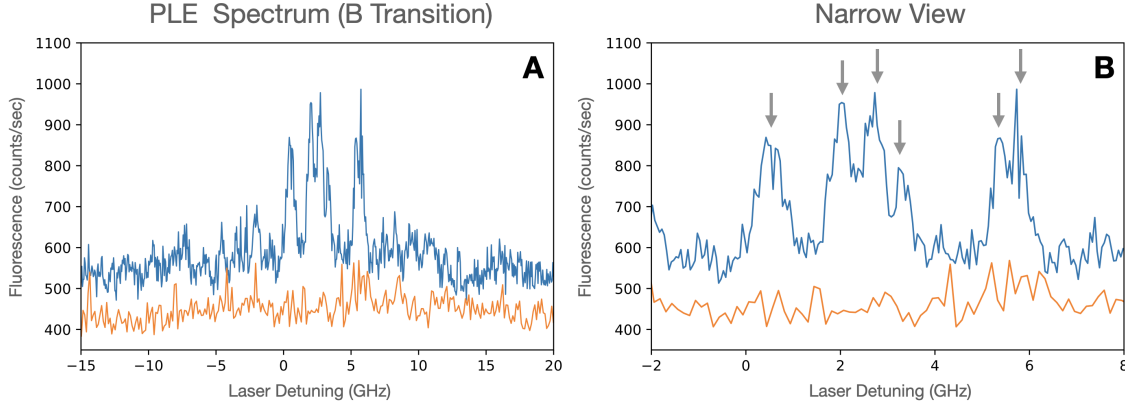


FIGURE 8.4. A) PLE scan of the SiV B transitions. B) A narrower plot of the data with arrows identifying potential single SiV transitions.

serves as a means to verify that effective cooling of the membrane is still occurring even with the added heat load of the sphere in contact.

### 8.3. Revisiting the Estimate for $C$ in the Composite cQED System

From the data collected in this chapter as well as the previous, linewidths for both equatorial cavity modes and single SiV transitions were measured. The fluorescence of one particular transition for a single SiV was found to have a linewidth of  $\gamma/2\pi = 250$  MHz, and an equatorial cavity mode demonstrated Q-spilling of only 3 MHz when brought into contact with the diamond membrane (with a total broadened linewidth of 38 MHz). Both of these values are relatively comparable to the estimated values of  $\kappa/2\pi$  and  $\gamma/2\pi$  used in the theoretical calculation for the achievable cooperativity of the system in chapter 2 ( $C \approx 11$ ).

Keeping the same theoretical value for  $g/2\pi$  of 150 MHz and using the measured best case (so far) values of  $\kappa/2\pi = 38$  MHz and  $\gamma/2\pi = 250$  MHz gives a cooperativity of  $C \approx 9$ , well within the regime where cQED effects should be visible in cavity transmission and PLE measurements for small or

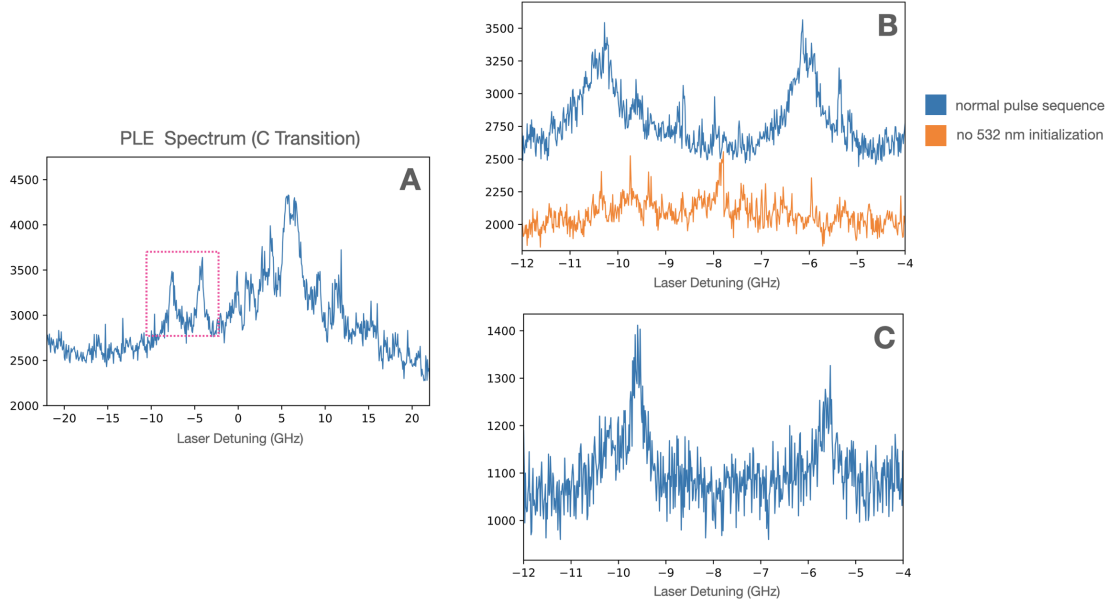


FIGURE 8.5. A) Wide frequency PLE scan of the SiV C transitions. B) A narrower scan of the two peaks shown within the outlined box in A. C) A repeated scan of both peaks but with reduced 737 nm power, revealing narrower fluorescence peaks of presumably single SiV transitions.

zero cavity-SiV detuning. Given that a confocal PLE spectroscopy survey of the membrane by itself showed some SiVs with linewidths even closer to 200 MHz, even higher cooperativities could be achievable. Limited time was spent trying to find transitions in the composite system with the smallest linewidths so this seems very plausible. Even in a less ideal scenario where the cavity modes are especially broad and minimal effort is put into finding narrow SiV transitions, values of  $\gamma/2\pi = 350$  MHz and  $\kappa/2\pi = 100$  MHz still give a cooperativity of  $C \approx 2.3$  which would still be detectable through PLE and cavity transmission measurements.

While  $g$  has yet to be measured through cQED specific experiments, these results are encouraging as it so far confirms the viability of this system for performing experiments in the good cavity regime where  $C > 1$  and  $g > \kappa$ .

## CHAPTER IX

### GUIDANCE FOR FUTURE WORK AND CONCLUSIONS

#### 9.1. Introduction

At the conclusion of research, this project is on the cusp of performing experiments to observe cQED effects of SiV-cavity coupling through cavity transmission and PLE spectroscopy measurements. Significant progress has been made to resolve the major roadblocks towards realizing SiV coupling experiments, including reduction of vibration sensitivity and the fabrication of a low SiV density membrane sample. As has been shown in the previous chapters, the system does in fact exhibit SiV optical transitions and equatorial WGMs with appropriate linewidths to operate in the desired good cavity limit, and theoretical estimates suggest that the coupling rate,  $g$ , should also be sufficient to observe cQED effects of SiV-cavity coupling. The system and methods currently used for experimentation thus far should already be sufficient to observe cQED effects; however, in addition to performing those experiments, there are further actions that could be taken to optimize the system performance, enhance the longevity of the system, and increase the quality of data collected. Here I will cover recommended further work to mitigate existing issues and provide better control of the experimental system, as well as next experimental steps that should be taken to finally observe cQED coupling between the cavity and SiV optical transitions.

## 9.2. Further Modifications for Vibration and Acoustic Susceptibility

In terms of further limiting the effects of vibration on data collection, the only structural changes that could be made would be on the outside of the vacuum chamber. The vacuum chamber and the cryostat are both mounted on a structural carrier plate and connected via a thermal cross link under vacuum which is what thermally connects the cold platform of the vacuum chamber to the cold finger of the cryostat. The cross link design uses several spring-like clamps to limit vibrations transmitted through the cross link. The structural carrier plate, however, is completely monolithic and ridged. To further increase the vibrational isolation, the cryostat could be mounted on a separate bench, not connected to the optics bench containing the vacuum chamber, and the carrier plate could be cut so that the only mechanical link from the cryostat to the vacuum chamber would be the flexible cross link.

In order to limit sound conduction into the vacuum chamber, the cryostat could be mounted on top of a layer of material to dampen the conduction of sound from the optics bench. Additionally, acoustic foam could be placed around the vacuum chamber to attenuate ambient sounds from the room which can also include sounds from the cryostat itself that propagate through the air as well as the cross link. It is likely most of the sound conduction into the sample chamber comes from the cross-link and the carrier plate bolted to the optics bench, however, the addition of sound damping foam around the sample chamber is extremely simple and cheap and could still be beneficial for very precise measurements of the cavity mode spectrum.

Lastly, one non-structural option to address vibration from the cryostat would be to gate all data collection using the timing trigger for the cryostat piston.

By omitting data collected based on its time of collection relative to the cycling of the cryostat piston, the impact of cryostat noise can be limited. Because certain elements of the system, such as the taper and sphere, have vibrational modes that can be resonantly excited through the impulse of the cryostat piston, the trigger for data collection can be timed such that the relevant data is only collected after the initial piston cycle, plus an additional delay period to allow the ring-down of those mechanical modes. Because the resonance frequencies and decay rates of the various mechanical modes can vary from sphere to sphere or taper to taper, etc. (as well as vary with changes in tension), the gated collection window will need to be adjusted on a case by case basis, or a much more conservative collection window could be used across the board at the expense of longer integration times.

As was shown in the section on vibration data in the results chapter, absent any additional sources of ambient sound in the lab, the system is exceptionally stable when the compressor is stopped temporarily which allows for just under 4 minutes to complete an experiment before the sample temperature climbs from 3K to 10K. It is certainly workable to run an experiment in that time frame, however, it would be advantageous if that time could be extended. As has been previously mentioned, one effect of the large copper mass of the outer mounting pedestal is its functioning as a thermal battery. Its presence in the system greatly prolongs the cool down and warm up process. Both the central pedestal and the outer pedestal are coupled to the cold head of the cryostat. However, the thermal connection of the central pedestal is significantly better than that of the outer pedestal. The outer pedestal is mounted on the PCB boards which are gold plated to enhance thermal conductivity, and those are in turn mounted to the cold platform via an

aluminum mounting bracket. At cryogenic temperatures, the thermal conductivity of aluminum drops to almost a hundredth that of high purity oxygen-free copper.

For most other system users, that design works perfectly fine, and the system maintains the PCB boards at around the same set temperature as the sample. In this case, however, the outer copper pedestal has significantly more surface area than the PCB boards alone. This, in conjunction with the fact that it has a large thermal mass and comparatively poor thermal conductivity, means that it does not achieve the same target temperature as the sample, and there is not an efficient thermal connection between the sample and the outer pedestal.

If an effective thermal short was added between the base of the sample pedestal and the outer pedestal, it would accomplish two things. First, it would allow the outer pedestal to reach the 3-4 K target temp, and second, it would allow the outer platform to act as a more effective thermal battery for experimental runs while the cryostat is turned off. The presence of a colder and better thermally coupled outer pedestal would behave as a more effective “cold-reservoir” to extend the 3 K to 10 K warm-up time while the passive heating power on the sample for a turned off cryostat would remain the same as it is now. It is possible that a better thermally connected outer platform could also have benefits for the vacuum performance at cryogenic temperatures as the colder surface area of the pedestal would further assist in cryo-pumping on the vacuum chamber.

No attempts have been made to measure the temperature of the sphere mounting bracket or the sphere itself while the system is running at cryogenic temperatures. Due to the low cross-sectional area of the sphere stems and poor thermal conductivity of silica at low temperatures, there may not be an appreciable change to the sphere temperature (while not in contact with sample,)



but some improvement might occur. Any such gains could potentially be further improved by using small amounts of silver thermal paste applied to the thicker sections of the DSS stems to increase their thermal conductivity. If improvements can be made to significantly reduce the  $\Delta T$  from the sphere to the membrane, this might help to eliminate one more source of frequency fluctuations in the cavity modes. Because of the high sensitivity to changes in temperature of the index of refraction of silica at low temperatures, small temperature fluctuations can in turn lead to frequency fluctuations. The vibrations of the cold platform in addition to the cantilever-like structure of the individual membranes can lead to vibrational modes of the membrane. When the sample is in contact with the sphere, the cantilever-like motion of the membrane can cause the sample to momentarily release from the sphere. This causes the sphere to heat up, and subsequently, the cavity mode will shift in frequency as it heats up and then relaxes to its original frequency while the system returns to a thermal steady state with the sample in contact again. These thermally driven frequency fluctuations are completely eliminated when the compressor is stopped. The physical process causing the thermal drift is not well understood but it seems that, to a certain extent, increasing the pressure of the sample against the sphere can reduce these fluctuations but not eliminate them altogether. Qualitatively, it seems that the fluctuations might become more of an issue when coupling to long membranes far from the base where they meet the bulk diamond. This suggests that an additional means for reducing these thermally driven frequency fluctuations could be to revisit how the SiV membranes are fabricated in order to achieve the necessary membrane thickness for minimal Q-spoiling, but without the need for a long

tapered membrane to achieve those thicknesses, creating shorter membranes that are perhaps less prone to vibration.

### **9.3. Addressing Sample Contamination**

One area in which there is much room for improvement for this experiment is the issue of contamination of the diamond membrane and microsphere. Often, the problem that ends up ending an experimental run is the accumulation of contamination that spoils the microsphere's narrow cavity line widths. The process of removing and replacing the sphere and taper is time consuming and the possibility of other components being damaged increases during the handling involved with the replacement process. If the problem of contamination could be resolved, it would allow the sphere to be usable indefinitely, which would greatly increase the fraction of lab time used for acquiring data as opposed to prepping the cryostat system for experimentation.

Evaluation and revision of the cleaning process will be necessary to eliminate the presence of microscopic particulates on the membranes. It is clear that the contamination of the diamond is not primarily due to exposure to the ambient lab environment, as visual analysis of the sphere shows no contamination (other than the contact point with the membrane), and if it were solely due to particulates in the air settling on the membrane those particulates would be visible on the sphere surface.

An SEM analysis of a contaminated sphere showed the presence of potentially two different kinds of surface contamination at the contact point. Targeted x-ray spectroscopy of some of the contamination indicated it was likely mostly comprised of organic material. The process used to clean the diamond

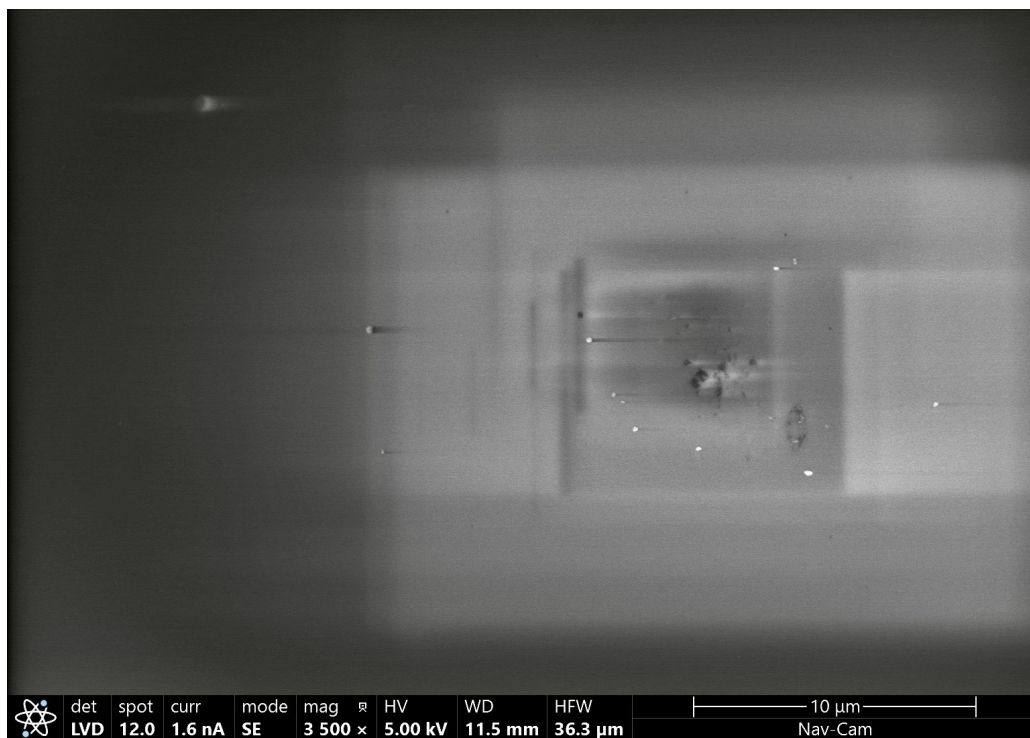


FIGURE 9.1. A micrograph of the membrane contact point of a contaminated sphere taken with a scanning electron microscope. Many spots of contamination are visible and the different shades of the contaminants suggest multiple substances are present. The blurry rectangular ghost images present in the micrograph are an artifact from hydrocarbons that deposit onto the surface while in the SEM and are subsequently burned off by the electron beam. They do not indicate actual surface features or contamination present while the sphere is in the cryostat.

utilizes boiling the sample in Piranha solution which attacks and completely breaks down organic compounds. This would suggest contamination occurs after the Piranha etch, possibly from contaminated solvents which are used to wash the sample after the etch. Identifying the contamination and its source could lead to cavities that have indefinite lifetimes of use which would be extremely beneficial for maintaining a working cQED system.

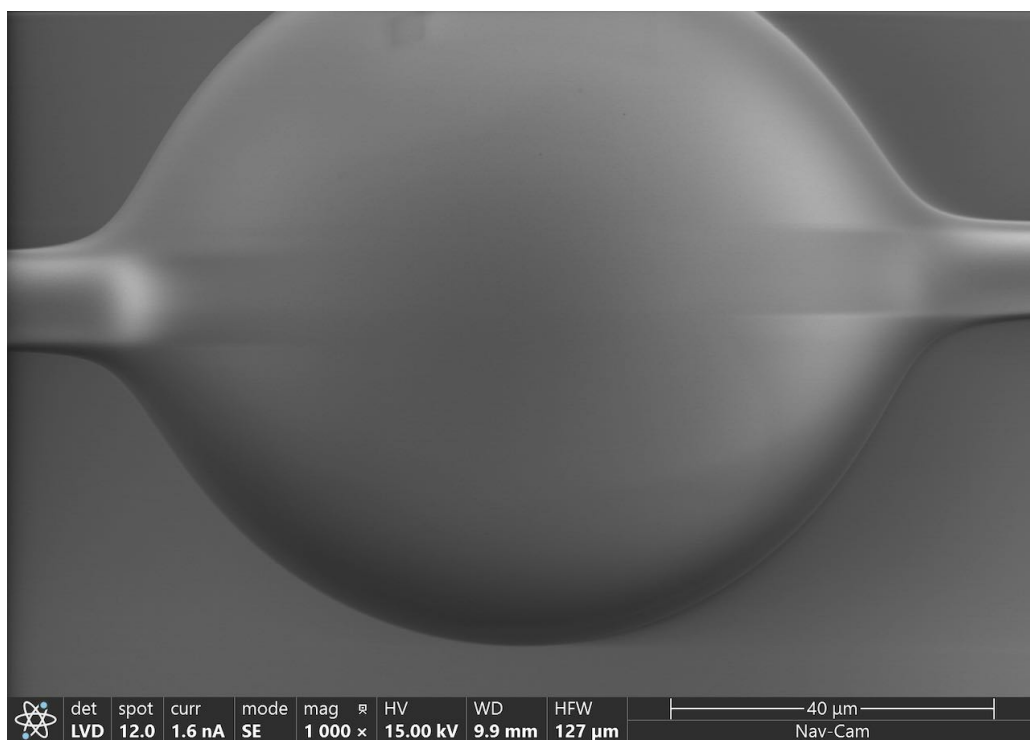


FIGURE 9.2. A micrograph of the same sphere taken at a 45° angle away from the view axis of the previous figure. The surface is clean, indicating the contamination buildup originated from contact with the membrane and not the cryostat environment itself.

#### 9.4. Managing Nitrogen Deposition

If the source of contamination from the membrane can be eliminated, the only environmental factor that would limit the usable lifetime of a cavity would be from the slow deposition of air onto the surface as it leaks into the vacuum chamber and cryo pumps onto the sphere. The Montana Instruments Fusion cryostat is designed to be convenient and simple to operate, and as such, its vacuum system is not optimized for an experiment as sensitive to contamination as this. While the charcoal absorber-type cryopump is extremely effective at maintaining a vacuum, all the seals are made using silicone o-rings and have an intrinsic leak rate much higher than what is typically used for ultra-high vacuum

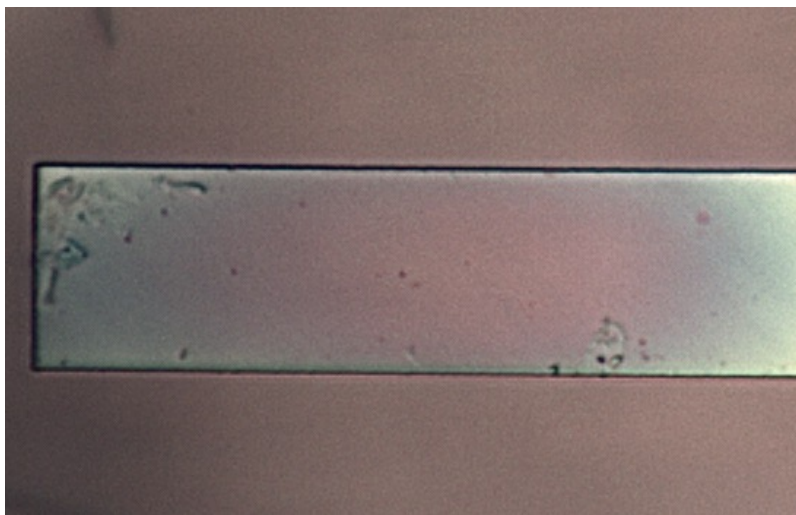


FIGURE 9.3. A micrograph of a section of a single diamond membrane taken with an optical microscope. The image has been slightly enhanced to show the numerous spots of surface contamination.

(UHV) applications. The cryo pump is capable of pulling a vacuum well into the UHV range, however, the use of silicone o-rings instead of copper ConFlats means the steady state vacuum pressure is well above UHV levels. The most effective path forward for limiting nitrogen deposition is finding methods to manage and remove the buildup rather than solving the underlying problem of o-ring leaks.

As mentioned previously, the contamination from nitrogen is reversible through heating of the sphere to a sufficient temperature to burn off the nitrogen while pumping on the vacuum chamber with a turbo pump. Without a turbo pump, the only effective way to burn off the nitrogen is by warming the entire system to room temperature and pumping on the vacuum chamber with the built in roughing pump contained within the cryostat. Because of the 5 hour warm up time and 8 hour cool down time, this process takes an entire day to complete what essentially amounts to a housekeeping task. Since the discovery of contamination from the turbo pump backed by an oil roughing pump, the use of a turbo pump is

not an option. Further, repeated cycles of cooling down to 4K and warming back up to 300 K puts strain on the epoxy bonds used to mount the taper. After several cycles, the epoxy will tend to fail and the taper will need to be replaced.

Several steps could be taken to eliminate the time wasted on nitrogen burn off cycles and to limit wear on the epoxy bonds. Replacing the turbo pump with one backed by a dry pump would allow for pumping on the vacuum chamber at temperatures around 100 K without risking back flow of oil droplets that would contaminate the entire sample space. Second, modifying the copper sample mount used to mount the diamond membrane to contain a small ohmic heater would allow for heating of the sphere without raising the temperature of the entire system. By heating the sample which the sphere is in contact with, the sphere temperature can be raised quickly, and due to the poor thermal conductivity of the sphere stems, very little heating would take place on any other components. This burn off process could be done in only a few minutes, and potentially would perform better than a normal partial warm-up-and-pump cycle, since the system would cryopump the sublimated gas without the need to pump with the turbo. The system could be maintained at 4 K for months on end and would only need to be heated up to 100 K and pumped on when the charcoal absorbers have saturated and the vacuum performance starts to degrade.

## 9.5. Potential improvements of $C$ and $g$

While experiments have not yet been performed to measure  $C$  and  $g$ , it could be possible to further improve both through modifications to the system. This would most likely need to come from a further reduction of the SiV distance from the cavity surface. Both  $\kappa$  and  $\gamma$  appear to be essentially within the optimum

values of what should be achievable, therefore an improvement would need to come from an increase in cavity field strength at the SiV point. The theoretical value of  $g/2\pi = 150$  MHz was found assuming the use of a microsphere with a  $30\text{ }\mu\text{m}$  diameter. Increasing the field intensity at the SiV site by using an even smaller sphere diameter is likely not the best option.[37] For smaller double-stemmed spheres, there would likely be more fabrication challenges, but even more fundamentally, for very small spheres, there is an increase in the cavity decay rate due to loss from the evanescent field leaking into free propagation.[40] Consequentially, this would result in a higher  $g$ , but at the expense of a higher  $\kappa$  as well. It is possible, however, that even thinner membranes could be fabricated while still maintaining optical transitions with limited broadening and bringing the SiV closer to the sphere surface where the evanescent field is the strongest.[83]

## 9.6. Modeling Membrane-Coupled Equatorial WGMs

The calculations made to estimate the potential coupling rate of an equatorial WGM with a silicon vacancy center in the diamond membrane were based on the assumption that there is no significant change made to the cavity's evanescent field as it couples to the membrane. It is not immediately clear how accurate an approximation this is, and whether there are any significant effects the membrane has on the local electromagnetic field. It could be the case that this assumption is good enough to produce reasonable estimates of the coupling strength, or there could be some as-of-yet unexpected impacts from coupling that create local field minima or maxima that are greater than anticipated.

A piece of qualitative evidence that suggests modeling the field behavior would be worthwhile is the sensitivity of Q-spoiling to sphere placement. The Q-

spoiling of equatorial modes seems to be particularly sensitive to the membrane location used to couple to the sphere. Having the sphere contact the membrane at what appears to be the thinnest segment of the membrane does not necessarily lead to the least amount of Q-spoiling. Further, it seems that there tends to be a fairly small segment along the long axis of the membrane, maybe 20 microns or so, where the Q-spoiling is minimized but increases quickly when moving the contact point away from this region. This suggests there could be factors not yet considered that could be impacting the coupling behavior. Modeling the effects of a diamond membrane on an equatorial cavity mode would help to better understand both the factors leading to Q-spoiling and the strength of the cavity's evanescent field within the diamond membrane.

### **9.7. PLE Count Rate and Signal-to-Noise Optimization**

Even absent any potential dramatic reductions in fluorescence collection using a not-in-contact tapered fiber, it would still be desirable to increase the PLE count rate and signal-to-noise ratio. As can be seen from the PLE results in the previous chapter, obtaining non-power-broadened spectra of SiV transitions requires either longer integration times or higher count rates to obtain results comparable to what is achievable with higher 737 nm power but broadened. In addition to seeing modes in the PLE spectra when the tunable long pass filter cutoff is at the edge of the laser emission curve, there is some DC background that persists even when the filter is completely normal to the incident beam. It is possible that while the taper being not in contact will result in lower PLE count rates, the coupling of the fiber to fewer modes will also result in less efficient collection of the scattered 737 nm laser light, which is responsible for increased



background counts. This should be tested as well as double checking the mode characteristics of the 737 nm laser to insure the spectral profile of the beam is as clean as possible. A notch filter is present in the beam line of the laser just after the isolator to block any potential modes other than the primary mode desired. This filter has a frequency notch that is considerably larger than the typical tuning range used for PLE scans which would mean different frequency emission modes could be present near the primary laser emission line, and consequentially, pass through the filter to reach the APD. If the laser does, in fact, prove to have emission from other modes, this could be managed by introducing a tunable short pass filter in the beam path just after the laser isolator to create a tighter cutoff closer to the proper laser emission line.

Similar DC background is visible in PL spectra when the membrane is not in contact with the sphere, and the 532 nm laser is tangentially incident to the sphere's equator which allows free space coupling of the green light into cavity modes. PL spectroscopy measurements should be repeated for this specific case with the long pass cutoff tuned to be in range of the spectrometer detection window to see if a similar step function in the elevated background can be observed. If a discrete jump is visible, this indicates there is likely some optical component along the beam path other than the membrane which is fluorescing under 532 nm illumination. It could then be the case as well that the 737 nm light is causing the same optical element to fluoresce from resonant driving, which would result in radiation that is able to pass through the optical filters along the collection path resulting in a uniform background. If this does prove to be the case, it might then be possible to replace/remove the optical element at fault, or depending on the spectral characteristics of the unwanted fluorescence, it might

be possible to attenuate with the addition of the appropriate optical filters in the collection path.

At present, the current PLE count rates and signal-to-noise ratios do not appear to pose any serious obstruction to performing the experiments necessary to observe cQED coupling effects. It would still be very advantageous for some effort to be spent on increasing the SiV fluorescence count rates for PLE and reduce the unwanted background fluorescence. Doing so would allow for less noise in the spectra data and reduce the required integration time needed to obtain clear data. Given that this experimental system integrates numerous systems with many different degrees of freedom, shorter times for data collection will make it easier to obtain multiple experimental measurements and observations in a shorter amount of time, which will help to mitigate the impact of any system drift that would confuse efforts to compare data sets.

Lastly, it could be useful to investigate whether there are other possible sources of fluorescence in the system causing the elevated DC background that is mostly insensitive to the position of the tunable long pass filter. Adding an additional long pass filter had little impact on the DC background present, which suggests the counts could be due in part to fluorescence driven by 737 nm laser light. There is some evidence to support this as a possibility. When performing PL spectroscopy with high green power (usually 10+ mW), there is a significantly elevated background count rate in addition to the expected double peak signature for SiV fluorescence using that spectrometer. There were signs that this could be due to green scatter within the spectrometer housing. Typically, the tunable long pass filter is removed from the collection path for PL spectroscopy; however, it is also possible to adjust the angle such that its cutoff is well past the SiV transitions

to keep from blocking the ZPL fluorescence. Towards the end of working on this project, several PL spectra were taken when the tunable long pass filter was left in and had accidentally not been turned sufficiently such that the cutoff of the filter was within the range of the spectrum window being measured by the spectrometer. The result was a very clear step function in the PL background which indicated that the background was in fact indicative of actual fluorescence and not the result of the imperfect rejection of green light scattering onto the CCD.

Lastly, it should be noted that PLE experiments were performed without implementing polarization control of the 737 nm excitation beam. Typically in confocal microscopy PLE studies of SiVs and NVs, a combination of a polarizer and half-waveplate are used to adjust the polarization of the resonant driving beam to optimize the fluorescence counts. This was attempted using a fiber polarization controller in the 737 nm fiber path, adjusting the polarization while observing the real time fluorescence count rate. This had little effect, however, because the limited count rate meant that the amplitude of variations in the count rate due to polarization adjustments were washed out by the signal-to-noise ratio in real-time observations. If the PLE signal-to-noise ratio can first be improved by other means such that the fluorescence count rate variation with polarization can be observed in real time, or a procedure is set up using a free space half-wave plate and utilizing longer integration times, this could allow for a further improvement in the PLE signal-to-noise ratio. A better overlap between the resonant driving polarization and SiV fluorescence would allow for comparable photon count rates to what is achievable now, but with an overall reduced optical power which would reduce detection noise.

## 9.8. Experimentation: Next steps

While the PLE spectrum of SiVs in the low density sample is good evidence for the presence of spectrally resolved single SiV transitions, ideally, this should be confirmed through further experiments. The sparseness and linewidths of the peaks in the low density PLE spectra point towards single emitters, however, it is still possible that some peaks are actually multiple SiVs overlapping in their transition frequencies. To verify the presence of single spectrally resolved SiVs,  $g^2$  two-time correlation experiments should be used to verify the presence of single photon emitters. Verification of a single photon emitter should also be done prior to performing cQED measurements at a particular PLE peak feature believed to be a single SiV. While cQED experiments can be performed with multiple SiVs, knowledge of the number of SiVs (if more than one) being coupled is useful for proper analysis of the results to determine the single-photon coupling rate and cooperativity.

Another question that needs to be addressed is the effect of taper-sphere coupling on the collection of SiV fluorescence for PLE spectroscopy. For both the PL and PLE data presented here, the tapered fiber was in contact with the sphere throughout the data collection. Having the taper in contact with the sphere allows the fiber to couple to many more modes than just those nearby with a high degree of mode overlap. As a consequence, the taper is able to collect the SiV fluorescence that is coupled into essentially any mode, thereby increasing the fluorescence count rate. When the taper is coupled to the sphere but not in contact, there are fewer modes coupled to it, but the modes are also sharper. At least from PL measurements, it appears that non-contact fiber coupling results in a reduced count rate at the detector. The effect of non-contact for PLE measurements still

needs to be investigated. A drop in PLE counts could be compensated for by opening up the tunable long pass filter to allow more of the phonon side band into the APD. This would additionally result in apparent fluorescence peaks that are in fact from 737 nm laser light scattering into the cavity modes. Care would need to be taken to distinguish SiV's from WGMs via tools like control scans without 532 nm initialization, or develop better means of filtering them without rejecting so much of the SiV phonon side band.

To observe and quantify the cQED coupling of the system, the primary method of data collection should be PLE spectroscopy of the particular SiV transition used for varying values of the cavity-SiV detuning. While cavity transmission measurements should be taken as well, PLE spectroscopy data is more likely to provide a clearly discernible signal of coupling effects and cavity transmission measurements when working in the good-cavity limit. As was discussed in the chapter on cQED, in and near the good-cavity limit (for the case of zero cavity-SiV detuning), the effects of coupling are evident through broadening of the cavity mode via damping by the SiV, and a dip in the SiV transition and for stronger coupling, the splitting of the SiV transition into two peaks. Depending on the actual strength of the SiV-cavity coupling, it could be the case that the coupling effects would be somewhat obscured in the data for WGM linewidth measurements. If the SiV induced mode broadening is comparable to the effective broadening brought about by cryostat noise, it may be difficult to reliably detect the presence of cQED induced Q-spoiling. For PLE spectroscopy, the qualitative behavior of the SiV transition induced by the cavity should be much more apparent and detectable and should be less sensitive to potential noise effects. Ideally, the coupling strength will be sufficient, and vibration noise

mitigated enough, to still observe SiV induced Q-spoiling, but for the initial search for cQED coupling, PLE spectroscopy will be more effective at initially observing it.

## 9.9. Conclusion

Over the course of this project, I have built from the ground up a platform for performing cQED experiments using silicon vacancy centers in diamond within the cQED good-cavity limit. This system utilizes a silica microsphere optical resonator which can couple to an adjacent SiV-containing diamond membrane via evanescent field while still maintaining exceptional cavity linewidths of 40 MHz. This is accomplished by utilizing SiVs contained within an ultra-thin (100 nm) diamond membrane that allows the diamond to come into contact with the sphere, thereby maximizing the single-photon coupling rate of the cavity mode to the SiVs while also minimizing Q-spoiling (as low as 3 MHz broadening observed).

Vibration and acoustic conduction into the cryostat sample chamber initially posed a major obstacle in the measurement of the cavity transmission spectrum while the cryostat compressor was running. However, a complete redesign of the cryostat experimental setup has resulted in a dramatic reduction of the system's sensitivity to such noise, allowing for experiments that require minimal cavity linewidths and/or controlled cavity detuning to be performed.

PL and PLE spectroscopy studies have shown fluorescence of single SiVs which is collected via the tapered fiber. This shows that SiVs within the diamond at the contact point do, in fact, optically couple with the WGMs of the cavity. Finer scale frequency PLE scans of the composite system also show optical transitions of single SiVs with linewidths as good as 250 MHz with narrower likely

achievable through a more patient survey of SiV linewidths. This in conjunction with the measured cavity linewidths of the composite system and the theoretically calculated single-photon coupling rate of  $g/2\pi = 150$  MHz indicates that the system should be capable of achieving cooperativities of  $C \approx 10$  while also operating within the good-cavity limit.

The ability to spectrally resolve single SiV transitions while also operating in the good-cavity limit with  $C > 1$  should enable experiments utilizing three-level  $\Lambda$  systems driven by the cavity field to realize optical control of the SiV spin state. This quantum level control will allow for operations that can reversibly transfer quantum information from the SiV spin state to the cavity mode and back. Because of the narrow cavity linewidth of this system ( $g > \kappa$ ), this state swapping can then be extended to facilitate the transfer of quantum states between multiple SiVs. Similarly, this system can also be used to generate maximally entangled states of SiV spins.

While we have yet to perform experiments that observe cQED coupling effects in this system, many of the engineering challenges that stood in the way of such experiments have been overcome. There are several ways I believe the system could be further improved and optimized, but as it stands now, there are no fundamental roadblocks preventing the observation of cQED effects.

All of the above, in conjunction with the long SiV spin lifetime, ( $> 10$  ms @ 100 mK) make the silica microsphere and diamond membrane composite system a promising candidate for applications in quantum networking that complement already existing SiV cQED architectures. This system will enable direct cavity mediated quantum control of the SiV spin state which has thus far not been accomplished. [69]

## REFERENCES CITED

- [1] Elke Neu, Christian Hepp, Michael Hauschild, Stefan Gsell, Martin Fischer, Hadwig Sternschulte, Doris Steinmüller-Nethl, Matthias Schreck, and Christoph Becher. Low-temperature investigations of single silicon vacancy colour centres in diamond. *New Journal of Physics*, 15(4):043005, apr 2013. doi: 10.1088/1367-2630/15/4/043005. URL <https://doi.org/10.1088/1367-2630/15/4/043005>.
- [2] L. J. Rogers, K. D. Jahnke, T. Teraji, L. Marseglia, C. Müller, B. Naydenov, H. Schauffert, C. Kranz, J. Isoya, L. P. McGuinness, and F. Jelezko. Multiple intrinsically identical single-photon emitters in the solid state. *Nature Communications*, 5(1):4739, Aug 2014. ISSN 2041-1723. doi: 10.1038/ncomms5739. URL <https://doi.org/10.1038/ncomms5739>.
- [3] A. Sipahigil, K. D. Jahnke, L. J. Rogers, T. Teraji, J. Isoya, A. S. Zibrov, F. Jelezko, and M. D. Lukin. Indistinguishable photons from separated silicon-vacancy centers in diamond. *Phys. Rev. Lett.*, 113:113602, Sep 2014. doi: 10.1103/PhysRevLett.113.113602. URL <https://link.aps.org/doi/10.1103/PhysRevLett.113.113602>.
- [4] R. J. Schoelkopf and S. M. Girvin. Wiring up quantum systems. *Nature*, 451(7179):664–669, Feb 2008. ISSN 1476-4687. doi: 10.1038/451664a. URL <https://doi.org/10.1038/451664a>.
- [5] J. Q. You and Franco Nori. Atomic physics and quantum optics using superconducting circuits. *Nature*, 474(7353):589–597, Jun 2011. ISSN 1476-4687. doi: 10.1038/nature10122. URL <https://doi.org/10.1038/nature10122>.
- [6] Peter Lodahl, Sahand Mahmoodian, and Søren Stobbe. Interfacing single photons and single quantum dots with photonic nanostructures. *Rev. Mod. Phys.*, 87:347–400, May 2015. doi: 10.1103/RevModPhys.87.347. URL <https://link.aps.org/doi/10.1103/RevModPhys.87.347>.
- [7] Shuo Sun, Hyochul Kim, Glenn S. Solomon, and Edo Waks. A quantum phase switch between a single solid-state spin and a photon. *Nature Nanotechnology*, 11(6):539–544, Jun 2016. ISSN 1748-3395. doi: 10.1038/nnano.2015.334. URL <https://doi.org/10.1038/nnano.2015.334>.
- [8] Luo Z Solomon GS Waks E. Sun S, Kim H. A single-photon switch and transistor enabled by a solid-state quantum memory. *Science*, 361:57–60, July 2018. doi: 10.1126/science.aat3581.



- [9] H. J. Kimble. The quantum internet. *Nature*, 453(7198):1023–1030, Jun 2008. ISSN 1476-4687. doi: 10.1038/nature07127. URL <https://doi.org/10.1038/nature07127>.
- [10] Marcus W. Doherty, Neil B. Manson, Paul Delaney, Fedor Jelezko, Jörg Wrachtrup, and Lloyd C.L. Hollenberg. The nitrogen-vacancy colour centre in diamond. *Physics Reports*, 528(1):1–45, 2013. ISSN 0370-1573. doi: <https://doi.org/10.1016/j.physrep.2013.02.001>. URL <https://www.sciencedirect.com/science/article/pii/S0370157313000562>. The nitrogen-vacancy colour centre in diamond.
- [11] Lilian Childress, Ronald Walsworth, and Mikhail Lukin. Atom-like crystal defects: From quantum computers to biological sensors. *Physics Today*, 67(10):38–43, 2014. doi: 10.1063/PT.3.2549. URL <https://doi.org/10.1063/PT.3.2549>.
- [12] W. B. Gao, A. Imamoglu, H. Bernien, and R. Hanson. Coherent manipulation, measurement and entanglement of individual solid-state spins using optical fields. *Nature Photonics*, 9(6):363–373, Jun 2015. ISSN 1749-4893. doi: 10.1038/nphoton.2015.58. URL <https://doi.org/10.1038/nphoton.2015.58>.
- [13] David D. Awschalom, Ronald Hanson, Jörg Wrachtrup, and Brian B. Zhou. Quantum technologies with optically interfaced solid-state spins. *Nature Photonics*, 12(9):516–527, Sep 2018. ISSN 1749-4893. doi: 10.1038/s41566-018-0232-2. URL <https://doi.org/10.1038/s41566-018-0232-2>.
- [14] Klemens Hammerer, Anders S. Sørensen, and Eugene S. Polzik. Quantum interface between light and atomic ensembles. *Rev. Mod. Phys.*, 82:1041–1093, Apr 2010. doi: 10.1103/RevModPhys.82.1041. URL <https://link.aps.org/doi/10.1103/RevModPhys.82.1041>.
- [15] L.-M. Duan and C. Monroe. Colloquium: Quantum networks with trapped ions. *Rev. Mod. Phys.*, 82:1209–1224, Apr 2010. doi: 10.1103/RevModPhys.82.1209. URL <https://link.aps.org/doi/10.1103/RevModPhys.82.1209>.
- [16] T. E. Northup and R. Blatt. Quantum information transfer using photons. *Nature Photonics*, 8(5):356–363, May 2014. ISSN 1749-4893. doi: 10.1038/nphoton.2014.53. URL <https://doi.org/10.1038/nphoton.2014.53>.

- [17] Andreas Reiserer and Gerhard Rempe. Cavity-based quantum networks with single atoms and optical photons. *Rev. Mod. Phys.*, 87:1379–1418, Dec 2015. doi: 10.1103/RevModPhys.87.1379. URL <https://link.aps.org/doi/10.1103/RevModPhys.87.1379>.
- [18] D. D. Sukachev, A. Sipahigil, C. T. Nguyen, M. K. Bhaskar, R. E. Evans, F. Jelezko, and M. D. Lukin. Silicon-vacancy spin qubit in diamond: A quantum memory exceeding 10 ms with single-shot state readout. *Phys. Rev. Lett.*, 119:223602, Nov 2017. doi: 10.1103/PhysRevLett.119.223602. URL <https://link.aps.org/doi/10.1103/PhysRevLett.119.223602>.
- [19] Kay D Jahnke, Alp Sipahigil, Jan M Binder, Marcus W Doherty, Mathias Metsch, Lachlan J Rogers, Neil B Manson, Mikhail D Lukin, and Fedor Jelezko. Electron–phonon processes of the silicon-vacancy centre in diamond. *New Journal of Physics*, 17(4):043011, apr 2015. doi: 10.1088/1367-2630/17/4/043011. URL <https://doi.org/10.1088/1367-2630/17/4/043011>.
- [20] Brendon C. Rose, Ding Huang, Zi-Huai Zhang, Paul Stevenson, Alexei M. Tyryshkin, Sorawis Sangtawesin, Srikanth Srinivasan, Lorne Loudin, Matthew L. Markham, Andrew M. Edmonds, Daniel J. Twitchen, Stephen A. Lyon, and Nathalie P. de Leon. Observation of an environmentally insensitive solid-state spin defect in diamond. *Science*, 361(6397):60–63, 2018. doi: 10.1126/science.aao0290. URL <https://www.science.org/doi/abs/10.1126/science.aao0290>.
- [21] A. Sipahigil, R. E. Evans, D. D. Sukachev, M. J. Burek, J. Borregaard, M. K. Bhaskar, C. T. Nguyen, J. L. Pacheco, H. A. Atikian, C. Meuwly, R. M. Camacho, F. Jelezko, E. Bielejec, H. Park, M. Lončar, and M. D. Lukin. An integrated diamond nanophotonics platform for quantum-optical networks. *Science*, 354(6314):847–850, 2016. doi: 10.1126/science.aah6875. URL <https://www.science.org/doi/abs/10.1126/science.aah6875>.
- [22] Lachlan J. Rogers, Kay D. Jahnke, Mathias H. Metsch, Alp Sipahigil, Jan M. Binder, Tokuyuki Teraji, Hitoshi Sumiya, Junichi Isoya, Mikhail D. Lukin, Philip Hemmer, and Fedor Jelezko. All-optical initialization, readout, and coherent preparation of single silicon-vacancy spins in diamond. *Phys. Rev. Lett.*, 113:263602, Dec 2014. doi: 10.1103/PhysRevLett.113.263602. URL <https://link.aps.org/doi/10.1103/PhysRevLett.113.263602>.

- [23] Benjamin Pingault, Jonas N. Becker, Carsten H. H. Schulte, Carsten Arend, Christian Hepp, Tillmann Godde, Alexander I. Tartakovskii, Matthew Markham, Christoph Becher, and Mete Atatüre. All-optical formation of coherent dark states of silicon-vacancy spins in diamond. *Phys. Rev. Lett.*, 113:263601, Dec 2014. doi: 10.1103/PhysRevLett.113.263601. URL <https://link.aps.org/doi/10.1103/PhysRevLett.113.263601>.
- [24] Jonas N. Becker, Benjamin Pingault, David Groß, Mustafa Gündoğan, Nadezhda Kukharchyk, Matthew Markham, Andrew Edmonds, Mete Atatüre, Pavel Bushev, and Christoph Becher. All-optical control of the silicon-vacancy spin in diamond at millikelvin temperatures. *Phys. Rev. Lett.*, 120:053603, Jan 2018. doi: 10.1103/PhysRevLett.120.053603. URL <https://link.aps.org/doi/10.1103/PhysRevLett.120.053603>.
- [25] Jingyuan Linda Zhang, Konstantinos G. Lagoudakis, Yan-Kai Tzeng, Constantin Dory, Marina Radulaski, Yousif Kelaita, Kevin A. Fischer, Shuo Sun, Zhi-Xun Shen, Nicholas A. Melosh, Steven Chu, and Jelena Vučković. Complete coherent control of silicon vacancies in diamond nanopillars containing single defect centers. *Optica*, 4(11):1317–1321, Nov 2017. doi: 10.1364/OPTICA.4.001317. URL <http://opg.optica.org/optica/abstract.cfm?URI=optica-4-11-1317>.
- [26] Uwe Jantzen, Andrea B Kurz, Daniel S Rudnicki, Clemens Schäfermeier, Kay D Jahnke, Ulrik L Andersen, Valery A Davydov, Viatcheslav N Agafonov, Alexander Kubanek, Lachlan J Rogers, and Fedor Jelezko. Nanodiamonds carrying silicon-vacancy quantum emitters with almost lifetime-limited linewidths. *New Journal of Physics*, 18(7):073036, jul 2016. doi: 10.1088/1367-2630/18/7/073036. URL <https://doi.org/10.1088/1367-2630/18/7/073036>.
- [27] Ruffin E. Evans, Alp Sipahigil, Denis D. Sukachev, Alexander S. Zibrov, and Mikhail D. Lukin. Narrow-linewidth homogeneous optical emitters in diamond nanostructures via silicon ion implantation. *Phys. Rev. Applied*, 5:044010, Apr 2016. doi: 10.1103/PhysRevApplied.5.044010. URL <https://link.aps.org/doi/10.1103/PhysRevApplied.5.044010>.
- [28] Ignas Lekavicius and Hailin Wang. Optical coherence of implanted silicon vacancy centers in thin diamond membranes. *Opt. Express*, 27(22):31299–31306, Oct 2019. doi: 10.1364/OE.27.031299. URL <http://opg.optica.org/oe/abstract.cfm?URI=oe-27-22-31299>.
- [29] J. M. Raimond, M. Brune, and S. Haroche. Manipulating quantum entanglement with atoms and photons in a cavity. *Rev. Mod. Phys.*, 73:565–582, Aug 2001. doi: 10.1103/RevModPhys.73.565. URL <https://link.aps.org/doi/10.1103/RevModPhys.73.565>.

- [30] Jingyuan Linda Zhang, Shuo Sun, Michael J. Burek, Constantin Dory, Yan-Kai Tzeng, Kevin A. Fischer, Yousif Kelaita, Konstantinos G. Lagoudakis, Marina Radulaski, Zhi-Xun Shen, Nicholas A. Melosh, Steven Chu, Marko Lončar, and Jelena Vučković. Strongly cavity-enhanced spontaneous emission from silicon-vacancy centers in diamond. *Nano Letters*, 18(2):1360–1365, Feb 2018. ISSN 1530-6984. doi: 10.1021/acs.nanolett.7b05075. URL <https://doi.org/10.1021/acs.nanolett.7b05075>.
- [31] Jonathan C. Lee, Igor Aharonovich, Andrew P. Magyar, Fabian Rol, and Evelyn L. Hu. Coupling of silicon-vacancy centers to a single crystal diamond cavity. *Opt. Express*, 20(8):8891–8897, Apr 2012. doi: 10.1364/OE.20.008891. URL <http://opg.optica.org/oe/abstract.cfm?URI=oe-20-8-8891>.
- [32] Srujan Meesala, Young-Ik Sohn, Haig A. Atikian, Samuel Kim, Michael J. Burek, Jennifer T. Choy, and Marko Lončar. Enhanced strain coupling of nitrogen-vacancy spins to nanoscale diamond cantilevers. *Phys. Rev. Applied*, 5:034010, Mar 2016. doi: 10.1103/PhysRevApplied.5.034010. URL <https://link.aps.org/doi/10.1103/PhysRevApplied.5.034010>.
- [33] Ignas Lekavicius, Thein Oo, and Hailin Wang. Diamond phononic crystal spin-mechanical resonators with spectrally-stable nitrogen vacancy centers. In *Conference on Lasers and Electro-Optics*, page JW3A.3. Optica Publishing Group, 2019. URL [http://opg.optica.org/abstract.cfm?URI=CLEO\\_SI-2019-JW3A.3](http://opg.optica.org/abstract.cfm?URI=CLEO_SI-2019-JW3A.3).
- [34] R. E. Evans, M. K. Bhaskar, D. D. Sukachev, C. T. Nguyen, A. Sipahigil, M. J. Burek, B. Machielse, G. H. Zhang, A. S. Zibrov, E. Bielejec, H. Park, M. Lončar, and M. D. Lukin. Photon-mediated interactions between quantum emitters in a diamond nanocavity. *Science*, 362(6415):662–665, 2018. doi: 10.1126/science.aau4691. URL <https://www.science.org/doi/abs/10.1126/science.aau4691>.
- [35] Shuo Sun, Jingyuan Linda Zhang, Kevin A. Fischer, Michael J. Burek, Constantin Dory, Konstantinos G. Lagoudakis, Yan-Kai Tzeng, Marina Radulaski, Yousif Kelaita, Amir Safavi-Naeini, Zhi-Xun Shen, Nicholas A. Melosh, Steven Chu, Marko Lončar, and Jelena Vučković. Cavity-enhanced raman emission from a single color center in a solid. *Phys. Rev. Lett.*, 121:083601, Aug 2018. doi: 10.1103/PhysRevLett.121.083601. URL <https://link.aps.org/doi/10.1103/PhysRevLett.121.083601>.

- [36] C. T. Nguyen, D. D. Sukachev, M. K. Bhaskar, B. Machielse, D. S. Levonian, E. N. Knall, P. Stroganov, C. Chia, M. J. Burek, R. Riedinger, H. Park, M. Lončar, and M. D. Lukin. An integrated nanophotonic quantum register based on silicon-vacancy spins in diamond. *Phys. Rev. B*, 100:165428, Oct 2019. doi: 10.1103/PhysRevB.100.165428. URL <https://link.aps.org/doi/10.1103/PhysRevB.100.165428>.
- [37] J. R. Buck and H. J. Kimble. Optimal sizes of dielectric microspheres for cavity qed with strong coupling. *Phys. Rev. A*, 67:033806, Mar 2003. doi: 10.1103/PhysRevA.67.033806. URL <https://link.aps.org/doi/10.1103/PhysRevA.67.033806>.
- [38] Mats Larsson, Khodadad Nima Dinyari, and Hailin Wang. Composite optical microcavity of diamond nanopillar and silica microsphere. *Nano Letters*, 9(4): 1447–1450, Apr 2009. ISSN 1530-6984. doi: 10.1021/nl8032944. URL <https://doi.org/10.1021/nl8032944>.
- [39] Russell J. Barbour, Khodadad N. Dinyari, and Hailin Wang. A composite microcavity of diamond nanopillar and deformed silica microsphere with enhanced evanescent decay length. *Opt. Express*, 18(18):18968–18974, Aug 2010. doi: 10.1364/OE.18.018968. URL <http://opg.optica.org/oe/abstract.cfm?URI=oe-18-18-18968>.
- [40] T.J. Kippenberg. *Nonlinear Optics in Ultra-high-Q Whispering-Gallery Optical Microcavities*. PhD thesis, 2004.
- [41] Young-Shin Park and Hailin Wang. Resolved-sideband and cryogenic cooling of an optomechanical resonator. *Nature Physics*, 5(7):489–493, Jul 2009. ISSN 1745-2481. doi: 10.1038/nphys1303. URL <https://doi.org/10.1038/nphys1303>.
- [42] Young-Shin Park, Andrew K. Cook, and Hailin Wang. Cavity qed with diamond nanocrystals and silica microspheres. *Nano Letters*, 6(9):2075–2079, 2006. doi: 10.1021/nl061342r. URL <https://doi.org/10.1021/nl061342r>. PMID: 16968028.
- [43] Christian Hepp, Tina Müller, Victor Waselowski, Jonas N. Becker, Benjamin Pingault, Hadwig Sternschulte, Doris Steinmüller-Nethl, Adam Gali, Jeronimo R. Maze, Mete Atatüre, and Christoph Becher. Electronic structure of the silicon vacancy color center in diamond. *Phys. Rev. Lett.*, 112:036405, Jan 2014. doi: 10.1103/PhysRevLett.112.036405. URL <https://link.aps.org/doi/10.1103/PhysRevLett.112.036405>.
- [44] Paul Berman and Vladimir S. Malinovsky. *Principles of Laser Spectroscopy and Quantum Optics*. Princeton University Press, 2011. ISBN 9780691140568.

- [45] Stéphane Balac. Wgmode : A matlab toolbox for whispering gallery modes volume computation in spherical optical micro-resonators. *Computer Physics Communications*, 243:121–134, 2019. ISSN 0010-4655. doi: <https://doi.org/10.1016/j.cpc.2019.05.002>. URL <https://www.sciencedirect.com/science/article/pii/S0010465519301511>.
- [46] V.B. Braginsky, M.L. Gorodetsky, and V.S. Ilchenko. Quality-factor and nonlinear properties of optical whispering-gallery modes. *Physics Letters A*, 137(7):393–397, 1989. ISSN 0375-9601. doi: [https://doi.org/10.1016/0375-9601\(89\)90912-2](https://doi.org/10.1016/0375-9601(89)90912-2). URL <https://www.sciencedirect.com/science/article/pii/0375960189909122>.
- [47] Michael L. Gorodetsky, Andrew D. Pryamikov, and Vladimir S. Ilchenko. Rayleigh scattering in high- $q$  microspheres. *J. Opt. Soc. Am. B*, 17(6):1051–1057, Jun 2000. doi: 10.1364/JOSAB.17.001051. URL <http://opg.optica.org/josab/abstract.cfm?URI=josab-17-6-1051>.
- [48] Jonas Nils Becker and Christoph Becher. Coherence properties and quantum control of silicon vacancy color centers in diamond (phys. status solidi a 112017). *physica status solidi (a)*, 214(11):1770170, 2017. doi: <https://doi.org/10.1002/pssa.201770170>. URL <https://onlinelibrary.wiley.com/doi/abs/10.1002/pssa.201770170>.
- [49] Chunhua Dong, Victor Fiore, Mark C. Kuzyk, and Hailin Wang. Optomechanical dark mode. *Science*, 338(6114):1609–1613, 2012. doi: 10.1126/science.1228370. URL <https://www.science.org/doi/abs/10.1126/science.1228370>.
- [50] J.D. Jackson, editor. *Classical Electrodynamics*. John Wiley Sons, 1999.
- [51] J.A. Stratton, editor. *Electromagnetic Theory*. 1941.
- [52] M. Pöllinger, D. O’Shea, F. Warken, and A. Rauschenbeutel. Ultrahigh- $q$  tunable whispering-gallery-mode microresonator. *Phys. Rev. Lett.*, 103:053901, Jul 2009. doi: 10.1103/PhysRevLett.103.053901. URL <https://link.aps.org/doi/10.1103/PhysRevLett.103.053901>.
- [53] Y. Louyer, D. Meschede, and A. Rauschenbeutel. Tunable whispering-gallery-mode resonators for cavity quantum electrodynamics. *Phys. Rev. A*, 72:031801, Sep 2005. doi: 10.1103/PhysRevA.72.031801. URL <https://link.aps.org/doi/10.1103/PhysRevA.72.031801>.

- [54] M.L. Gorodetsky and V.S. Ilchenko. High-q optical whispering-gallery microresonators: precession approach for spherical mode analysis and emission patterns with prism couplers. *Optics Communications*, 113(1): 133–143, 1994. ISSN 0030-4018. doi: [https://doi.org/10.1016/0030-4018\(94\)90603-3](https://doi.org/10.1016/0030-4018(94)90603-3). URL <https://www.sciencedirect.com/science/article/pii/0030401894906033>.
- [55] Young-Shin Park and Hailin Wang. Radiation pressure driven mechanical oscillation in deformed silica microspheres via free-space evanescent excitation. *Opt. Express*, 15(25):16471–16477, Dec 2007. doi: 10.1364/OE.15.016471. URL <http://opg.optica.org/oe/abstract.cfm?URI=oe-15-25-16471>.
- [56] A. Serpengüzel, S. Arnold, and G. Griffel. Excitation of resonances of microspheres on an optical fiber. *Opt. Lett.*, 20(7):654–656, Apr 1995. doi: 10.1364/OL.20.000654. URL <http://opg.optica.org/ol/abstract.cfm?URI=ol-20-7-654>.
- [57] A. Yariv. Universal relations for coupling of optical power between microresonators and dielectric waveguides (vol 36, pg 321, 2000). *Electronics Letters*, 36:999–999, 02 2000.
- [58] Wolf von Klitzing, Romain Long, Vladimir S. Ilchenko, Jean Hare, and Valérie Lefèvre-Seguin. Frequency tuning of the whispering-gallery modes of silica microspheres for cavity quantum electrodynamics and spectroscopy. *Opt. Lett.*, 26(3):166–168, Feb 2001. doi: 10.1364/OL.26.000166. URL <http://ol.osa.org/abstract.cfm?URI=ol-26-3-166>.
- [59] Khodadad N. Dinyari, Russell J. Barbour, D. Andrew Golter, and Hailin Wang. Mechanical tuning of whispering gallery modes over a 0.5 thz tuning range with mhz resolution in a silica microsphere at cryogenic temperatures. *Opt. Express*, 19(19):17966–17972, Sep 2011. doi: 10.1364/OE.19.017966. URL <http://opg.optica.org/oe/abstract.cfm?URI=oe-19-19-17966>.
- [60] Srujan Meesala, Young-Ik Sohn, Benjamin Pingault, Linbo Shao, Haig A. Atikian, Jeffrey Holzgrafe, Mustafa Gündoğan, Camille Stavrakas, Alp Sipahigil, Cleaven Chia, Ruffin Evans, Michael J. Burek, Mian Zhang, Lue Wu, Jose L. Pacheco, John Abraham, Edward Bielejec, Mikhail D. Lukin, Mete Atatüre, and Marko Lončar. Strain engineering of the silicon-vacancy center in diamond. *Phys. Rev. B*, 97:205444, May 2018. doi: 10.1103/PhysRevB.97.205444. URL <https://link.aps.org/doi/10.1103/PhysRevB.97.205444>.

- [61] Young-Ik Sohn, Srujan Meesala, Benjamin Pingault, Haig A. Atikian, Jeffrey Holzgrafe, Mustafa Gündoğan, Camille Stavrakas, Megan J. Stanley, Alp Sipahigil, Joonhee Choi, Mian Zhang, Jose L. Pacheco, John Abraham, Edward Bielejec, Mikhail D. Lukin, Mete Atatüre, and Marko Lončar. Controlling the coherence of a diamond spin qubit through its strain environment. *Nature Communications*, 9(1):2012, May 2018. ISSN 2041-1723. doi: 10.1038/s41467-018-04340-3. URL <https://doi.org/10.1038/s41467-018-04340-3>.
- [62] Benjamin Pingault, David-Dominik Jarausch, Christian Hepp, Lina Klintberg, Jonas N. Becker, Matthew Markham, Christoph Becher, and Mete Atatüre. Coherent control of the silicon-vacancy spin in diamond. *Nature Communications*, 8(1):15579, May 2017. ISSN 2041-1723. doi: 10.1038/ncomms15579. URL <https://doi.org/10.1038/ncomms15579>.
- [63] Ignas Lekavicius and Hailin Wang. Optical coherence of implanted silicon vacancy centers in thin diamond membranes. *Opt. Express*, 27(22): 31299–31306, Oct 2019. doi: 10.1364/OE.27.031299. URL <http://opg.optica.org/oe/abstract.cfm?URI=oe-27-22-31299>.
- [64] Martin Mücke, Eden Figueroa, Joerg Bochmann, Carolin Hahn, Karim Murr, Stephan Ritter, Celso J. Villas-Boas, and Gerhard Rempe. Electromagnetically induced transparency with single atoms in a cavity. *Nature*, 465(7299):755–758, Jun 2010. ISSN 1476-4687. doi: 10.1038/nature09093. URL <https://doi.org/10.1038/nature09093>.
- [65] Haibin Wu, J. Gea-Banacloche, and Min Xiao. Observation of intracavity electromagnetically induced transparency and polariton resonances in a doppler-broadened medium. *Phys. Rev. Lett.*, 100:173602, May 2008. doi: 10.1103/PhysRevLett.100.173602. URL <https://link.aps.org/doi/10.1103/PhysRevLett.100.173602>.
- [66] D. Andrew Golter and Hailin Wang. Optically driven rabi oscillations and adiabatic passage of single electron spins in diamond. *Phys. Rev. Lett.*, 112: 116403, Mar 2014. doi: 10.1103/PhysRevLett.112.116403. URL <https://link.aps.org/doi/10.1103/PhysRevLett.112.116403>.
- [67] A. Imamoglu, D. D. Awschalom, G. Burkard, D. P. DiVincenzo, D. Loss, M. Sherwin, and A. Small. Quantum information processing using quantum dot spins and cavity qed. *Phys. Rev. Lett.*, 83:4204–4207, Nov 1999. doi: 10.1103/PhysRevLett.83.4204. URL <https://link.aps.org/doi/10.1103/PhysRevLett.83.4204>.



- [68] Shi-Biao Zheng and Guang-Can Guo. Efficient scheme for two-atom entanglement and quantum information processing in cavity qed. *Phys. Rev. Lett.*, 85:2392–2395, Sep 2000. doi: 10.1103/PhysRevLett.85.2392. URL <https://link.aps.org/doi/10.1103/PhysRevLett.85.2392>.
- [69] J. I. Cirac, P. Zoller, H. J. Kimble, and H. Mabuchi. Quantum state transfer and entanglement distribution among distant nodes in a quantum network. *Phys. Rev. Lett.*, 78:3221–3224, Apr 1997. doi: 10.1103/PhysRevLett.78.3221. URL <https://link.aps.org/doi/10.1103/PhysRevLett.78.3221>.
- [70] Wang Yao, Ren-Bao Liu, and L. J. Sham. Theory of control of the spin-photon interface for quantum networks. *Phys. Rev. Lett.*, 95:030504, Jul 2005. doi: 10.1103/PhysRevLett.95.030504. URL <https://link.aps.org/doi/10.1103/PhysRevLett.95.030504>.
- [71] A. D. Boozer, A. Boca, R. Miller, T. E. Northup, and H. J. Kimble. Reversible state transfer between light and a single trapped atom. *Phys. Rev. Lett.*, 98:193601, May 2007. doi: 10.1103/PhysRevLett.98.193601. URL <https://link.aps.org/doi/10.1103/PhysRevLett.98.193601>.
- [72] E. Hagley, X. Maître, G. Nogues, C. Wunderlich, M. Brune, J. M. Raimond, and S. Haroche. Generation of einstein-podolsky-rosen pairs of atoms. *Phys. Rev. Lett.*, 79:1–5, Jul 1997. doi: 10.1103/PhysRevLett.79.1. URL <https://link.aps.org/doi/10.1103/PhysRevLett.79.1>.
- [73] S. Osnaghi, P. Bertet, A. Auffeves, P. Maioli, M. Brune, J. M. Raimond, and S. Haroche. Coherent control of an atomic collision in a cavity. *Phys. Rev. Lett.*, 87:037902, Jun 2001. doi: 10.1103/PhysRevLett.87.037902. URL <https://link.aps.org/doi/10.1103/PhysRevLett.87.037902>.
- [74] J Majer, JM Chow, JM Gambetta, Jens Koch, BR Johnson, JA Schreier, L Frunzio, DI Schuster, AA Houck, A Wallraff, A Blais, MH Devoret, SM Girvin, and RJ Schoelkopf. Coupling superconducting qubits via a cavity bus. *Nature*, 449(7161):443–447, September 2007. ISSN 0028-0836. doi: 10.1038/nature06184. URL <https://doi.org/10.1038/nature06184>.
- [75] J. Borregaard, P. Kómár, E. M. Kessler, A. S. Sørensen, and M. D. Lukin. Heralded quantum gates with integrated error detection in optical cavities. *Phys. Rev. Lett.*, 114:110502, Mar 2015. doi: 10.1103/PhysRevLett.114.110502. URL <https://link.aps.org/doi/10.1103/PhysRevLett.114.110502>.

- [76] Sophia E. Economou, Netanel Lindner, and Terry Rudolph. Optically generated 2-dimensional photonic cluster state from coupled quantum dots. *Phys. Rev. Lett.*, 105:093601, Aug 2010. doi: 10.1103/PhysRevLett.105.093601. URL <https://link.aps.org/doi/10.1103/PhysRevLett.105.093601>.
- [77] H.-J. Briegel, W. Dür, J. I. Cirac, and P. Zoller. Quantum repeaters: The role of imperfect local operations in quantum communication. *Phys. Rev. Lett.*, 81:5932–5935, Dec 1998. doi: 10.1103/PhysRevLett.81.5932. URL <https://link.aps.org/doi/10.1103/PhysRevLett.81.5932>.
- [78] J. Borregaard, P. Kómár, E. M. Kessler, M. D. Lukin, and A. S. Sørensen. Long-distance entanglement distribution using individual atoms in optical cavities. *Phys. Rev. A*, 92:012307, Jul 2015. doi: 10.1103/PhysRevA.92.012307. URL <https://link.aps.org/doi/10.1103/PhysRevA.92.012307>.
- [79] Sreraman Muralidharan, Jungsang Kim, Norbert Lütkenhaus, Mikhail D. Lukin, and Liang Jiang. Ultrafast and fault-tolerant quantum communication across long distances. *Phys. Rev. Lett.*, 112:250501, Jun 2014. doi: 10.1103/PhysRevLett.112.250501. URL <https://link.aps.org/doi/10.1103/PhysRevLett.112.250501>.
- [80] Mercedes Gimeno-Segovia, Terry Rudolph, and Sophia E. Economou. Deterministic generation of large-scale entangled photonic cluster state from interacting solid state emitters. *Phys. Rev. Lett.*, 123:070501, Aug 2019. doi: 10.1103/PhysRevLett.123.070501. URL <https://link.aps.org/doi/10.1103/PhysRevLett.123.070501>.
- [81] Peter Schnauber, Anshuman Singh, Johannes Schall, Suk In Park, Jin Dong Song, Sven Rodt, Kartik Srinivasan, Stephan Reitzenstein, and Marcelo Davanco. Indistinguishable photons from deterministically integrated single quantum dots in heterogeneous gaas/si3n4 quantum photonic circuits. In *Frontiers in Optics + Laser Science APS/DLS*, page FM3D.5. Optica Publishing Group, 2019. doi: 10.1364/FIO.2019.FM3D.5. URL <http://opg.optica.org/abstract.cfm?URI=FiO-2019-FM3D.5>.
- [82] Tzu-Han Chang, Brian M. Fields, May E. Kim, and Chen-Lung Hung. Microring resonators on a suspended membrane circuit for atom&#x2013;light interactions. *Optica*, 6(9):1203–1210, Sep 2019. doi: 10.1364/OPTICA.6.001203. URL <http://opg.optica.org/optica/abstract.cfm?URI=optica-6-9-1203>.

- [83] Johannes Lang, Stefan Häußler, Jens Fuhrmann, Richard Waltrich, Sunny Laddha, Jochen Scharpf, Alexander Kubanek, Boris Naydenov, and Fedor Jelezko. Long optical coherence times of shallow-implanted, negatively charged silicon vacancy centers in diamond. *Applied Physics Letters*, 116(6): 064001, 2020. doi: 10.1063/1.5143014. URL <https://doi.org/10.1063/1.5143014>.